Contribution to Localization and Motion Control of Inertial Actuated Nano-Robotic Systems Inside Electron Microscopy

Shuai Liang

Thesis

presented at

Sorbonne University

by

Shuai LIANG

for the thesis evaluation of the

Doctorate of Sorbonne University

In the field of robotics

Contribution to Localization and Motion Control of Inertial Actuated Nano-Robotic Systems Inside Electron Microscopy

---

Committee

M.	Sergej Fatikow	Professor, Dr.-Ing. habil at University of Oldenburg	Rapporteur
M.	Philippe Lutz	Professor at Burgundy Franche-Comté University	Rapporteur
M.	Stéphane Doncieux	Professor at Sorbonne University	Examiner
M.	Frédéric Lamarque	Professor at University of Technology of Compiègne	Examiner
Mrs.	Catherine Achard	Associate Professor, HDR at Sorbonne University	Guest
M.	Stéphane Régnier	Professor at Sorbonne University	Thesis director
M.	Mokrane Boudaoud	Associate Professor at Sorbonne University	Co-supervisor

Thesis defense: October 4, 2019

Abstract

Progress in micro/nano actuation and sensing systems over recent years has greatly extended the capability to explore, observe, feel, interrogate, and manipulate a variety of samples at small scales, from the millimeter down to the size of individual atoms. These technological and scientific advances are fundamental to a wide range of applications including, micro-nano-manipulation and assembly, material characterization at micro/nano-scales, localization and physical analysis of single molecules. The trend is the combination between nano-robotic systems and Scanning Electron Microscopy (SEM) and to achieve robotic tasks in such an environment in automated ways. This choice is mainly motivated by performance that classical optical microscopy cannot offer, i.e. the nano-metric imaging resolution and the depth of field which is necessary to simultaneously observe tools and samples. The works related in the literature have tackled very interesting critical issues of robotic at the small, but they have been made successfully thanks to the experience of the operator in the filed. Current control interfaces are therefore a real impediment toward a widespread use of robotic technology inside electron microscopy by a broad scientific community. This thesis targets the development of a generic, intelligent and user friendly interface that can manage elementary robotic tasks needed inside a SEM by simply defining graphical instructions on the SEM screen. To deal with the very high magnification capability of SEM and to be able to reach any region of interest on sample observed by such microscopes, the robot end effectors must have the capability to navigate with a displacement range to resolution ratio of several million times. As such, all the motion control must deal with multi-scale trajectories, i.e. trajectories in the nano-meter range up to the milliliter range. The main experimental platform considered in this thesis is the ISIR-robotex nano-robotic platform. It is mainly composed of a poly-articulated nano-robotic system actuated by piezoelectric inertial actuators (PIAs) and holding a self sensing Atomic force Microscope (AFM) probe as end effector. Several robotic scientific issues have been tackled. The main contributions are:

- Non-linear modeling of piezoelectric inertial actuators to deal with multi-scale dynamic representation issues.

- Velocity characterization and velocity control of a class of piezoelectric inertial actuators

- High level multi-scale path following control of an AFM operating inside electron microscopes.

- AFM tip localization and tracking through deep learning based vision inside an electron microscope.

- Model predictive control (MPC)-based path following and obstacle avoidance for an AFM cantilever operating inside electron microscopes.

The developed methods enrich the motion capability and sensing of nano-robotic systems operating inside SEMs, accelerating the process towards a fully-automation for robotic manipulation purposes at the small scales.

Keywords: Nano-robotics, automation, velocity control, path following, deep learning, model predictive control, scanning electron microscopy.

Contents

List of Figures

General introduction

Nano-robotics has become a key tool to face the current challenges in micro/nano technologies for both industry and academic research. It has been applied in a wide range of emerging domains, such as nano-material characterization, nano-assembly and cell manipulation. Automated and batch productivity with micro/nano-robots is a critical issue to meet the massive and potential market windows. To achieve complex and advanced robotic tasks, a remarkable amount of works in motion planning, control, evolution and learning methods has been developed and successfully applied on macro scale robots. However, there is still a huge gap between these cutting-edge theories and their possible implementation to nano-robotics. This issue is still an open research subject in the community. The reasons are mainly lying on the fact that the working principles between nano-robotics and macro robotics are totally different as well as the complex working environment at the small scales. In addition, there are several critical issues related to the lack of observation data in the small scales compared with the abundant sensing choices for conventional robots.

The mainstream is the combination between nano-robotic systems and Scanning Electron Microscopy (SEM) and to achieve robotic tasks in such an environment in automated ways. This choice is mainly motivated by performance that classical optical microscopy cannot offer, i.e. the nano-metric imaging resolution and the depth of field which is necessary to simultaneously observe tools and samples. Automated control can be divided in two layers, the high level control layer and the low level control layer. The high level control consists on decision making, motion planning, task assignments and so on, according to the fusion between multiple sensing cues such as vision, position, velocity and force measurements. The low level control layer is in charge of controlling the dynamics of the robot and the end effectors to execute a task defined by the high level controller.

The works related in the literature have tackled very interesting critical issues of robotic at the small, but they have been made successfully thanks to the experience of the operator in the filed. So the question is: **is it possible that all the cited applications are programmed by a child of 10 years old?** So, if the reply is YES (and it is YES), that means that nano-robotic technology inside SEM can be used by any operator from any field. This is fundamental for a widespread use of robotic systems inside EMs in a broad scientific community and not only from computer scientists/roboticists. This is possible provided that an advanced user friendly interface is built to allow programming robotic tasks by a succession of elementary path following tasks that manage all the unpredictable and no totally observable situations such as probes landing on the substrate, obstacles avoidance, trajectory optimisation, stop motions to avoid unwanted collisions, intelligence and so one. These are just few exemples of tasks that HAVE TO BE MANAGED by an advanced high level controller. There is still a plenty of improvement space for nano-robotics automation inside SEM in order to achieve more generic, intuitive, intelligent and autonomous robotic tasks in such an environment. The improvement varies from detection, modeling and control to decision making, planning and emergency reaction.

This thesis targets the development of a generic, intelligent and user friendly interface that can manage elementary robotic tasks needed inside a SEM by simply defining graphical instructions on the SEM screen. All these motion control must deal with *multi-scale trajectories*, i.e. trajectories in the nano-meter range up to the milliliter range. In this case, the piezoelectric inertial actuator (PIA) is the most promising type of actuator for such robots.

These technical challenges require to deal with several robotic scientific issues that have not

been solved in the literature. For the thesis, the end effector is a self sensing AFM. The issues are:

Issue 1: due to the very high magnification capability of SEM, to be able to reach any region of interest on sample observed by an SEM, the AFM probe must have the capability to navigate with a displacement range to resolution ratio of several million times. The AFM probe must be able to move on a distance of several mm or cm to reach any region on a sample as well as of few nm to operate in a narrow area. No solution was available in the literature to control in an automated way the position of an AFM probe with such a high range to resolution ratio.

Contributions:

- Non-linear model of PIAs is proposed to deal with multi-scale dynamic representation issues. It describes the mathematical relation between the input voltage applied to a piezoelectric element and the displacement of the associated slider. The model is based on a coupled piezo/friction hysteresis model and an augmented elasto-plastic friction model for which the breakaway displacement depends on the frequency and the amplitude of the input sawtooth voltage. This dependency is highlighted experimentally and represents the main novelty in friction modeling compared to the state of the art.

- Velocity characterization and velocity control of a class of PIAs is studied. The achievable velocity range of PIAs is characterized in air and vacuum environments. This analysis allows the definition of a detailed map of the velocity characteristics in forward and backward motion directions. Velocity control strategies are then studied based on an instantaneous velocity feedback and an average velocity feedback. The work on the velocity characterization and control has been the key for path following control and model predictive control that has been studied thereafter.

Issue 2: for AFM tracking using SEM vision, one has to consider specific issues related to the compromise between the scan speed and the image quality of SEM. This restriction seriously limits the performance of conventional vision tracking algorithms such that those based on Template Matching when used with electron images. At high scan speed, the image quality is very noisy making very difficult to differentiate the AFM tip from the background, hence limiting the tracking capabilities. In this thesis, we have explored for the first time the potential value of deep learning in the context of nano-robotic vision tracking inside SEM.

Contributions:

- High level multi-scale path following control of an AFM cantilever operating inside electron microscopes.

- Atomic force microscope tip localization and tracking through deep learning based vision inside an electron microscope.

Issue 3: during the navigation of the AFM inside the SEM, it is often needed to avoid obstacles. This is for instance the case when the trajectory is delimited by virtual guides. The issue is that if the obstacle is detected when the AFM tip touches it, i.e detection by force sensing, it is too late to avoid it in a secure way. The only solution is to predict it by vision, to

let an interval of time for a secure obstacle avoidance with controlled dynamics. We propose in this thesis for the first time a model predictive control-based obstacle avoidance for AFM with SEM vision feedback.

Contribution:

- Model predictive control (MPC)-based path following and obstacle avoidance algorithm for AFM cantilever operating inside electron microscopes.

The thesis is organized as follows: **Chapter 1** reviews recent advances in robotics at the small scales operating inside EM and their relevant impact in micro/nano- applications. It gives a sighted to the reader about what is possible nowadays with such instruments and it shows the chalenges for automated programming of robots inside SEM. **Chapter 2** lays the foundations for the low level closed loop position and velocity control of the ISIR-robotex nano-robotic platform. It presents a non-linear model of PIAs to deal with multi-scale dynamic representation issues. Issues related to multi-scale position control and velocity controls are then studied. **Chapter 3** addresses the issue of high level multi-scale path following control of an AFM cantilever operating inside electron microscopes. The aim is to control the trajectory of the cantilever driven by a PIA using both electron microscope images and velocity measurements from optical encoders. To do so, we have studied the issues related to the real time localization and tracking of an AFM cantilever from SEM images for any scan speed configuration and despite of low images quality. **Chapter 4** adresses the issue of Model predictive control (MPC)-based path following and obstacle avoidance of AFM cantilevers operating inside a SEM.

Publications

S. Liang, M. Boudaoud, B. Cagneau and S. Régnier. Velocity characterization and control strategies for nano- robotic systems based on piezoelectric stick-slip actuators. **IEEE International Conference on Robotics and Automation (ICRA)**, Singapore, 2017.

S. Liang, M. Boudaoud, C. Achard, W. Rong, S. Régnier. Atomic force microscope tip localization and tracking through deep learning based vision inside an electron microscope. **IEEE/RSJ International Conference on Intelligent Robots and Systems (IROS)**, Macau, China 2019. (accepted)

S. Liang, M. Boudaoud, B. Cagneau and S. Régnier. Path Following Based On Velocity Control For Inertial Actuated Nano-Robotic Systems Inside Scanning Electron Microscopy. **IEEE Transactions on Automation Science and Engineering**. (in preparation)

S. Liang, M. Boudaoud, P. Morin, C. Achard, W. Rong and S. Régnier. Model predictive control (MPC)-based path following and obstacle avoidance algorithm for AFM cantilever operating inside electron microscopes. **IEEE International Conference on Robotics and Automation (ICRA)**, 2020. (in preparation)

M. Boudaoud, **S. Liang**, T. Lu and S. Régnier. Voltage/frequency rate dependent modeling for nano-robotic systems based on piezoelectric stick-slip actuators. **IEEE International Conference on Intelligent Robots and Systems (IROS)**, Deajeon, South Korea, 2016.

M. Boudaoud, T. Lu, **S. Liang**, R. Oubellil and S. Régnier. A voltage/frequency modeling for a multi-DOFs serial nano-robotic system based on piezoelectric inertial actuators . **IEEE/ASME Transactions on Mechatronics**, Vol 23, 2814 - 2824, 2018.

J. Cailliez, M. Boudaoud, **S. Liang**, and S. Régnier. A multi-model design for robust hybrid control of non-linear piezoelectric actuators at the micro/nano scales. **American Control Conference (ACC)**, Milwaukee, USA, 2018.

M. Al Janaideh, M. Boudaoud, M. Al Saaideh, **S. Liang**, and S. Régnier. Inverse Hysteresis Control of Stick-Slip SEM Integrated Nano-Robotic Systems. **IEEE International conference on Decision and Control (CDC)**, Nice, France, 2019. (accepted)

J. Cailliez, M. Boudaoud, **S. Liang**, and S. Régnier. Robust multi-model hybrid control of a self sensing atomic force microscope at the nano-scale. **IEEE Transactions on Control Systems Technology**. (under review)

Chapter 1

Nano-robotics inside SEM

In order to use a manipulation robotic system at the nanometer scale, the positions of the tools and the end effectors relative to the objects with which they interact need to be observed in a fairly precise manner. Choosing Electron Microscopes (EMs) is advantageous in this regard. This chapter reviews recent advances in robotics at the small scales operating inside EM and their relevant impact in micro/nano- applications. Robotic tasks inside EMs do not concern only people from the fields of robotics but more generally scientists from broad disciplines that do not have necessary the required skills for advanced programming of complex robotic tasks inside EMs. As it will be shown in this chapter, whatever the complexity of the tasks, it is always composed of a succession of several elementary simple positioning tasks of the end effectors and or the background. The breaking approach targeted in this thesis is to open a new way to achieve automated tasks at the small scales inside EMs that any operator can programs by simply drawing elementary paths with a mouse click on a computer screen displaying the magnified electron images. If the robotic end effectors can follow these paths accurately in a secure way, programming a manipulation task at the small scales inside EMs would become a child's play. The need of advanced user-friendly interfaces for robotic tasks programming inside EMs is the key for a widespread use of robotic systems inside EMs. Such interfaces require however to tackle several robotics scientific issues that have not been solved in the literature and that represents the heart of the thesis.

1.1 Electron and atomic force microscopy for the observation of the small worlds

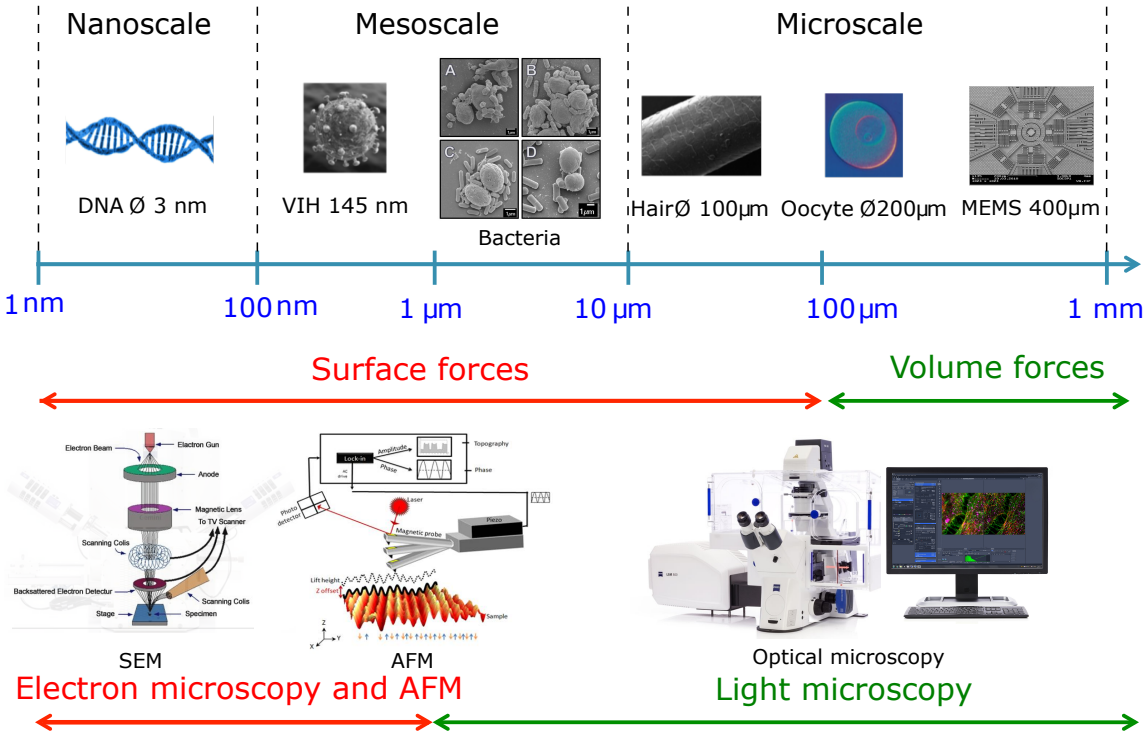

Figure 1.1: Comparison between multi scales in micro world [47].

When tackling micro/nano-robotics, one has to consider several constraints in terms of interaction forces, actuation and sensing principles (Fig. 1.1). The small scales can be classified into nanoscale (1 up to 100nm), mesoscale (100 nm up to 10 μm) and microscale (10 μm up to 1mm) [47]. Due to the scale effect, surface forces are predominant between 1 nm and 100 μm while volume forces have more importance beyond 100 μm. Electron microscopy (EM) and Atomic Force Microscopy (AFM) are ideal observation tools below 1μm.

Various types of microscopes are available when it comes to observing the micro and nano worlds. They rely on distinct physical principles of operation, interacting directly or indirectly with the objects to observe and then reconstructing the resulting image. Which type of microscope should be used depends on the goals; the microscopes relevant to the nano-scale are:

1.1.1 Electron Microscopy (EM)

It relies on electrons instead of photons. Electrons are emitted by a field electron emitter gun or a thermionic field gun. As with photonics microscopy, these electrons can be reflected (SEM: Scanning Electron Microscopy) or transmitted (TEM: Transmission Electron Microscopy). The electron beam interacts with matter as it hits it, which results in emissions. These emissions are intercepted by specific sensors, and treated so as to reconstruct an image of the object's surface, topography, atomic composition and so on. A SEM can reach sub-nanometer resolutions, and a TEM can go below a tenth of that on thin samples. SEM can be used for the observation of

solid materials and prepared biological cells in high vacuum conditions (i.e. 10^{-6} Pa), for frozen cells using CryoSEM technology and for no frozen and no dried cells using the variable pressure SEM (VP-SEM). EM allows the observation of the inner structure of unroofed cells but their main drawback is that they do not provide tridimensional images, which is an impediment for the definition of the thickness of nanoscale structures.

1.1.2 Atomic force Microscopy (AFM)

It is based on the work of Binnig, Nobel Prize of physics 1986. AFM uses tools of various natures, sizes and operating principles, which have in common that they probe the observed surfaces with a stiff tip. The apex of this tip is of a nano- or micrometer scale and is brought very close or even in contact with the zones of interest. This microscope is useful to get various kinds of data such as adhesion, elasticity, viscosity and topography of small-scale samples.

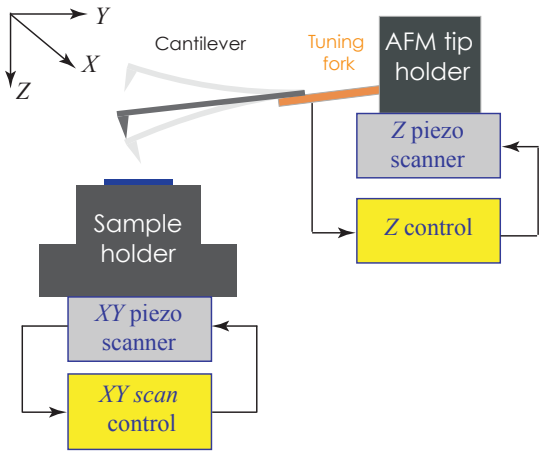

Figure 1.2: Simplified scheme of an AFM using a frequency shift detection from a tuning fork. The AFM can operate by controlling the XYZ positions of the AFM tip holder or that of the sample holder.

The AFM is generally mounted on a piezoelectric scanner that can either moves the AFM probe or moves the sample in X, Y and Z directions. Depending on the application, it can operate following different operating modes. The three main AFM modes are contact mode, intermittent contact (or tapping), and non-contact modes. In contact mode, the force on the tip is repulsive. The probe-surface separation is less than 0.5 nm. By moving the Z position of the probe in a way to maintain the force between the probe and the sample constant an image of the surface is obtained. One disadvantage of this mode is that forces can damage and deform soft samples. In non-contact mode, the probe does not enter in contact with the sample surface, but oscillates above the sample. Using a feedback loop to monitor changes in the amplitude due to attractive VdW forces, the surface topography can be measured. This mode will not suffer damage to the sample, but usually need ultra high vacuum (UHV) to have best imaging. In tapping mode, the cantilever is oscillated at its resonant frequency and the probe lightly taps during scanning on the sample surface. The tip only contacts the surface briefly during each oscillation cycle. This mode is perfect for biological samples such as polymers and DNA, as well as numerous other fragile samples. Fig. 1.2 shows a simplified scheme of an AFM using a frequency shift detection from a tuning fork. The AFM can operate by controlling the XYZ positions of the AFM tip

holder or that of the sample holder.

1.2 Nano-robotics inside SEM

A series of robotic applications involving SEM have been reported in the literature. One can cite works related to electrical and mechanical characterization of nano-matarials [120] [164] [49] [137] [101] [120], MEMS and NEMS assembly [35] [152] [143] [146], biological cell manipulation and/or characterization [44] [127] [5], pick and place of small scale objects such as colloidal particles [163] and carbon nanotubes (CNTs) [133]. The common point between these applications is the need of corse and fine positioning capabilities of the robotic system and a SEM vision feedback. Such robots often have multiple degrees of freedom and are composed of specific actuation and sensing mechanisms. Some example of commercial nano-robotic systems designed by companies such as Zyvex, Kleindiek, SmarAct, Toronto Nano Instrumentation, Physik Instrumente and attocube are shown in Fig. 1.3 [143] [154] [43] [150] [159] [56] [114] [75]).

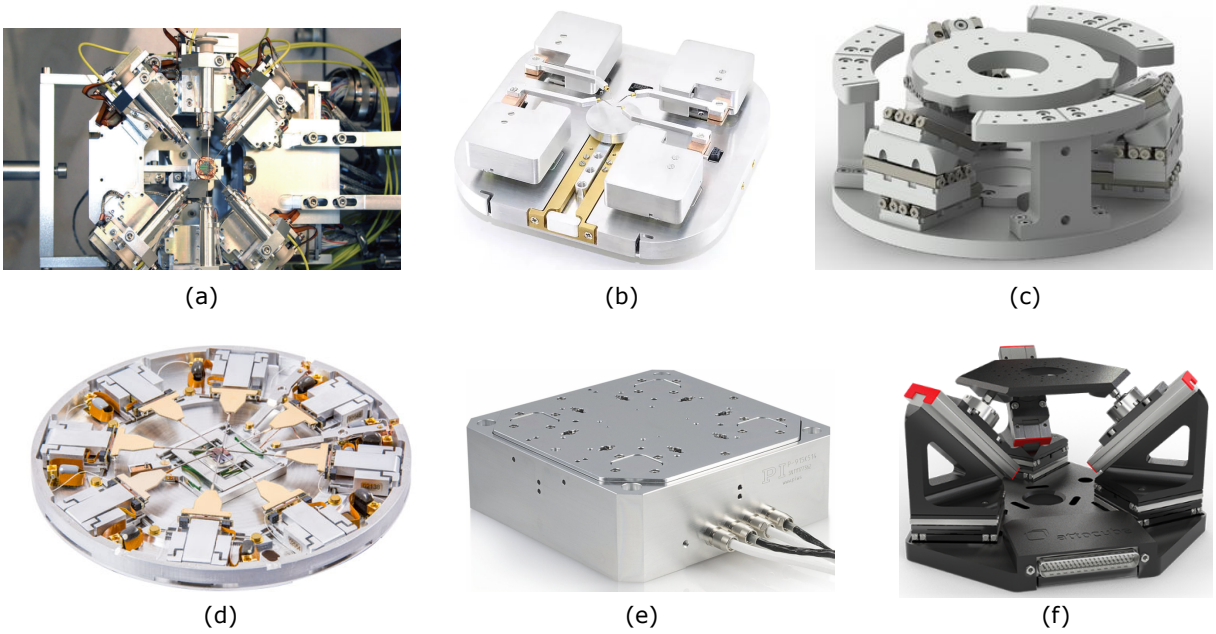

Figure 1.3: Commercial nano-manipulation systems. (a) Zyvex. (b) Toronto Nano Instrumentation. (c) SmarAct. (d) Kleindiek Nanotechnik, (e)Physik Instrumente (PI). (f)attocube [132].

1.2.1 Actuation

Because of SEM's working principle, only specific actuators can be used. They must be vacuum-compatible and being insensitive to the electron beam. They must also be able to achieve a very high displacement to resolution ratio, typically several millimeter travel range for coarse positioning tasks and few nanometers for high precision fine positioning tasks. Performance comparison between micro/nano-actuators can be observed in Fig.1.4. Piezoelectric actuators have been increasingly applied thanks to their desirable properties such as fast dynamics, high resolution,

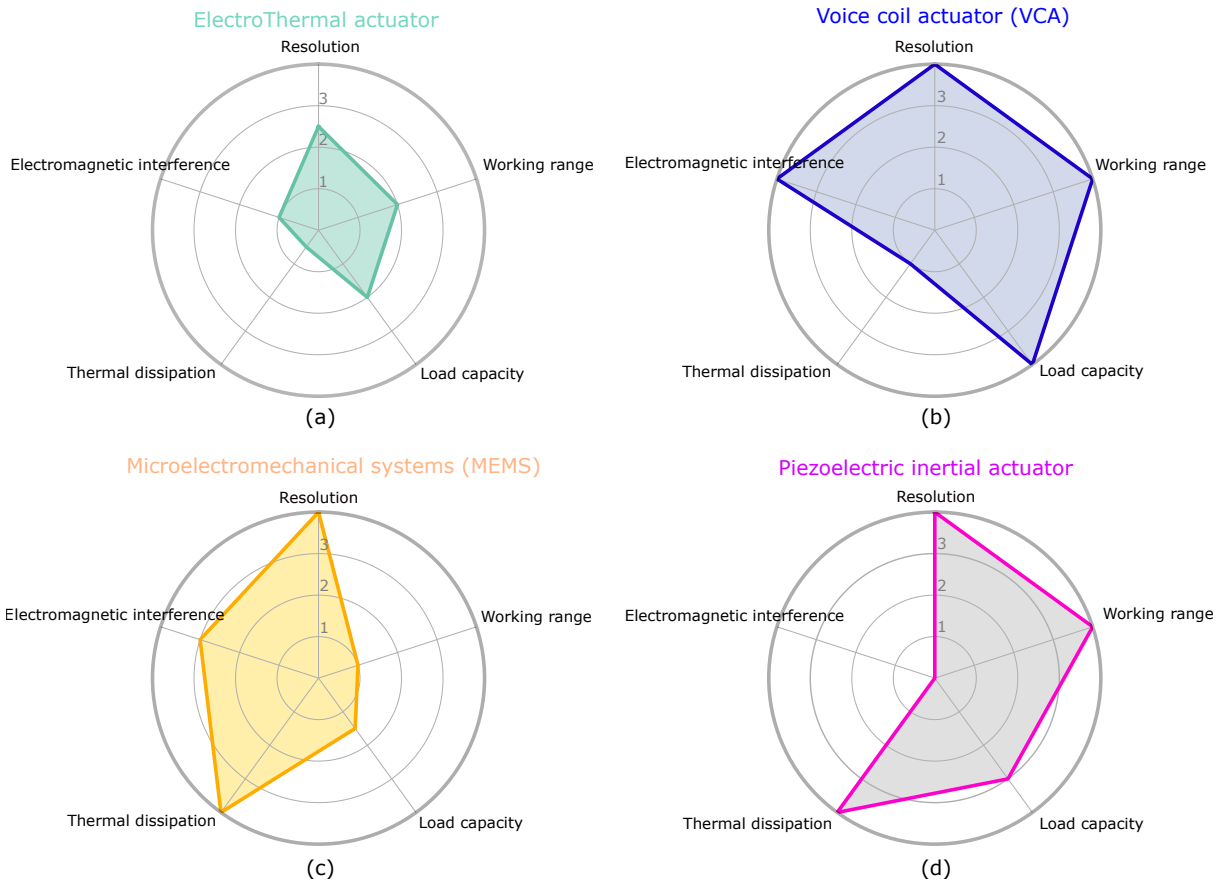

Figure 1.4: Performance comparison between micro/nano-actuators. (a) ElectroThermal actuator. (b) Voice coil actuator (VCA). (c) Microelectromechanical systems (MEMS). (d) Piezoelectric inertial actuator.

high power-to-weight ratio and compact size. Especially, Piezoelectric Inertial Actuators (PIAs) are one of the best candidates to produce a high motion range to resolution ratio.

PIAs can be classified into three families [69] [25]: ultrasonic, inchworm, and stick-slip. They share common characteristics: (i) their motion are friction driven, (ii) the travel range is only related to the length of the slider's guide and (iii) holding force arises from friction without power consumption. However, they are different in working principle and performance [23].

Actuator	Controllability	Force	Speed	Reference
Ultrasonic	Medium(need of track resonance)	Press-dependent	$>100mm/s$	[61]
Inchworm	Low(multi-phase synchronization)	$>15N$	$>1.5mm/s$	[82]
Stick-slip	High(only one control channel)	dozens of N	10-50mm/s	[73] [100]

Table 1.1: Comparison between perzoelectric actuators.

The ultrasonic actuator is based on the excitation of stator's resonance. This resonant vibration is typically elliptical [141] [62]. By changing motion phase shift among piezo components,

motion direction can be altered. Typical ultrasonic actuators are characterized by a high speed capability ($>$ 100 mm/s). From a control point of view, such actuators are characterized by a medium controllability and the control unit can be complex to realize due to the need to track resonance [27] in the case of load variation. A typical inchworm actuator has two groups of piezo stators. When one group sticks to slider (i.e. load) and guides its motion by deformation, the other group is not in contact with the slider and prepares for the next stick motion. The quality of the resulting motion relies on the driving frequency and the phase shift among stator groups. Thus, synchronization among piezo stators must be accurate [83] [93]. The advantage is that such actuators can produce a motion with a high resolution and a high output force. The main limitation lies in its low speed ($<$ 10mm/s). From a control point of view, the need of a multi-phase synchronization can lead to a high cost and an engineering complexity. The working principle of a stick-slip actuator takes advantage of the competition between friction force and inertial force. It can be operated in hybrid mode (scanning or stepping) depending on the choice between high resolution and large motion range [18] [147] [134] [46]. Compared to the other two classes of actuators, a stick-slip actuator provides medium speeds (10-50 mm/s). Without any need of multi-phase synchronization, such an actuator possesses only one piezoelectric channel. This is a major advantage, which lowers the cost, simplifies controller design, and leads to a better miniaturization potential. Based on the simplicity and versatility described above, Piezoelectric Stick-Slip (PSS) is one of the most commonly used actuation principle for nano-robotic systems. The performances of PIAs are summarized in Table 1.1.

Working principle of a Piezoelectric Stick-Slip (PSS) actuator: a PSS actuator is mainly composed of a Piezoelectric Element (PE), a slider with one translational or rotational DOF, and a friction material located between the PE and the slider (Fig. 1.5). The slider is used to carry a load. Several PSS actuators can construct a multi-DOFs kinematic structure. The friction force F_f drives the motion of the slider.

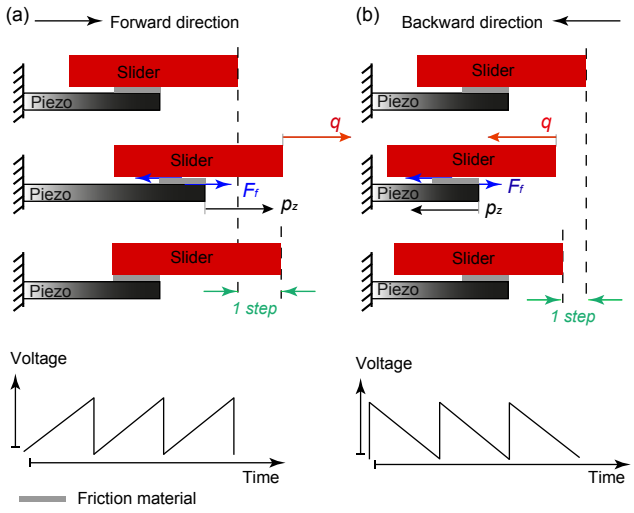

Figure 1.5: Piezoelectric stick-slip actuator driven by sawtooth signal. (a) Motion in the forward direction. (b) Motion in the backward direction.

This actuator has two main motion phases. Stick phase is produced by a slow deformation of the PE, the slider sticks to the motion of PE. Slip phase results from an abrupt deformation of the PE leading to a relative motion between the PE and the slider. If only the stick phase is involved, the actuator is moving in *scanning mode*. This operating mode is useful for a high

positioning resolution but the stroke of the slider is limited by the maximal deformation of the PE. If stick and slip phases are used alternatively, the actuator is moving in *stepping mode*. This mode allows a large motion stroke but with a lower resolution. The alternate stick and slip phases are often obtained when the PE is fed with a sawtooth voltage. Usually, for PSS actuators with a linear motion profile, the slider has one translational DOF. If the sawtooth voltage is featured by a slow rise and an abrupt drop, the resulting motion direction will be referred to as *forward direction*. If the sawtooth voltage is featured by an abrupt rise and a slow drop, the motion direction will be referred to as *backward direction*. They are illustrated in Fig. 1.5.

1.2.2 Sensing

Due to the vacuum-working environment of SEMs, one has to consider the heat dissipation issues of sensors to be used inside these microscopes. Typically, for SEM integrated nano-robotic systems, different kinds of sensors can be used for position/velocity measurements, force measurements and depth measurements Fig. 1.6.

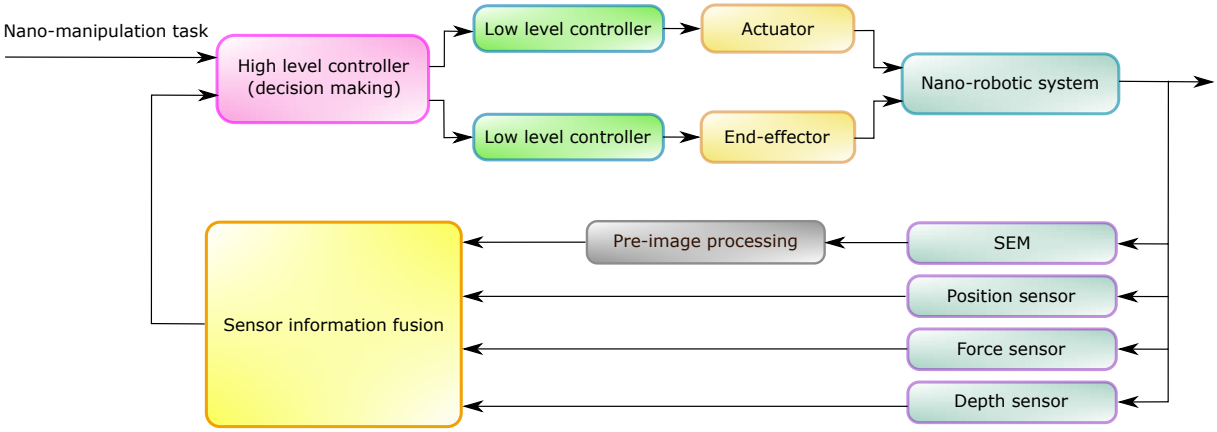

Figure 1.6: Nano robotic control scheme inside SEM.

1.2.2.1 Position measurement

There are mainly three kinds of sensors that can be integrated in piezoelectric actuators, namely capacitive sensors, optical encoder-based sensors and strain gauge-based sensors.

Piezoelectric actuators have nonlinear properties such as the hysteresis and the creep [59], which lower down the accuracy and the stability of the nano-manipulators. The compensation of such non-linearities with feedback controllers and/or with inverse hysteresis models is nowadays well mastered. Capacitive sensors provide a non-contact and a low power displacement measurement, with a nanometer resolution and a wide bandwidth up to 10 kHz. However, they are expensive and they allow position measurement in a very limited working range within a couple of millimeters [40]. Strain gauges suffer from the thermal drift issues. Optical encoders are able to measure displacements in the centimeter range with a nanometer resolution. They are usually combined with an interpolation circuit and a counter to provide a position or a velocity measurement. They are ideal for stick and slip actuators but they also suffer from thermal drift because optical elements generate heat.

1.2.2.2 Force measurement

Forces sensors are useful to provide a force feedback during a manipulation task. Several kinds of force sensors can be used based for instance on MEMS technology or AFM. With MEMS technology, the capacitive measurement principle is used to measure the displacement of a probe. The force measurement is deduced from the displacement measurement by the knowledge of mechanical suspensions stiffness. This method tends to provide smaller sensors with the need of little control electronic, leading to more integrated sensors. A trade-off between the measurement range and the resolution is often involved. With AFM technology, small and shap cantilevers can be used as end effectors to manipulate objects while providing in real time force informations. To be integrated in the analysis chamber of a SEM, it is preferable to use compact self sensing AFM probes.

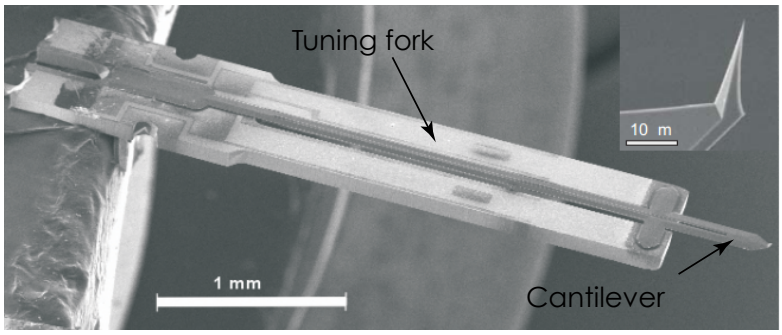

Figure 1.7: Simplified model of the Akiyama A-probe Tunning Fork, composed of the AFM cantilever integrated on the tuning fork, [136].

A self-sensing and self-actuating (-exciting) probe can be based on a quartz tuning fork (TF) combined with a micro-machined cantilever for dynamic mode AFM, Fig. 1.7. One example of commercially available self sensing AFM probe is the Akiyama-probe. This tuning fork-probe is made of two coupled resonators, i.e. the tuning fork and the cantilever. The typical resonance frequency of the silicon cantilever is $\sim$ 50 kHz and that of the tuning fork before the cantilever was glued is $\sim$ 32 kHz.

1.2.2.3 Depth measurement

The vertical manipulation in SEM keeps being a challenging and tricky issue having not been reasonably solved, due to the lack of depth information. Depth measurement or estimation can be used to safely land the end-effector on substrates to be able to perform manipulation tasks afterwards. Depth measurement can be divided into two methods, namely vision based and force measurement based [63] [89] [154] [154] [117] [133] [37] [88] [140] [140] [154] [39]. In addition, the depth measurement is of importance to calibrate the end effectors relative to the SEM images. The end effector can be for instance an AFM cantilever (Fig. 1.8).

Electron microscopes usually provide a two dimensional image of the sample with a scale bar indicating the horizontal dimensions along x and y axes of the image. However, the image does not provide information about sample feature height or the vertical distance between the probe tip and the sample. Hence, to guide a probe tip under the microscope towards a desired point on the sample, one has to use a manipulator and sensors attached to the tip to detect contact

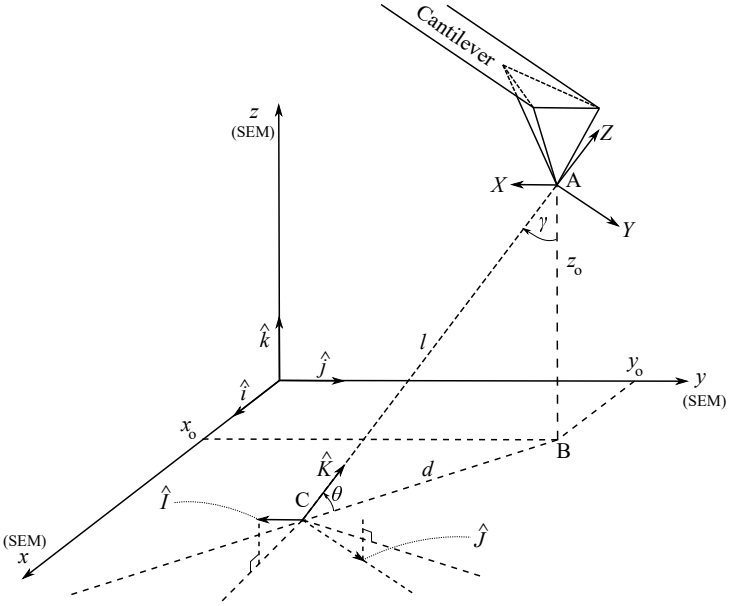

Figure 1.8: Three dimensional schematic diagram of SEM and AFM cantilever coordinates.

with the sample or observe alternative signs such as probe shadow on the sample just before the contact and horizontal sliding of the tip on the sample just after colliding it [116]. In addition, if a microscope is not provided with a built-in sample manipulator or the manipulator does not meet the desired precision, the user may have to incorporate another positioner in the microscope for sample manipulation and nano-probing. Hence, coordinates of the image and microscope may not be well aligned with those of the micro-manipulator. Ignoring such misalignment can create unacceptable positioning error after guidance of the probe tip to a target point on the sample or even damage the probe and sample. Hence, to increase the precision and speed of operation in nano-porbing applications, it is essential to address this misalignment problem in a systematic way.

1.2.3 Control strategy

For nano-robotic tasks inside SEM, a systematic control scheme must be implemented taking advantage of multiple sensing feedbacks as described in Fig. 1.6. The control structure is mainly divided into two parts. The decision making layer referred as *high level control* is in charge of selecting and monitoring the tasks such as a Sequential function chart (SFC), a path planning, a path following and a deep learning. The dynamic control referred as *low level control* is in charge of controlling the dynamics of the robot and the end effectors to execute a task defined by the high level controller.

1.2.3.1 Position control

The state of art has shown that for PIAs several control issues related to the nonlinear behavior and the hybrid operating mode of these actuators still require studies in order to satisfy the demanding performance in nanotechnologies. Existing control strategies can be classified into

control in scanning mode and control in stepping mode.

The objective of the control in scanning mode is to reduce the hysteresis effect and to damp the vibrations [52]. Hysteresis may induce open-loop positioning errors as high as 10%-15% of the displacement range [71]. Furthermore, oscillations of a hundred nanometers at the fundamental resonance frequency can be observed in the slider displacement [84]. Open-loop strategies can be used for hysteresis compensation [51, 142] [65, 108, 157] and vibration damping [92, 109]. However, in practice, it is difficult to obtain precise compensators, and hence to guarantee positioning accuracy. Also, these methods are not robust against hysteresis variations and shifts in the resonance frequency. For these reasons, numerous closed-loop control strategies have been studied in the literature, including pole-placement [70], PID control [41], H_∞ control [123, 139] [12], sliding mode control [74], LQG control [105], and so on. On the other hand, few techniques exist in the literature to control PSS actuators in stepping modes. A frequency proportional controller is proposed in [24] where the frequency of the sawtooth control voltage is chosen based on the tracking error. A cascade controller is designed via dehybridization in [124] using a hybrid model of the actuator. In the inner-loop, a hybrid controller is designed to impose a time-scale separation between continuous and discrete states. In the outer-loop, a continuous proportional derivative controller is developed using an approximated continuous model of the inner-loop in order to satisfy closed-loop stability. A frequency/amplitude proportional controller is presented in [110] to control the amplitude and the frequency of the sawtooth control signal separately. The proportional gains are determined in the same way as for classical proportional controllers. None of the existing controllers has dealt with the stepping/scanning switch problem of PSS actuators. The first ever results on mixed Stepping / Scanning mode control of stick-slip SEM-integrated nano-robotic systems has been proposed in [98].

1.2.3.2 Velocity control

Specific driving methods of PIAs are needed to obtain a smooth motion trajectory through velocity control. This is of primary importance to achieve a path following as it will be explained in Chapter 3. However, the only two references in the literature dealing with velocity control of PIA are [57] [73]. The second reference is a part of this thesis that will be explained in Chapter 2. In the first reference, Hunstig et al. [57] proposed some driving methods of PIAs to obtain smooth motions while avoiding the slip vibrations. These driving methods are evaluated considering three main criteria, namely the steady state velocity, the smoothness of motion, and the start-up time. Liang et al. [73] have made a characterization of the velocity of PIAs with respect to the amplitude and the frequency of the input sawtooth voltage to evaluate the reachable velocities that can be used a an input reference in a closed loop control. Velocity control based on an instantaneous velocity feedback and on an average velocity feedback has then been studied. The latter one has shown better results in terms of motion vibration damping. The average velocity control described in [73] will be used in this thesis as a part of the path following control.

1.3 Nano-robotic Application inside SEM

The aim of this section is to report some applications of robotics at the small scales inside an electron microscope. The applications are divided into three categories, namely "Nano-

materials manipulation and characterization", "Nano-assembly" and "Cell characterization and manipulation". The presented examples are of course non exhaustive. It gives a sighted to the reader about what is possible nowadays with such instruments.

1.3.1 Nano-materials manipulation and characterization

For such applications, several works can be found. Fig. 1.9 illustrate some of them. There are two main types of characterization, the mechanical and the electrical one.

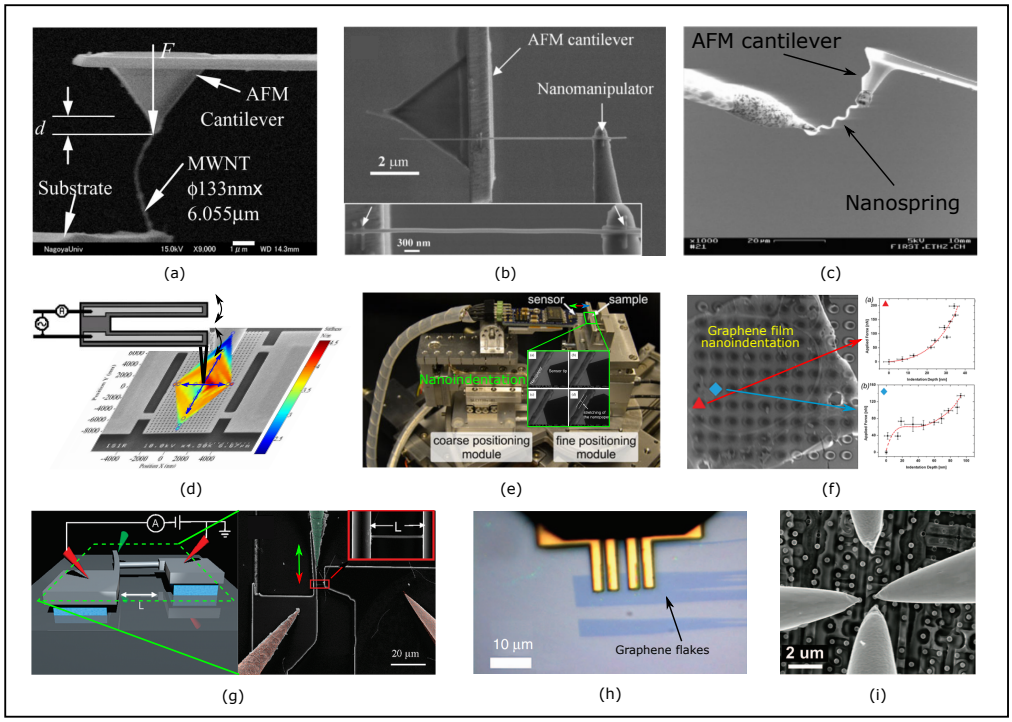

Figure 1.9: Nano-robotic applications involving mechanical and electrical manipulation and characterization of nano-materials [132]. (a) Mechanical characterization of MWNTs [43], (b) nanowires [159], (c) nanosprings [17]. (d) Mechanical characterization of 2D materials of graphene films [3]. (e) nanopapers [91]. (f) suspended InP membranes [161]. using nanoindentation and contactless measurements. (g) Electrical characterization for nanowires. (h) [160]. graphene flakes [86]. (i) single transistors on IC chips [137].

The mechanical characterization aims at estimating some mechanical properties of nano-materials such as the Young modulus. One can cite exemples with Multiwalled Carbon Nanotubes (MWNTs) [43], nano-wires [159], nano-springs [17], graphene films [3], nano-papers [91]. The electrical characterization aims at providing electrical properties of nanomaterials such as the conductivity. One can site the case of nano-wires [160] or single transistors on IC chips characterization [137].

The mechanical characterization can be done by indentation or stretching of nano-materials using probes such as AFM cantilevers. The electrical characterization can be done by bringing a conductive probe on the nano-material and passing a current through it.

1.3.2 Nano-assembly

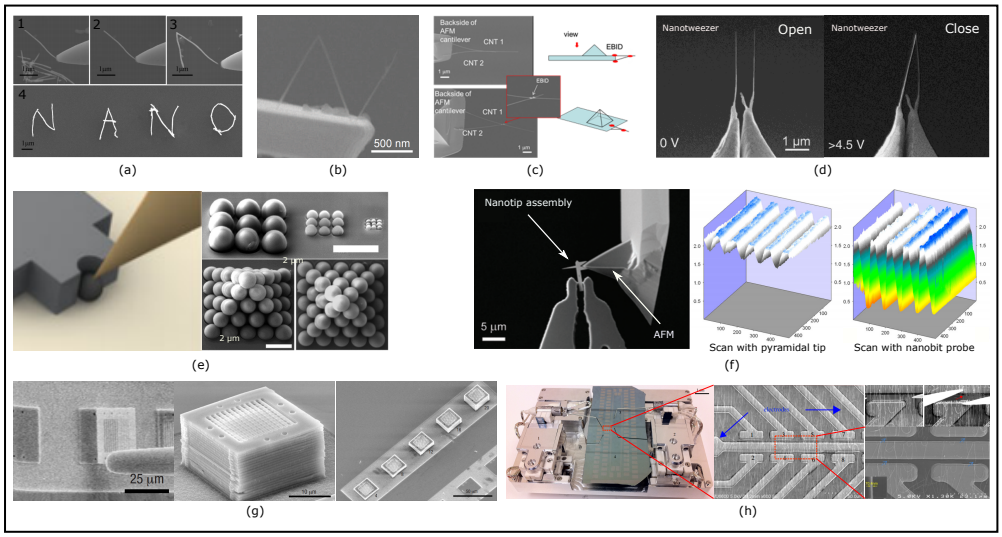

Figure 1.10: Nano device and nanostructure assembly [132]. (a) Nanowires pick, place and assembly [102]. (b) MWCNT assembled as a 3D letter with EBID [45]. (c) and (d) A thermal sensor [148] and nanoscaled tweezer assembled by nano-manipulation [11]. (e) 3D pyramidal spheres assembly [163]. (f) High-aspect-ratio AFM cantilever tip assembly for high-resolution imaging [66]. (g) Assembly photonic plates as a 3D photonic crysta device [14]. (h) Nanowire field-effect transistors (nano-FETs) automated nanomanipulation to remove extra and maintain one-nanowire format [152].

With a precise positioning of end effectors using multi-DOF capabilities, the nano-robotic manipulator can achieve assembly tasks of various nano-devices. For instance, in Fig. 1.10(a), a pick-and-place manipulation was executed by two nano-probes to distribute and solder golden nano-wires on a pattern of 'NANO' [102]. A 3D letter 'N' consisting of MWCNT was constructed by cutting and bending processes from EBID, and assembled via nano-manipulation [45] [78] [79] (Fig. 1.10(b)). In Fig. 1.10(c), a thermal sensor composed of two MWCNTs is mounted on an AFM cantilever realized by EBID and nano-manipulation [148]. Two nanotubes were manipulated and assembled as a nanotweezer and finally mounted on a special Si tip patterned with metal electrodes [11] (Fig. 1.10(d)). As shown in Fig. 1.10(e), a 3D pyramidal structure composed of stacked silica spheres was constructed by a cooperative assembly process of two nano probes [162]. The pick and place control is conducted by the coorperation between a tungsten probe and a modified piezoresistive AFM cantilever featured with a spherical adhensive pocket tip. A nanotip held by a microgripper was assembled and soldered on an AFM cantilever tip by EBID technique. This forms a high-aspect-ratio AFM cantilever tip, for a high-resolution topography imaging [66] (Fig. 1.10(f)). To produce a 3D photopic crystal device (Fig. 1.10(g)), a thin plate was disassembled from a substrate with the connection bridge broken by a nano-probe [14]. It is then reassembled (Fig. 1.10(g)). In Fig. 1.10(h), a fabrication method of nanowire field-effect transistors (nano-FETs) is proposed using nanowire contact printing [152].

1.3.3 Cell characterization and manipulation

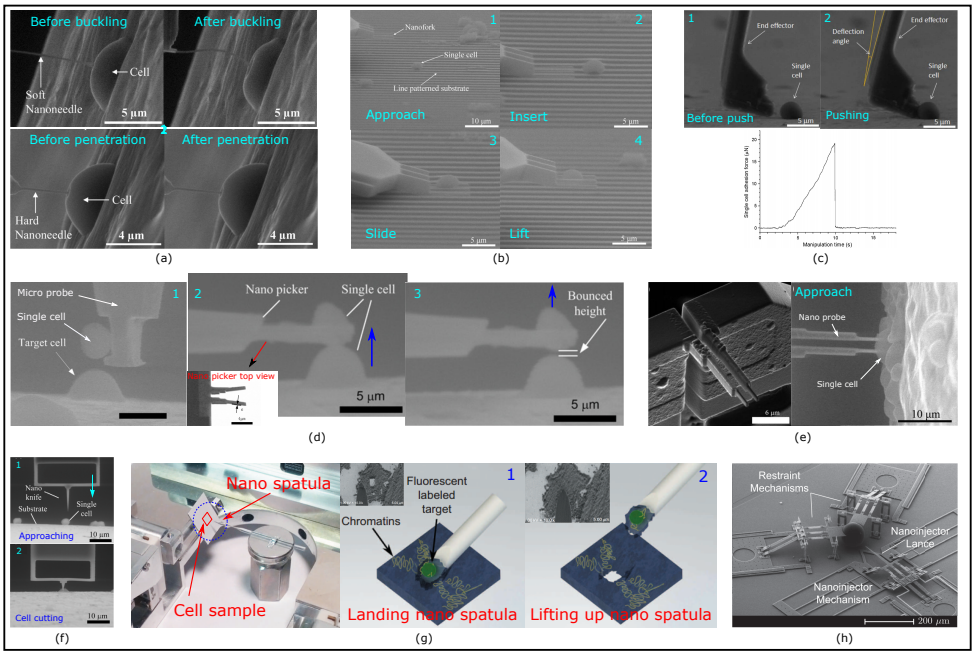

Figure 1.11: Cell characterization and manipulation inside an ESEM and SEM, [132]. (a) Cell stiffness measurement [8]. (b) Cell–substrate tested by nano-fork [6]. (c) Cell–substrate tested by nano-putter [126]. (d) Cell–cell adhesion force determination [128]. (e) Intracellular electrical measurement for viability test [5]. (f) Single cell cutting [130]. (g) Chromatin extraction [28]. (h) Self-reconfiguring metamorphic nanoinjector for injection into mouse zygotes [15].

FIB etching and deposition techniques are carried out to convert the standard AFM cantilevers into various types of functional tools such as a soft buckling nanoneedle [7] [8] [10], a nano-fork [6] and a nano putter [129] as shown in Fig. 1.11(a), Fig. 1.11(b) and Fig. 1.11(c). These tools were controlled by nano-manipulators in Environmental Scanning Electron Microscopes (ESEM) to identify and determine the cell stiffness and viscoelastic properties [9] [8]. The nano-manipulations are also applied to lift and push cells to measure adhesion forces among cells [128], adhesion forces between cell and substrate [126] [6] [131] [129], and intracellular electrical properties [5] as shown in Fig. 1.11(d) and Fig. 1.11(e). In Fig. 1.11(f), a nano-knife is used to perform a surgery on yeast cell [130]. Nano-manipulation can also contribute to the extraction of DNA from single-cell nucleus with a vision illustration from SEM. A nanospatula was used to dissect and collect a single-chromatin complex from cell nucleus, after the target location for extraction is decided by combining the information from both SEM images and fluorescence microscopy images [50] (Fig. 1.11(g)). Because the gene distributions in nucleus are not random, this work guarantee high-throughput gene mapping to explore the relation between gene loci and nuclear substructures [28]. Fig. 1.11(h) presents a self-reconfiguring microelectromechanical system (MEMS) nanoinjector for genetic modification of cells [15]. DNA is attracted to the outside of the lance using positive voltage, and then the lance is inserted into a cell. This lowers down cell internal stress caused by the extra fluid from traditional DNA microinjection.

1.4 Automation

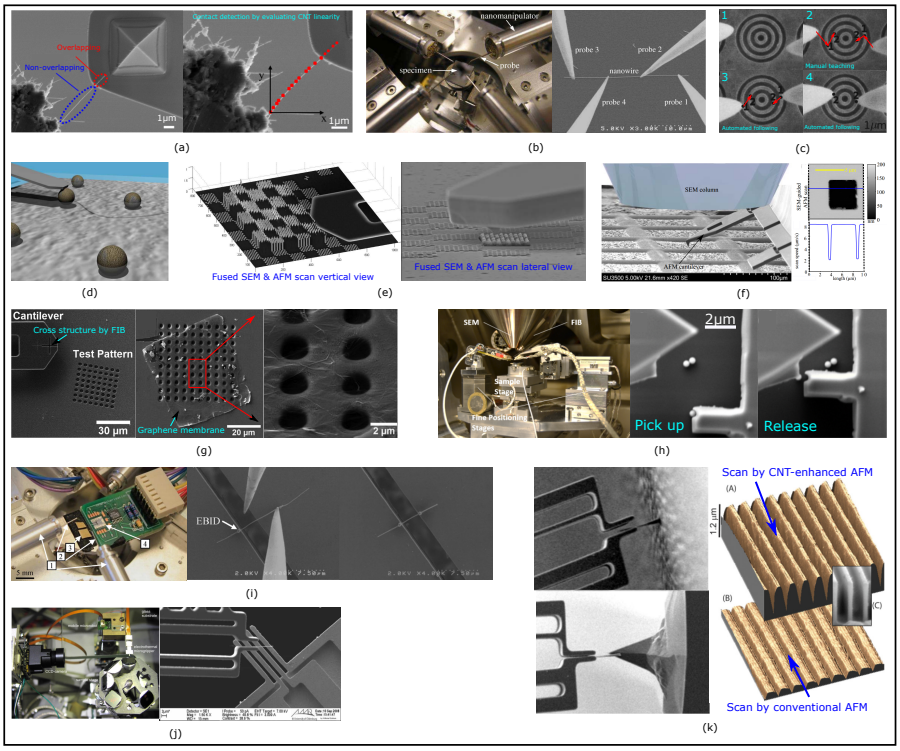

Figure 1.12: Automated nano-manipulation. (a) Automated CNTs pick-up based on SEM visual feedback. CNT and AFM cantilever during overlapping are separate by segment detection method (SDM) algorithm. Contact detection by evaluating CNT linearity [53] [133]. (b) Automated four-point probe measurement on a single nanowire. Adapted from [119]. (c) Automated nanoprobing for electrical characterization. Adapted from [49] [156]. (d) Robotic assisted micro-manipulation system for path plan by haptic/visual/sound interfaces [13]. (e) Fused representation of SEM overview scan and AFM topography scan of a calibration pattern [90]. (f) SEM-Guided AFM scan [29]. (g) Automated indentation for graphene membranes test [164]. (h) Individual colloidal spheres fully-automated pick-and-place by two coorporative nanoprobes with customized geometries [163]. (i) Automated nanowire pick-place on MEMS device for tensile test [149]. (j) CNT automated pick up, delivered to a microstructured four-point-probe for electrical measurements [38]. (k) CNT-enhanced, high-aspect-ratio AFM tip assembly [26].

To achieve an automated or semi-automated robotic task inside an electron microscope, it is necessary to used several sensor data (Fig. 1.6) including force measurements, SEM vision treatments as well as some tools such as virtual reality (VR) and tele-operation. Automated sequences can be made by specific tool boxes such as OFFIS Software developed in the Division Microrobotics and Control Engineering (AMiR) from University of Oldenburg.

To deal with unpredictable situations and to tend to less ad hoc solutions, two solutions are possible: including the human in the loop using teleoperation or developing advanced algorithms such as those based on machine learning. The first solution requires experienced operators, the second one is not well mature in the literature for SEM based nano-robotics.

Some examples of applications that have used automated or semi automated controllers are

illustrated in Fig. 1.12. The degree of automation can be categorized into three levels, low-automated, semi-automated and fully-automated. The low-automated level control is based on tele-operation, which requests experienced operators in the control loop to make decision according to comprehensive sensing cues, for instance, haptic and observations through SEM screen [20] [39]. The process is time-consuming and not repeatable when dealing with a batch of manufacturing production. The semi-automated level control plays an assistant role during the robotic task. Virtual Reality (VR) techniques can be used to get an access to a non-observable environment. VR can provide several informations such as vision, sound an touch to help the human operator to make a reasonable decision [13] [2]. In other applications, some tasks are partially feasible by an automated process while other ones are implemented manually [38]. To get an automation level, it is possible to first achieve a sequence based on a manually predefined procedure which is repeatedly executed after [149]. This is a manual teaching in order to provide reference operation sequence, followed by an automated duplication [133] [53] [156]. The fully automated level control is often achieved conditionally or task-oriented. Customized end-effectors can be used to guarantee a high manipulation success rate [163]. A summary of automation levels inside SEM is reported in Table 1.2.

1.5 Summery and objectives

According to the literature, SEM based nano-robotic systems are key tools for scientists and industrials that need to fabricate, observe and analyse products from micro and nano-technologies. Applications can be related to material science, electronics and mechanics at small scales as well as the fields of biology. The design of robotic systems made of materials compatible with the vacuum environment of SEM is well mature in the filed. The piezoelectric inertial actuator (PIA) is the most promising type of actuator for such robots as it can deal the the very high magnification capability of SEM by enabling motions in the centimeter range with a nanometer resolution. The works related in the literature have tackled very interesting critical issues of robotic at the small, but they have been made successfully thanks to the experience of the operator in the filed. There is still a huge gap between the nano-robotics technology inside SEM and its accessibility by *non-roboticists*. This thesis targets the development of a generic, intelligent and user friendly interface that can manage elementary robotic tasks needed inside a SEM by simply defining graphical instructions on the SEM screen. All these motion control must deal with *multi-scale trajectories*, i.e. trajectories in the nano-meter range up to the milliliter range. The high level control layer must consider decision making, motion planning, task assignments, according to the fusion of multiple sensing cues, varying from vision, position, velocity and force measurements. The low level control layer must be responsible of achieving the specific reference commands from the higher layer decision with a well mastered dynamic so that it can interact with the high level layer in real-time.

Table 1.2 –Summary of automation levels inside SEM

Task	Method	Automation level	Reference
Path planning assistance	Multi-mode tele-manipulation system with virtual reality environment using haptic/visual/sound combined with potentials fields interfaces	semi-automated	[13]
3-D Microassembly of microspheres	A dual-tip gripper controlled haptic interface for pick-and-place microspheres	low-automated	[20]
micromembrane stiffness cartography	Coarse approach by nano-manipulation system follows the behavior of its 3D replica in virtual reality interface controlled by operators. Fine approach by nanometric discrete position control.	semi-automated	[2]
CNTs griping for characterization	Two nanorobots coorperate for coarse and fine positioning for gripping CNTs. Contact detection are developed based on depth from focus of SEM imaging and touchdown sensor consist of bimorph piezo bending actuator.	low-automated	[39]
Pick-and-Place and characterization of CNTs	Utilize principle component analysis (PCA) for CNTs identification from SEM image, control the microgripper by CCD-based tracking, z-direction alignment by depth from focus and novel shadowbased depth detection technique, picks the CNTs automatically. Place the CNTs by tele-operation	semi-automated	[38]
Graphene membranes Young's modulus measurement	FIB milling on self-sensing AFM cantelever for SEM visual tracking and alignment for automated nano-indentation with discrete displacement control	fully-automated	[164]
Individual colloidal spheres pick-and-place	Two nanoprobes with tailored geometries cooperate, to grip, align and release the particle are based on the SEM vision servo and force control from a self sensing cantilever	fully-automated	[163]
Contact detection of SEM	coarse and fine positioning by nano-manipulators. Contact establishment inducing probe horizontal motion identified from SEM imaging.	full-automated	[118]
SEM-Guided AFM scan with dynamic speed	AFM scanning speed varying referring the velocity map drived from the features identified in SEM imaging	full-automated	[29]
Automated Four-Point Probing for nanowire electromechanical properties	Fine position over the nanowire by feedforward control referring SEM visual servo. Contact detection on nanowire by identifying the probe sliding monitored by SEM vision.	fully-automated	[153] [119]

Continued on Next Page...

Table 1.2 –Summary of automation levels inside SEM

Task	Method	Automation level	Reference
Automated Pick-Place of silicon nanowires	Low-pass Gaussian filter for sparse nanowire identification, edge detection and Hough line transform for substrate determination, contour extraction and corner detection for free end nanowire detection. Automated pick-and-place process is pre-defined and task depending. Contact detection by monitoring nanowire free end deflection.	semi-automated	[149]
Robotic Probing on SEM metrology chip	SEM imaging NL-Means denoising and drift compensation for real time tracking. Stick-slip coarse positioning and fine positioning ranged of tens of micrometers, by tubular nanopositioner, with radial bending motion and axial extension. Probing process defined by user teaching, followed with automatied duplication. Contact detection based on detecting the probe tip sliding motion.	fully-automated(manual teaching)	[49]
Integrated circuits (IC) quality inspection	Nanorobing on SEM metrology chip is carried out by fine positioning based on strain gauge sensing and open-loop coarse positioning. The probing process is teached manually and duplicate by aotomated manipulation. Automated contact detection is achieved by calibrating and establish a virtual coorinate system.	fully-automated	[156]
Automated Pick-up of CNTs from SEM	Histogram thresholding for automatic binarization, segment detection method (SDM) and linearity evaluation algorithms for CNTs recognization, overlap extraction and contatc detection. Pick-up CNTs with fixed step displacement control	fully-automated	[133] [53]

Chapter 2

Characterization, modeling and low level control of the ISIR-robotex nano-robotic platform

This chapter lays the foundations for the low level closed loop position and velocity control of the ISIR-robotex nano-robotic platform. This platform is composed of a multi-dof nano-robotic system actuated by Inertial Piezoelectric type Actuators (PIA) and holding an AFM cantilever as an end effector. The robotic system operates inside a SEM. Due to the very high magnification capability of Scanning Electron Microscopes (SEMs), to be able to reach any region of interest on a sample observed by an EM, the AFM probe must have the capability to navigate with a displacement range to resolution ratio of several million times which is referred as a multi-scale displacement. First, a non-linear model of PIAs is proposed to deal with multi-scale dynamic representation issues. It describes the mathematical relation between the input voltage applied to a piezoelectric element and the displacement of the associated slider. The model is based on a coupled piezo/friction hysteresis model and an augmented elasto-plastic friction model for which the breakaway displacement depends on the frequency and the amplitude of the input sawtooth voltage. This dependency is highlighted experimentally and represents the main novelty in friction modeling compared to the state of the art. Secondly, the nonlinear model is used to define control gains for two fundamental and elementary tasks inside the SEM, namely 3D motion generation of the AFM probe and multi-scale AFM tip landing on sample surface. Finally, velocity characterization and velocity control of a class of PIAs is studied. The achievable velocity range of PIAs is characterized in air and vacuum environments. This analysis allows the definition of a detailed map of the velocity characteristics in forward and backward motion directions. Velocity control strategies are then studied based on an instantaneous velocity feedback and an average velocity feedback. The low level controllers will be used in the next chapters as the basis to deal will multi-scale path following issues of AFM probes with SEM vision feedback.

2.1 ISIR-robotex nano-robotic platform

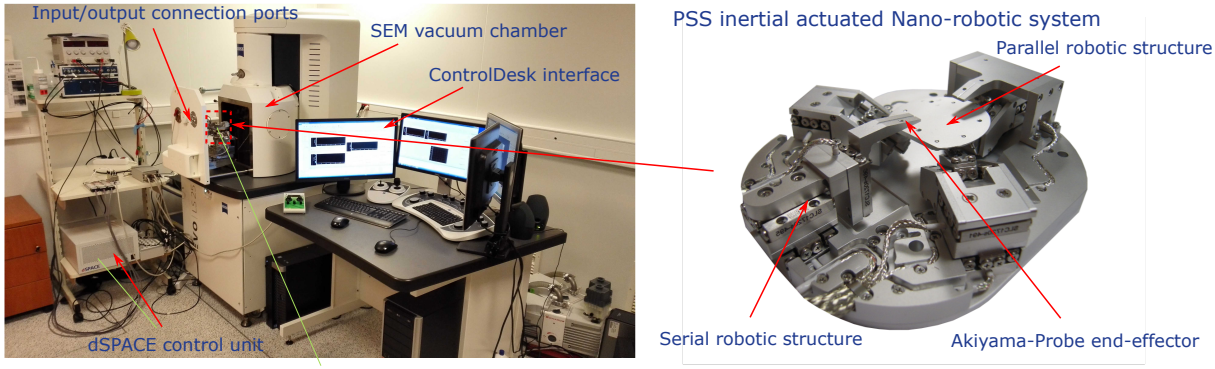

Figure 2.1: Experimental setup used in this study (a) and the nano-robotic system (b).

The ISIR-robotex nano-robotic platform is composed of (Fig. 2.1): **(i)** the multi-dof nano-robot actuated by 9 piezoelectric stick-slip actuators (SLC-1720), **(ii)** a controller board (dSPACE DS1007), **(iv)** a control interface (dSPACE ControlDesk), **(iii)** a Scanning Electron Microscope (ZEISS EVO LS 25) providing visual feedback and **(v)** a self seing tuning fork AFM probe as the end effector, with its signal processing unit interface.

2.1.1 SEM ZEISS EVO LS 25

The instruments EVO LS 25 is a high performance Scanning Electron Microscope (SEM) that includes a large analysis chamber to observe and analyze hydrated and non-hydrated samples.

The analysis chamber is under vacuum conditions so that the electron beam not only travels through the electron gun, but also within the chamber to reach the sample to be observed. The EVO LS 25 microscope allows various vacuum conditions, i.e various pressures. This extends the capabilities of the microscope to image and analyze non-conductive samples using a variable pressure mode. This is fundamental for samples or parts that cannot be coated with a thin conductive carbon or metal film. The variable pressure mode allows also the observation of hydrated and heavily contaminated samples (e.g. oily).

High vacuum (HV) mode: typically samples or parts are presented to the SEM with a conductive surface – native in the case of metals, or applied as a thin carbon or metal film on the surface of non-conductive samples. High vacuum delivers the best quality image and analysis data as the electron beam remains coherent when traveling in high vacuum through the column to the vacuum chamber.

Variable Pressure (VP) mode: when high quality imaging and analysis are needed on uncoated, non-conductive samples or parts, such as those being imaged in a multimodal workflow, VP mode is recommanded. VP mode uses a gas in the vacuum chamber to trigger a process of gas ionization that will neutralize charge build-up on the surfaces of non-conductive materials.

Extended Pressure (environmental mode): variable pressure also can be taken to the extreme, by choosing through-the-lens (TTL) pumping and water vapor in the specimen chamber,

to work at even higher gas pressures. This allows imaging at relative humidity up to 100% of hydrated samples in their natural state. This vacuum configuration is also recommended for heavily contaminated parts, where throughthe-lens pumping will prevent contamination from reaching the optical column.

Some examples of biological samples observed using the SEM of ISIR are shown in Fig. 2.2. The technical specifications are shown in Table 2.1:

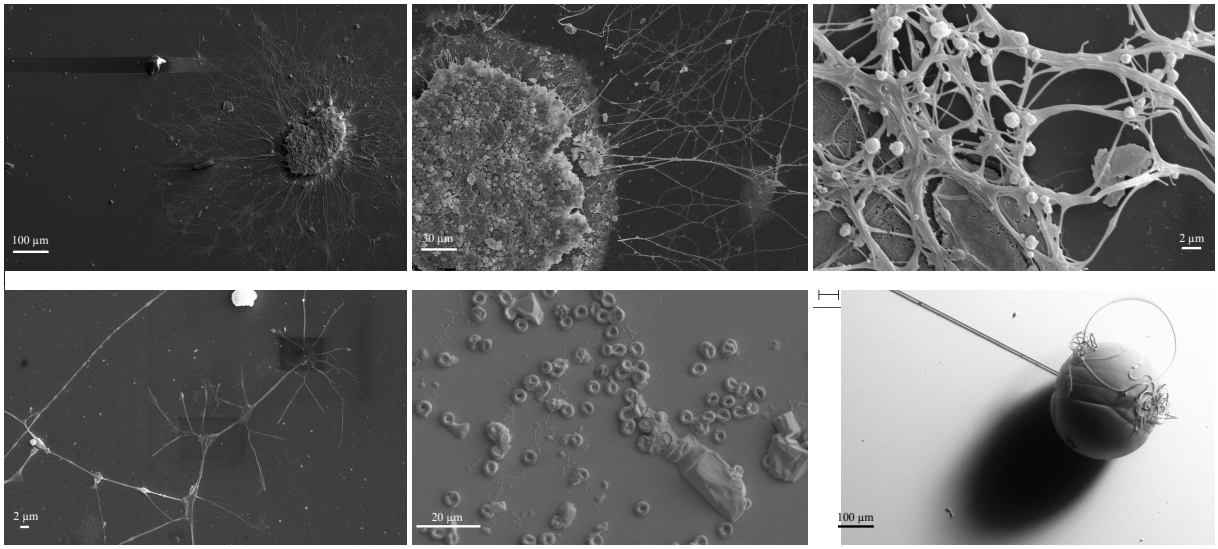

Figure 2.2: Some examples of biological samples observed using the SEM of ISIR.

In addition, there are 9 different scanning modes (Mode 1 - Mode 9) for EVO LS 25 microscopes. The electron beam scanning speed decreases with the scanning mode increase. Higher quality images can be obtained by lowering the electron scanning speed. This severely affects the performance of real-time close-loop control with visual feedback. Conversely, the higher the electron scanning speed is applied, the shorter time it takes to obtain the imaging, but at the price of a loss of the image quality resulting in noise and blur. In this work, Scanning Mode 3 is chosen for SEM visual feedback, to achieve a reasonable tradoff batween the image quality and scanning speed.

	Resolution	Acceleration Voltage	Probe Current	Magnification
Value	2 nm	0.2 to 30 kV	0.5 ρA to 5 μA	$< 5 - 1{,}000{,}000\times$

Table 2.1: SEM EVO LS 25 specifications.

2.1.2 Multi-dof nano-robot

The nano-robotic system is vacuum compatible. It is composed of a 3 DOF serial structure and a 6 DOF parallel structure (Fig. 2.1 b). All actuators of the nano-robot are piezoelectric stick-slip(PSS) with same reference (SLC-1720-S-HV). The actuators have a stroke of 12 mm and a resolution in the nanometer range. The position of each actuator is measured by an integrated

optical encoder with an initial resolution of 20 μm. To increase the measurement resolution, we have used a digital interpolator with an interpolation factor of 4096. As such, the measurement resolution is around 5 nm. The nano-robotic system is interfaced to a host computer via the controller board. X and Y axes of the serial structure are in the horizontal position while Z axis is in the vertical position (see Fig. 2.1 b). The end-effector, self sensing tuning fork AFM, is held by z axis actuator.

2.1.3 Controller board

The controller board is composed of a DS1007 PPC Processor Board, a DS2004 High-Speed A/D Board, and a DS3001 Incremental Encoder.

DS1007 PPC Processor Board: it provides high computing power combined with fast I/O access. The single-slot board offers an onboard Gigabit Ethernet host and I/O interface. It is an excellent fit application requiringe a combination of high computing power and fast closed-loop rates (e.g., for electric motor control, advanced driver assistance systems or active noise and vibration cancellation)

The DS1007 features a QorlQ P5020 dual-core processor running at 2 GHz. It is fully programmable from Simulink. It offers an integrated, high-data-throughput Ethernet host interface for setting up modular systems without additional host interface cards. The DS1007 is highly expandable. Its Ethernet I/O interface can be used for direct real-time model access via the TCP/IP or UDP/IP protocol and for bypassing.

DS1007 supports a multicore system by using the individual cores of the dual-core processor and easily assign the I/O boards by graphical programming via RTI-MP. The DS1007 dual-core board is able to speed up applications with parallel computing and high performance data exchange between the cores.

DS2004 High-Speed A/D Board: it has 16 channels with an independent A/D converter with a resolution of 16 bits and differential inputs. The conversion time is 800 ns per channel. Four external trigger lines, extensive trigger functions and onboard sample buffers enable single measurement as well as burst conversion. The board buffers up to 16,384 values per channel and then transfers them to the processor board as a burst. This reduces the communication overhead and improves the overall system performance.

The Real-Time Interface (RTI) libraries for the A/D board provide RTI blocks that allow you to implement the functionality and I/O capabilities of the board in Simulink models. The RTI blocks can be added to a Simulink model via drag & drop.

DS3001 Incremental Encoder: it comprises 5 parallel input channels, each providing everything needed to connect an incremental encoder and process its output signals: a regulated encoder power supply with sense lines, differential or single-ended inputs for the encoder's two phase lines, and an index input. Technical specification is given in Table 2.2.

	Channels	Position counter	Input frequency	Signal types	Resolution
Value	5	24 bit	1.25 MHz (max)	Digital	4-fold subdivision

Table 2.2: DS3001 technical specifications.

2.1.4 Akiyama AFM Probe (A probe)

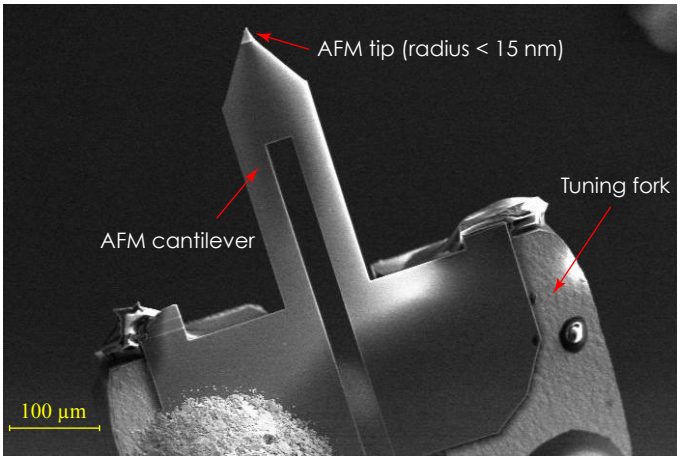

Figure 2.3: Akiyama A-probe Tunning Fork observed by the SEM of ISIR. It is composed of the AFM cantilever integrated on the tuning fork, [136].

Akiyama-Probe (A-Probe) is a self-sensing and self-actuating (-exciting) probe based on a quartz tuning fork (TF) combined with a micromachined cantilever for dynamic mode AFM. As shown in Fig. 2.3. Akiyama-Probe is equipped with a high-end sharp silicon tip (tip radius of $d \leq 15nm$, tip height of $28\mu m/s$) and has an excellent imaging capability on various samples with different properties. It requires neither optical detection, nor external shaker. Its compact and integrated structure of the cantilever is another advantage, making itself more adjustable for nano-manipulation within limited working space. A-Probe is designed for operation in ambient conditions. It may work in other conditions, like vacuum, UHV, or low temperatures.

Tipically, the A-Probe works at a dynamic mode with the frequency modulation (FM) detection, where the TF is self-excited (oscillating) at its first resonance frequency. This motion applies a small vibration at the glued ends of the cantilever, which always contains a component in z-direction (i.e., the axis of the tip) due to the twisting motion of the prongs (i.e., the cantilever disturbs a symmetry of the TF). The cantilever amplifies the vibration according to its mechanical property and a large out-ofplane motion of the tip is obtained. During sample imaging, the resonance frequency is tracked by a phase locked loop (PLL) and kept at a set value by adjusting the tip-sample distance with a feedback loop. The A probe can detect external forces applied on the AFM tip by a measurement of a shift on the resonance frequency of the tuning fork.

2.2 Nonlinear modeling and position motion control of an elementary pizoelectric inertial actuator

This section summarizes the work reported in [Boudaoud et al. Tmech 2018] dealing with the dynamic non linear modeling of PIAs embedded into the serial XYZ robotic structure. In this work, a particular case of PIAs are considered which are the Piezoelectric Stick Slip (PSS) actuators. However, the model can be generalized to a large class of PIA.

This model has been validated with experimental data for multi-scale displacements, i. from the mm range to the nm range:

- in both time and frequency domains,
- for the two operating modes of the nano-robot, i.e. scanning mode and stepping mode,
- for different motion directions, i.e. forward and backward,
- for close loop trajectory-tracking task.

The modeling is performed under the hypothesis that the actuator is composed of: (i) a Piezoelectric Element (PE) attached to the base of the actuator, (ii) a moving slider guided by a linear crossed roller guideway with one translational DOF and (iii) a friction material between the slider and the PE without lubricant (Fig. 2.4). The 3 DOF nano-robotic serial structure is modeled here. Let us consider X_e, Y_e and Z_e as the coordinates of the end effector. The direct geometric model of the structure is:

$$\begin{bmatrix} X_e \\ Y_e \\ Z_e \end{bmatrix} = \begin{bmatrix} q_x \\ q_y \\ q_z \end{bmatrix} + \begin{bmatrix} 0 \\ L_1 \\ -L_2 \end{bmatrix} \tag{2.1}$$

q_x, q_y and q_z are respectively the joint coordinates of X, Y and Z axis. The dimensions L_1 and L_2 are the initial position of the end effector in Y and Z axes respectively.

2.2.1 Multi-state dynamic modeling of the Piezoelectric Element (PE)

The PE of the studied PSS actuators series has two main vibration modes (Fig. 2.4), a multi-mode model is then used as follows:

$$M_p \frac{d^2 p_{z_a}}{dt^2} + D_{p_a} \frac{dp_{z_a}}{dt} + K_{p_a} p_{z_a} = K_{act_a} U - F_f \tag{2.2}$$

$$M_p \frac{d^2 p_{z_b}}{dt^2} + D_{p_b} \frac{dp_{z_b}}{dt} + K_{p_b} p_{z_b} = K_{act_b} U - F_f \tag{2.3}$$

$$p_z = p_{z_a} + p_{z_b} \tag{2.4}$$

M_p, D_{p_i}, K_{p_i} and K_{act_i} are respectively the mass, the damping, the stiffness and a static gain of the first vibration mode and the second vibration mode (when replacing i with a and b

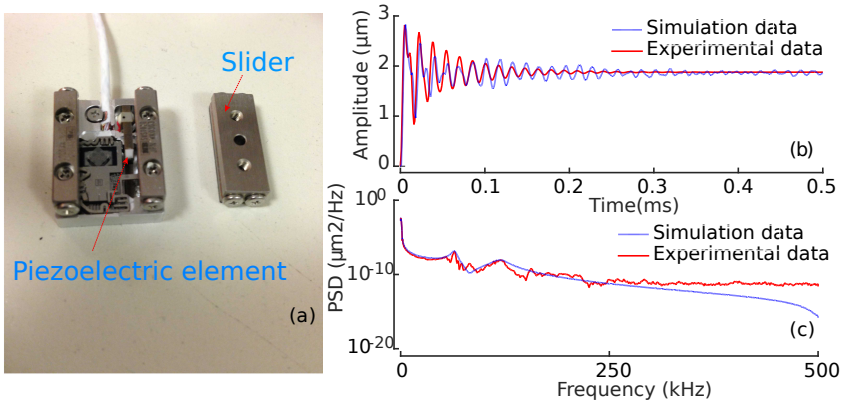

Figure 2.4: Step response and Power Spectral Density (PSD) of the x axis PE (PSS actuator without slider) using a 90 V step input. Two main vibration modes at 64 kHz and 118 kHz.

respectively). p_{z_i} is the displacement of a vibration mode i. The total displacement of the PE is p_z. U and F_f are respectively the input voltage and the friction force between the slider and the PE.

In static mode (i.e when t$\rightarrow \infty$), the hysteresis nonlinearity $H(.)$ is considered. The Modified Prandtl-Ishlinskii (MPI) static hysteresis model is used to define $H(.)$. It is well adapted for non-symmetric hysteresis. This model is composed of (see equation 2.5): (i) n blocks of backlash $\beta\left(r_{b_i}\right)$ with a bandwidth $2 \times r_{b_i}$ and a weighting coefficient ω_{b_i} for each block and (ii) n blocks of dead zone $\Delta\left(r_{dz_i}\right)$ with a dead zone width $2 \times r_{dz_i}$ and a weighting coefficient ω_{dz_i} for each block $(1 < i < n)$.

$$H\left(.\right) = \left[\sum_{i=1}^{n} \omega_{dz_i} \Delta\left(r_{dz_i}\right) \sum_{i=1}^{n} \omega_{b_i} \beta\left(r_{b_i}\right)\right] \tag{2.5}$$

2.2.2 Dynamic Modeling of the the Slider

The motion q of the slider is produced thanks to the friction force F_f. The dynamic equation of the slider can be described by the following equation:

$$M_s \frac{d^2 q}{dt^2} = F_f \tag{2.6}$$

M_s is the mass of the slider. In the sequel, the friction force is modeled by an augmented elasto-plastic model whose original formulation has been proposed in [36].

2.2.3 Modeling of the friction force

For the PSS actuators of the X, Y and Z axes, experiments have shown that in the stepping operating mode, the breakaway displacement z_{ba} depends on the amplitude and the frequency of the input sawtooth signal. This dependency is different when the slider is moving in a forward direction or in a backward direction. Therefore, we propose here an augmented formulation

of the original elasto-plastic model by taking into account a voltage/frequency rate dependent function of z_{ba}. Moreover, experiments have shown that the actuator has several low frequency (< 15 kHz) vibration modes which are not due to the PE. According to our hypothesis, the low frequency vibration modes are related to the presliding motion between the PE and the slider. A multi-state elasto-plastic friction model is then formulated to describe F_f

2.2.3.1 Multi-State Elasto-Plastic Friction model

In the elasto-plastic friction model, the motion $x = p_z - q$ between the PE and the slider is decomposed into elastic and plastic parts, denoted by z and w respectively:

$$x = z + w \tag{2.7}$$

Let us consider an external force that produces the motion x, which can be elastic (case 1), elasto-plastic (case 2), or purely plastic (case 3). If the external force is cancelled, in case 1, the motion x returns back to its initial position, in case 2, the motion return back with an offset due to the plastic part, and in case 3, the motion is irreversible due to the pure plastic motion. In the elastic range (case 1) $\dot{x} = \dot{z}$ and $\dot{w} = 0$. In the elasto-plastic range (case 2) $\dot{x} = \dot{z} + \dot{w}$. In the pure plastic range (case 3) $\dot{x} = \dot{w}$ and $\dot{z} = 0$. Each motion range is delimited by the breakaway displacement z_{ba} and the steady-state elastic strain z_{ss}. The motion x is in the elastic range (case 1) when $|z| \leq z_{ba}$. When $z_{ba} < |z| < |z_{ss}|$, mixed elastic and plastic displacements are produced (case 2). Otherwise, only plastic displacement or sliding occurs (case 3), with $|z|$ saturates to $|z_{ss}|$.

A single-state elasto-plastic friction model with the friction force F_f is governed by:

$$F_f = \rho_0 z + \rho_1 \dot{z} + \rho_2 \dot{x} \tag{2.8}$$

ρ_0, ρ_1 and ρ_2 are respectively the contact stiffness, the damping for the tangential compliance and the viscous friction constant. When the friction is presliding dominant with a small velocity $\dot{x}$, $\rho_2 \dot{x}$ is negligible compared to dry friction [67].

As such, the force F_f has a stiffness component ρ_0 and a damping component ρ_1. Each of these parameters, including the mass of the moving surface, can define a resonance mode.

The elastic component z is described by the equation:

$$\dot{z} = \dot{x}\left[1 - \alpha(z, \dot{x})\frac{z}{z_{ss}}\right] \tag{2.9}$$

where α is given in equations (2.10) and (2.11), [36].

$$\alpha\,(.) = \frac{1}{2} Sin\left(\pi \frac{|z| - \frac{|z_{ss}|+z_{ba}}{2}}{|z_{ss}| - z_{ba}}\right) + \frac{1}{2} \tag{2.10}$$

$$\alpha\left(z,\dot{x}\right)=\left\{\begin{array}{ccc}0 & |z|\leqslant z_{ba} & \\ \alpha(.) & z_{ba}<|z|<|z_{ss}| & \left.\begin{array}{l}\\ \\ \\ \end{array}\right\} \quad \operatorname{sgn}(\dot{x})=\operatorname{sgn}(z) \\ 1 & |z|=|z_{ss}| & \\ & 0 & \operatorname{sgn}(\dot{x})\neq\operatorname{sgn}(z)\end{array}\right. \tag{2.11}$$

Equations (2.7), (2.9), (2.10) and (2.11) allow satisfying the requirements on $\dot{x}(t)$, $\dot{w}(t)$ and $\dot{z}(t)$ in case 1, case 2 and case 3 as described above.

z_{ss} is often assigned in the literature as a positive constant independent of $\dot{x}(t)$. In order to ensure that the model is able to simulate the motion of the slider in both forward and backward directions, we replace z_{ss} by $z_{ss}(z)$ and we propose the following formulation [85]:

$$z_{ss}(z)=z_{ss}\ \operatorname{sgn}(z) \tag{2.12}$$

z_{ss} in the right side of equation (2.12) only represents a positive constant value. Combined with the condition that $|z|$ is always saturated to $|z_{ss}|$, for any motion direction it yields:

$$0\leqslant\frac{z}{z_{ss}(z)}\leqslant 1 \tag{2.13}$$

Taking into account the equations (2.9), (2.10) and (2.11), the condition $0\leqslant dz/dx\leqslant 1$ is always satisfied. This condition is necessary as described in the original paper [36], when super relaxation is produced and no Stribeck effect is considered.

Let us now consider a multi-state elasto-plastic model. In this case F_f is governed by the following equation:

$$F_f=\sum_{i=1}^{m}\left(\rho_{0_i}z_i+\rho_{1_i}\dot{z}_i\right) \tag{2.14}$$

Here, we select m=3 to take into accound 3 eigenmodes in the friction presliding dynamic. This choice is motivated by the experimental curves of Fig. 2.5.

This formulation will allow to describe m resonant frequencies of the stick-slip actuator. The resonant frequency f_{r_i} for an eigenmode i is:

$$f_{r_i}=\frac{1}{2\pi}\sqrt{\frac{\rho_{0_i}}{M_s}}. \tag{2.15}$$

The complete model of the PSS actuator describes the nonlinear transfer between the motion q and the voltage U.

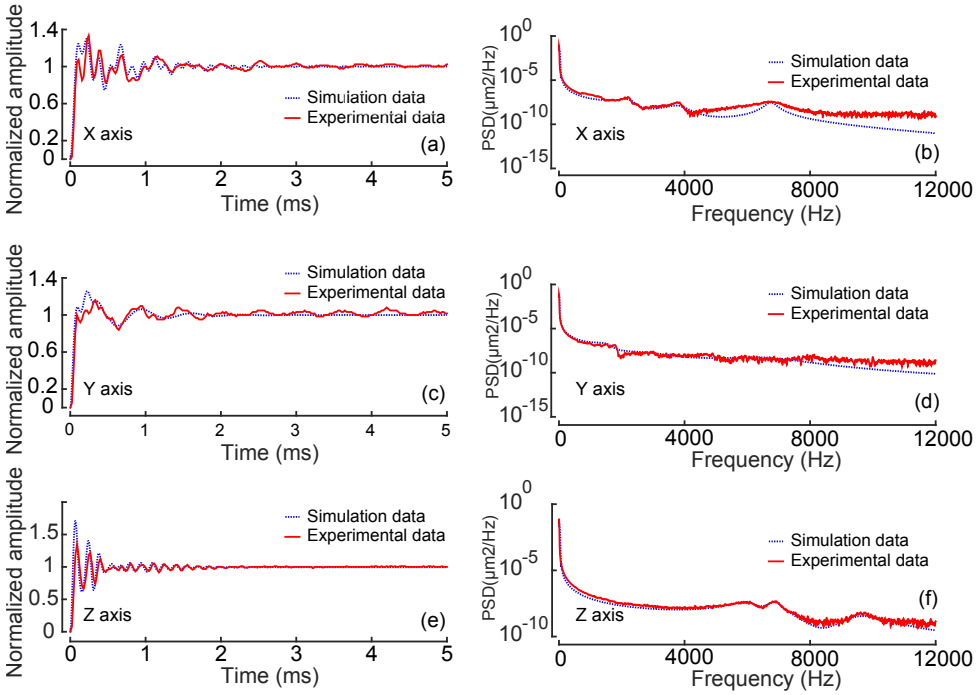

Figure 2.5: Step response of the PE (PSS actuator without slider) using a 90 V step input (a). PSD of the PE (PSS actuator without slider) using a 90 V step input (b). Normalized (to unity) step response of X axis (c), Y axis (e) and Z axis (g) for a 30 V step input voltage (PSS actuator with slider). PSD of the step response of X axis (d), Y axis (f) and Z axis (h). The PSD of each measured step response (c), (e) and (g) shows three main vibration modes. For X axis: 2200 Hz, 3700 Hz and 6800 Hz. For Y axis: 1500 Hz, 2900 Hz and 8000 Hz. For Z axis: 5950 Hz, 6850 Hz and 9630 Hz.

2.3 Experimental analysis and parameters identification

The dynamic parameters of the PE in equations (2.2) and (2.3), the hysteresis parameters in equation (2.5) and the friction force parameters of equations 2.7-2.12, are identified [85] [22]. The breakaway displacement z_{ba} is fitted to cover the ranges [50 Hz - 1 kHz] and [20 V - 95 V] in both motion directions.

The model identification is done considering experimental data from each axis of the serial structure (i.e. X, Y and Z axis) independently. Experiments are performed in air. The identification results are presented in TABLE 2.3.

Simulation and experimental data demonstrate highly consistency as shown in Fig. 2.5 and Fig. 2.6.

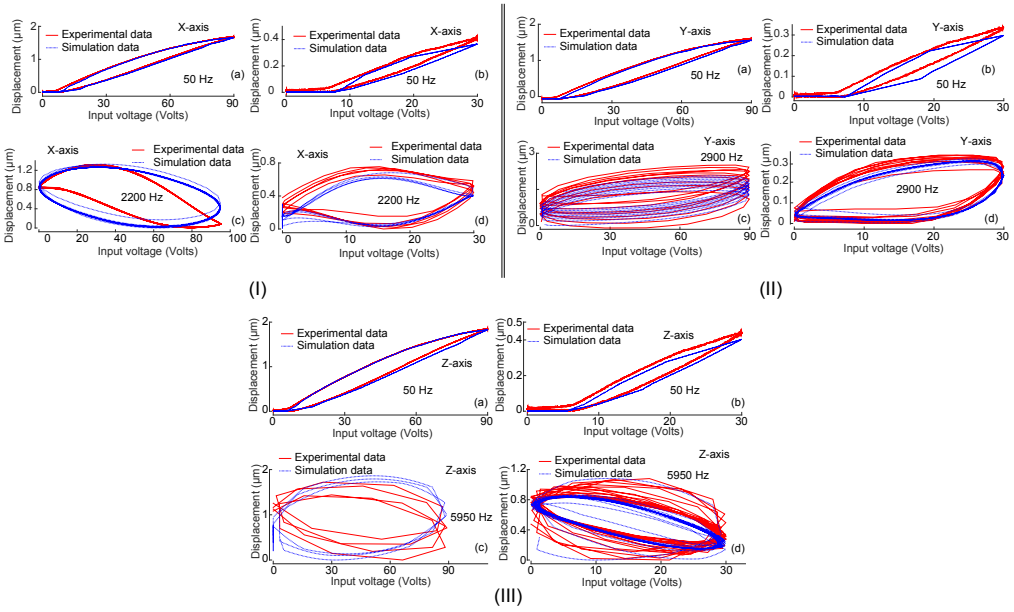

Figure 2.6: Hysteresis curves of X axis (I), Y axis (II) and Z axis (III). The amplitude and the frequency of the input sin signals are: (I-a) 90 V, 50 Hz, (I-b) 30 V, 50 Hz, (I-c) 90 V, 2200Hz,(I-d) 30V,2200Hz, (II-a) 90 V, 50 Hz, (II-b) 30 V, 50 Hz, (II-c) 90 V, 2900 Hz, (II-d) 30 V, 2900 Hz, (III-a) 90 V, 50 Hz, (III-b) 30 V, 50 Hz, (III-c) 90 V, 5950 Hz, (III-d) 30 V, 5950 Hz.

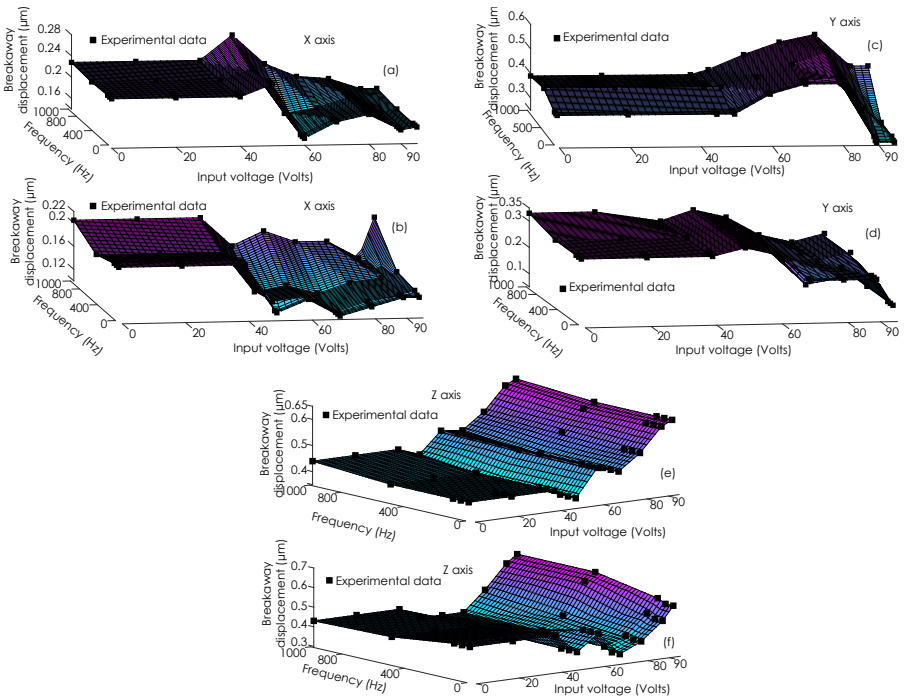

Figure 2.7: Voltage/frequency rate dependent characteristic of the breakaway displacement z_{ba}. Characteristic for the forward direction of motion: (a) X axis, (c) Y axis and (e) Z axis. Characteristic for the backward direction of motion: (b) X axis, (d) Y axis and (f) Z axis. The curves are obtained with experimental data in the ranges [20 V - 95 V] and [50 Hz - 1 kHz]

For the identification of z_{ba}, different sawtooth voltages are applied to measure the displacement q of the slider. The average slope of q is calculated for the identification of z_{ba} considering $r_z = \frac{z_{ss}}{z_{ba}} = 1.1$. For each nano-robot axis, 32 sawtooth voltages are applied in forward direction and 32 in backward direction. The frequencies of the input signals are 50 Hz, 100 Hz, 500 Hz and 1kHz. For each frequency, different amplitudes are used, namely 20, 40, 50, 60, 70, 80, 90 and 95 V. Identified results of z_{ba} are fitted to cover the ranges [50 Hz - 1 kHz] and [20 V - 95 V]. Results are shown in Fig. 2.7. These characteristics are quite different for the actuators of the 3 axes even they are from the same reference.

Nevertheless, common properties can be observed:

(i) For two sawtooth signals of same amplitude and same frequency, the characteristics of z_{ba} are different in backward and in forward directions of motion (see for instance Fig. 2.7 (a) and Fig. 2.7 (b)). This can explain the asymmetric behavior of the actuator in the two motion directions.

(ii) The breakaway displacement is more sensitive to the amplitude of the input signal than to its frequency. This is important for simulation issues. The model can be simplified by considering only the relation between z_{ba} and U.

For control issues, these results show that the model and/or an observer based on the model must be designed considering a relation between z_{ba} and U for each driving direction.

X, Y and Z axes parameters [unit]		Identified values		
		X axis	Y axis	Z axis
ρ_{0_1}	$[N/m]$	4.012×10^6	9.67×10^5	3.15×10^6
ρ_{0_2}	$[N/m]$	1.27×10^7	3.52×10^6	4.14×10^6
ρ_{0_3}	$[N/m]$	4.93×10^7	2.08×10^7	8.35×10^6
ρ_{1_1}	$[Ns/m]$	78.77	39.07	17.72
ρ_{1_2}	$[Ns/m]$	137.24	154.4	13.99
ρ_{1_3}	$[Ns/m]$	96.03	246.94	32.92
PE parameters [unit]		Identified values		
M_p	$[Kg]$	0.00075		
D_{p_a}	$[Ns/\mu m]$	25.86		
D_{p_b}	$[Ns/\mu m]$	82.17		
K_{p_a}	$[N/\mu m]$	1.23×10^8		
K_{p_b}	$[N/\mu m]$	4.24×10^8		

Table 2.3: Identified parameters of the PSS actuator for X, Y and Z axis.

2.4 Closed loop trajectory generation and control strategies

The nonlinear model is used to define control strategies for the 3 DOF structure. The aim is to analyze if a motion generation defined by simulation with a controller can be faithfully reproduced when the same controller is implemented experimentally. The first part deals with a closed loop trajectory generation involving X and Y axes in stepping mode only. The second part

deals with a contact detection strategy with Z axis in a mixed regime: stepping and scanning.

2.4.1 Closed loop trajectory generation in stepping mode

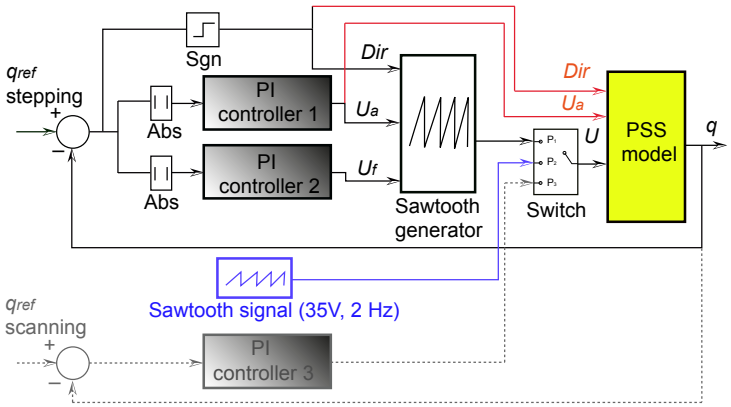

Figure 2.8: Control diagram of one axis of the nano-robotic system. q_{ref} stepping is the reference position in stepping mode. q_{ref} scanning is the reference position in scanning mode. The switch block define which control signal is used: position P_1 for closed loop stepping control, position P_2 for open-loop stepping control and position P_3 for closed loop scanning control.

In stepping mode, the closed loop control scheme for one axis of the nanorobot is shown in Fig.2.8 where the switch is always in position P_1. It includes:

(i) A sawtooth generator designed with matlab/Simulink. This generator has three inputs U_A, U_F and Dir to control respectively, the amplitude, the frequency and the direction of the sawtooth output signal U at each sampling time.

(ii) The PSS model defined in the previous sections with the identified parameters. The inputs of the model are the voltage U, the input direction Dir and the signal U_A. Dir and U_A are used to define the value of z_{ba} at each sampling time.

(iii) PI controller 1. It is a Proportional Integral (PI) controller used to control the amplitude of the sawtooth signal U taking into account the absolute value of the error between the reference position q_{ref} in stepping mode, the actual position q (i.e. $\left|q_{ref_{stepping}} - q\right|$) and the absolute value of the integral of this error. The proportional gain and the integral gain are denoted respectively $K_{p_{V\_step}}$ and $K_{i_{V\_step}}$.

(iv) PI controller 2. It is also a PI controller used to control the frequency of the sawtooth signal U. The input of this controller is the same as that of PI controller 1. The proportional gain and the integral gain are denoted respectively $K_{p_{F\_step}}$ and $K_{i_{F\_step}}$.

Let us denote $q_{ref}X$ and $q_{ref}Y$ the reference positions in stepping mode for X and Y axes respectively.

$$\begin{cases} \mathbf{q_{ref}}X = (-20t + 1000)\sin(2\pi f_0 t + \frac{\pi}{2}), \\ \mathbf{q_{ref}}Y = (-20t + 1000)\sin 2\pi f_0 t, \end{cases} \tag{2.16}$$

t is the time vector.

The controller of Fig.2.8, where the switch is always in position P_1, has been applied for X and Y axes. First, the controller has been simulated with Matlab/Simulink using the nonlinear model of the nano-robotic system. Secondly, the controller with the same parameters (i.e. controller's gains) has been implemented in real time on the dSPACE controller board.

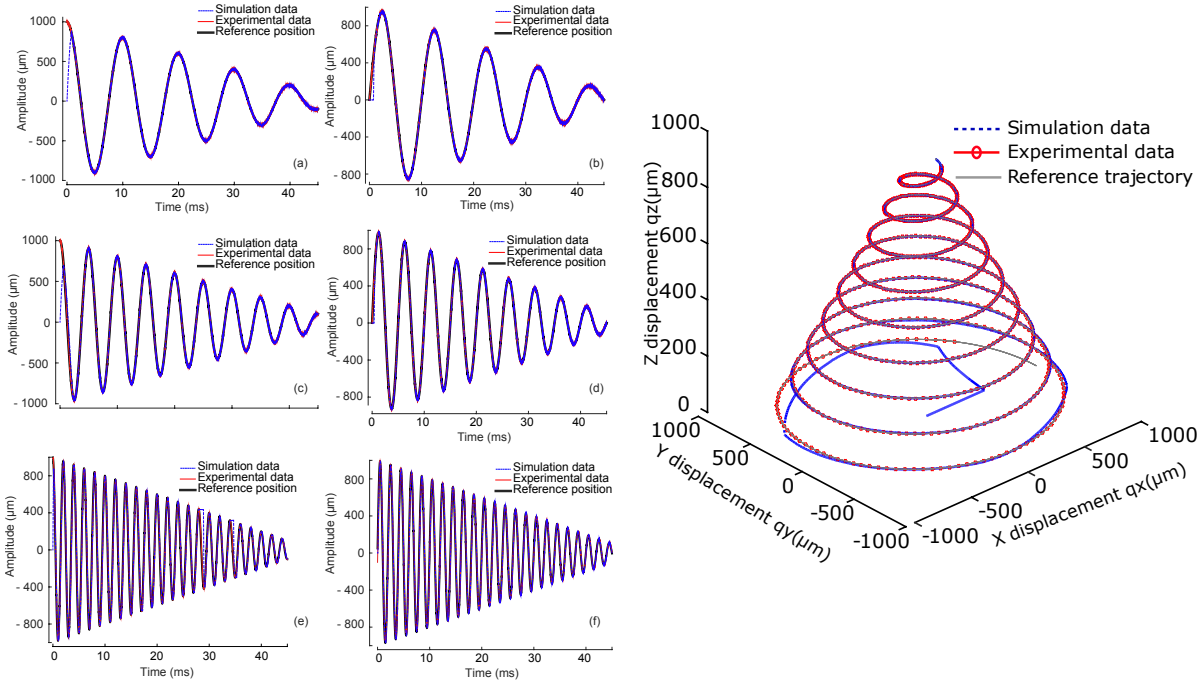

Figure 2.9: Closed loop displacements of the X axis and Y axis in response to a decreasing amplitude reference input $q_{ref}X$ and $q_{ref}Y$ respectively. Reference trajectory, experimental data and simulation data are shown. Experiments are done in air. X axis: (a) 0.1 Hz, (c) 0.2 Hz and (e) 0.5 Hz. Y axis: (b) 0.1 Hz, (d) 0.2 Hz and (f) 0.5 Hz. The same controller's parameters have been used in simulation and for experiments. (g) Results of the 3D spiral motion in XYZ

Results in Fig.2.9 show that, both in simulation and experiments, the 3 DOF structure of the nano-robot tracks well the reference trajectories for frequencies 0.1 Hz, 0.2 Hz and 0.5 Hz, in stepping mode. This consistent result demonstrates the efficiency of the model to design a controller by simulation upstream of a real time implementation. Indeed, the gains of the controller have been defined by simulation using the model and the same gains have been implemented experimentally. In the next section, the study goes further by generating a motion as well in the millimeter range as in the nanometer range, which covers a motion range where the maximum displacement is one million times higher than the minimum one.

2.4.2 Multi-scale AFM tip landing inside SEM

We propose here a mixed stepping/scanning control to land the AFM cantilever in a wide motion range. The control strategy of Fig. 2.8 is also used here, where the switch can be in positions P_1, P_2 or P_3 depending on specific conditions. For a safe contact detection, the PSS actuator

must operate in both scanning and stepping modes.

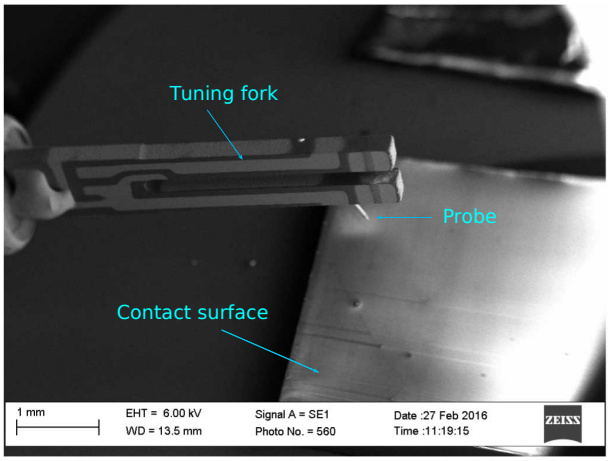

Figure 2.10: A tuning-forkbased dynamic force sensor on Z axis. A tungsten probe tip of 1-2 mm length with a tip radius around 1 μm, manually glued on the side of one prong of the tuning fork, oscillating at resonance frequency of 32 kHz. Resonance frequency shifts and feedback as voltage V_{sh}, when contact occurs between probe and environment.

The tuning fork oscillates at is resonance frequency (32 kHz). When the probe tip touches a sample, a shift of frequency occurs. This shift is deduced from an analog voltage V_{sh}. See [1] for more details about the working principle of the tuning fork probe.

The control strategy is applied on Z axis of the nano-robot serial structure. It has been defined as follows (Fig. 2.8) :

Step1 - *stepping mode control- (Switch position P1)*: the actuator is controlled in stepping mode with a course reference position equal to 1 mm, through controller in Fig.2.8.

Step 2 - *mixed stepping and scanning mode control- (Switch position P2 or P3)* : the actuator is controlled in a mixed regime scanning mode (Switch position P3) and stepping mode (Switch position P2). For the scanning mode, the voltage U is generated by the PI controller 3. The reference position is 1.7 μm. For the stepping mode, the amplitude and the frequency of the sawtooth signal are fixed to 35 V and 2 Hz respectively (open loop). In this step, the Z axis performs a fine approach of the probe tip toward the sample. The scanning mode control monitoring contact signal V_{sh}, ensures a safe approach of the probe toward the sample. The amplitude of the displacement in stepping mode must be lower than that in scanning mode. As such, it is ensured that the probe touches the sample only in the phase of scanning control.

Step 3 - *scanning mode control- (Switch position P3)*: the voltage V_{sh} of the tuning fork probe detects a contact. Only the PI controller 3 is then active. The probe returns back in closed loop by 100 nm in scanning mode, Fig. 2.11 (c).

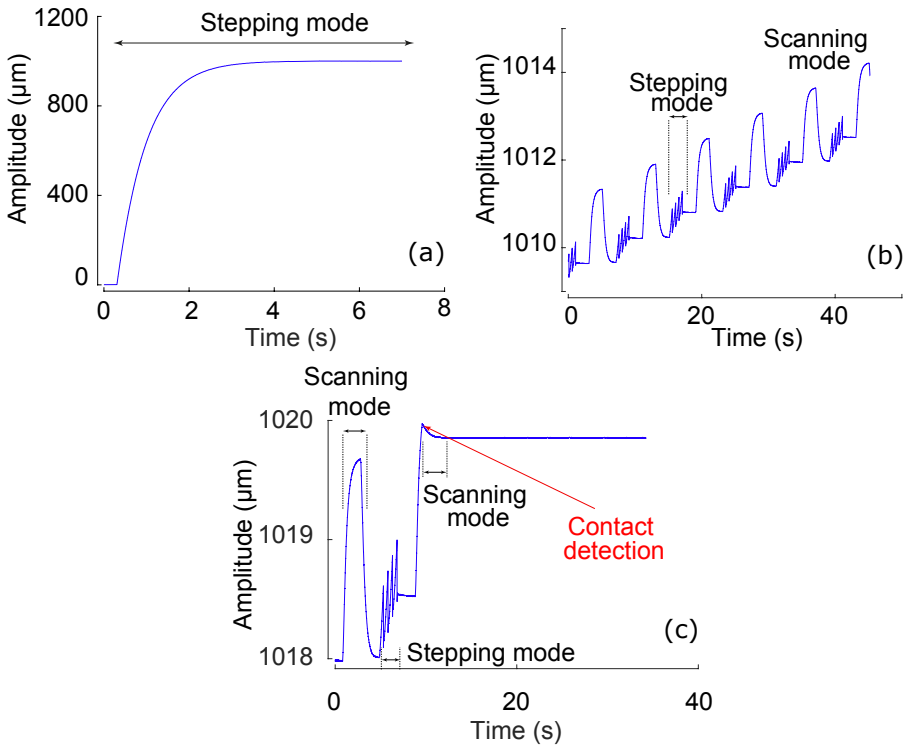

Figure 2.11: Experimental results of the controlled position of Z axis by the controller in Step 1 (a), Step 2 (b) and Step 3 (c). When the position of Z axis increases, it is moving toward the sample.

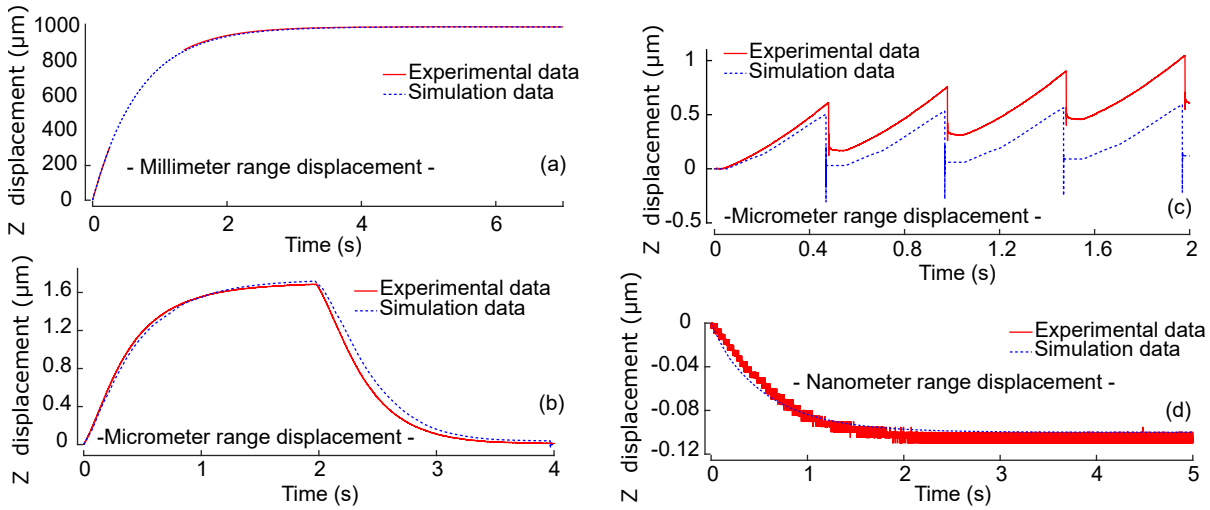

Figure 2.12: Experimental and simulation results of the controlled Z axis position in Step 1 (a), Step 2 (b) (c) and Step 3 (d). The time origin is set at 0.

The control strategy including the 3 steps has been simulated with Matlab/Simulink using the nonlinear model of the Z axis. The control strategy with the same parameters (i.e. gains of the controllers in Steps 1, 2 and 3) has been implemented in real time on dSPACE controller

board. The nano-robotic system is operating in the vacuum chamber of the SEM. Fig. 2.11 (a),(b),(c) show respectively the experimental results of the controlled position of Z axis in Step 1, Step 2 and Step 3. The switch from Step 2 to Step 3 is performed when the value of V_{sh} is higher or lower than two threshold values.

The experimental closed loop position of Z axis is very close to that obtained by simulation during Step 1, Step 2 and Step 3. This result demonstrates that the control parameters (controllers gain) can be completely defined by simulation when considering millimeter (Fig. 2.12 (a)), micrometer (Fig. 2.12 (b)) and even nanometer displacements (Fig. 2.12 (d)). The mean errors between experimental data and simulations are 0.56 %, 18.36% and 8.25% for closed loop millimeter, micrometer and nanometer displacements respectively. The efficiency of the model to design a controller by simulation in stepping mode, in scanning mode and in a mixed mode upstream of a real time implementation is demonstrated. Therefore, the proposed model can be used for observer and control designs as well as simulation and code generation for nano- robotics through a streamlined CAD/CAM engine programming.

2.5 Velocity characterization and control

In the previous sections, we have developed the control the PSS actuated nano-robotic system through position control. However, if we want to achieve more automated tasks, such as driving the end-effector to accurately follow a reference trajectory and path, velocity control is of primary importance. The work of this section fills the technological gap in nano-robotics for applications requiring a motion generation and path following at the micrometer and the nanometer scales with a controlled speed. In order to provide velocity references that PSS actuators can achieve, experiments are carried in both forward and backward directions of motion under air and vacuum environments. Through applying various input sawtooth voltages on the actuator with different amplitudes and frequencies, the velocity range of the actuator is identified. This analysis allows obtaining a detailed map of the velocity characteristics. Velocity control strategies are then studied and implemented experimentally on the nano-robotic system. The control method is based on a Proportional Integral (PI) scheme to control the amplitude and the frequency of a sawtooth input voltage with a velocity feedback of the actuator. Two control strategies are studied, the first one uses the instantaneous velocity of the actuator as a feedback signal and the second one uses, at each sampling time, the slope value of the displacement from the actuator's starting position as the closed loop feedback.

2.5.1 Analysis and characterization of the velocity

Because the nano-robotic systems is not only used in air environment but also in the vacuum chamber of the SEM, the velocity characterization is done in both air and vacuum. Without loss of generality, all experiments are performed on the PSS actuator of Y axis in the serial nano-robotic structure (see Fig. 2.1).

The aim is to define the reachable velocities of the actuator based on the experimental conditions. Experiments have shown that the velocity of the slider depends mainly on the sawtooth voltage parameters, namely the amplitude, the frequency and the sign of the ramp slope.

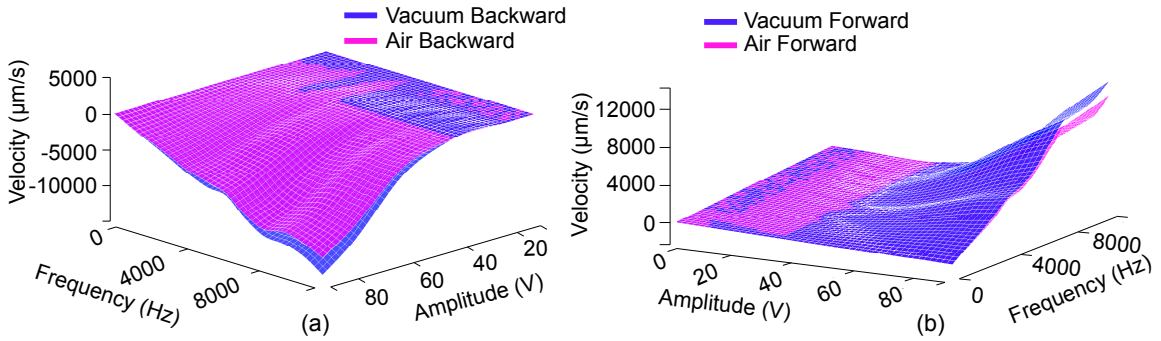

Figure 2.14: Velocity characteristics of the PSS actuator in air and vacuum environments for backward (a) and forward (b) motion directions.

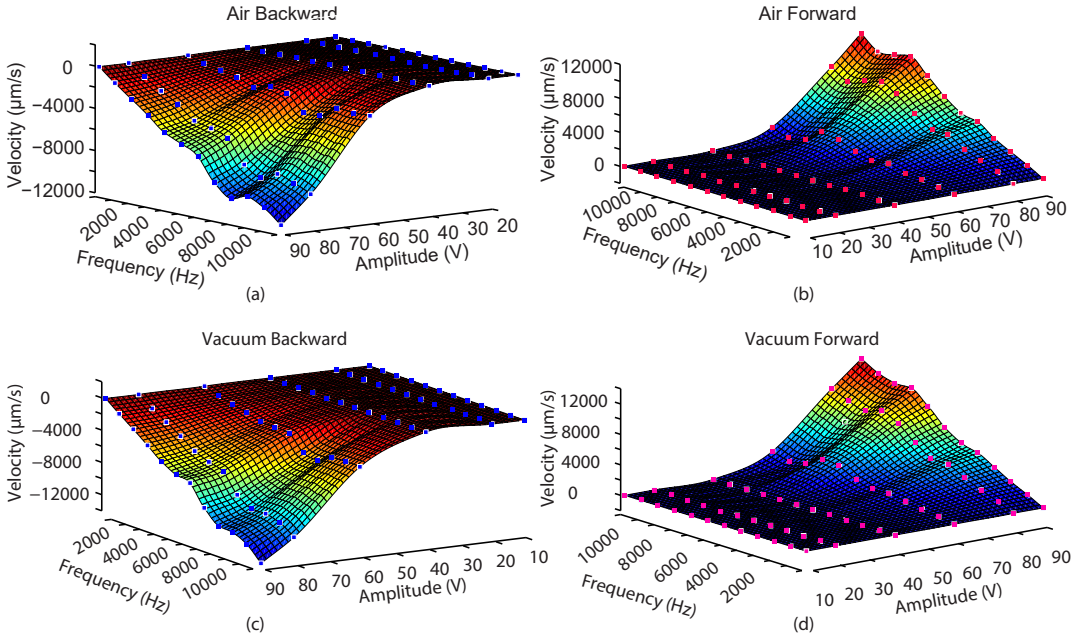

Figure 2.13: Velocity characteristics of the piezoelectric stick-slip actuator in vacuum environment.

The experiments have been done first in air and then in vacuum under the following protocol: (i) a sawtooth voltage with a fixed amplitude, frequency and ramp slope is applied on the piezoelectric element of the actuator, (ii) the displacement of the slider is measured during several seconds with 35 kHz sampling frequency using the integrated optical encoder, (iii) the average velocity is calculated based on the experimental displacement measurement. This experiment is repeated for sawtooth voltages with the following frequencies: 50 Hz, 1 kHz, 2 kHz, 3 kHz, 4 kHz, 5 kHz, 6 kHz, 7 kHz, 8 kHz, 9 kHz, 10 kHz and 11 kHz. For each frequency, different amplitudes have been are applied, namely 10 V, 20 V, 40 V, 60 V, 80 V and 90 V. The same experiment is then repeated by changing the sign of the ramp slope of the sawtooth voltage. In total, the average velocity of the actuator has been identified for 144 operating points in air and 144 operating points in vacuum. In this latter case, the nano-robotic system has been put inside the SEM with a vacuum pressure of 3.16×10^{-4} Pa.

	Air		Vacuum	
	Forward	Backward	Forward	Backward
Maximum Velocity [μm/s]	10732	-11465	12313	-13796
Minimum Velocity [μm/s]	17	-30.9203	21.9235	-37.473

Table 2.4: Maximum and minimum measured velocities in different operating conditions.

For each operating condition, i.e. air/forward direction, vacuum/forward direction, air/backward direction and vacuum/backward direction, the velocity characteristic of the actuator with respect to the amplitude and the frequency of the sawtooth voltage has been obtained (Fig. 2.13) by fitting the experimentally identified average velocities with a cubic interpolation.

For a given set of amplitude and frequency, the slider moves faster in backward direction. This is observed in both air and vacuum conditions. The velocity does not depend on the sawtooth voltage parameters only, but also on the working environment. Indeed, with the same input amplitude, input frequency and motion direction, the actuator moves faster in vacuum than in air as shown in Fig. 2.14. The difference of velocity in air and vacuum is significant only for velocities higher than 10000 μm/s. The minimum and the maximum identified velocities for each operating condition are summarized in Table 2.4.

For control purposes, the velocity characteristic curves allow the definition of the required amplitude and the required frequency of the sawtooth voltage to reach a desired velocity. It can also be used as a basis for the definition of the proportional gains to control the amplitude and the frequency of the sawtooth voltage in closed loop so that the actuator can reach a reference velocity. In addition, as it will be shown in Chapter 4, the velocity maps can be used as an internal model for model predictive control.

2.5.2 Velocity control strategies

Velocity control strategies are proposed in this section considering the range [500 μm/s - 5000 μm/s]. As shown in Fig. 2.14, the effect of the environment (i.e. air and vacuum) on the velocity in this range is not very high. As such, velocity control in both environments using the same controller will lead to comparable results. Therefore, in this section experiments are performed in vacuum only.

The first strategy is based on the instantaneous velocity while the second one uses the average velocity calculated at each sampling time from the actuator's starting position.

2.5.3 Instantaneous velocity control

The velocity control is based on two Proportional-Integral (PI) controllers. As shown in Fig. 2.15, PI controller 1 and PI controller 2 are used to control the amplitude and the frequency respectively of the driving sawtooth voltage. The input of each controller is the error between the reference velocity V_{ref} and the actual instantaneous velocity v_i. The output of the *sign* function allows the definition of the direction of motion of the actuator.

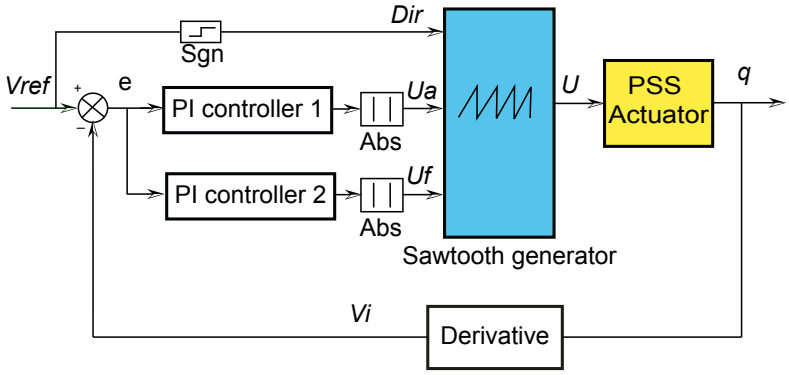

Figure 2.15: Control diagram of the closed loop instantaneous velocity control. V_{ref} and V_i are respectively the desired velocity reference and the actual instantaneous velocity of the slider.

The controller is designed in the discrete form as follows:

$$U_a(k) = K_{pa}e(k) + \sum_{i=1}^{k}(K_{ia}e(k)T_e) \tag{2.17}$$

$$U_f(k) = K_{pf}e(k) + \sum_{i=1}^{k}(K_{if}e(k)T_e) \tag{2.18}$$

The signals $U_a(k)$ and $U_f(k)$ are calculated from the PI controllers. They define respectively the amplitude and the frequency of the sawtooth voltage. K_{pa}, K_{ia} are the proportional gain and the integral gain respectively of PI controller 1. K_{pf}, K_{if} are the proportional gain and the integral gain respectively of PI controller 2. T_e is the sampling time and kT_e stands for the time. The derivative of the displacement is considered as the feedback signal.

Since the actuator is driven by a stick-slip principle, the instantaneous velocity used in the feedback loop becomes very high during the slip phases. This is a major impediment to achieve a good compromise between the closed loop bandwidth and the stability margin of the system. For instance, high gains of the controller lead to a fast response time but significant vibrations of the actuator will be produced.

For the implementation of the controller, based on a trade off between stability and response time, the selected gains are $K_{pa} = 0.00001\ Vs/\mu m$, $K_{ia} = 1.2\ Vs/\mu m$, $K_{pf} = 0.001\ Vs/\mu m$ and $K_{if} = 1\ Vs/\mu m$.

The controller has been designed using matlab/simulink and the implementation has been performed on the dSPACE controller board with a sampling frequency of 35 kHz. The control voltages U_a and U_f calculated with the controller board are connected to the input of the sawtooth generator to drive the PSS actuator.

The velocity references have been selected taking into account the characterization results of Fig. 2.14. Experimental results of the slider displacement with the closed loop instantaneous velocity control are shown in Fig. 2.16 for reference velocities of 500 μm/s, 1000 μm/s, 2000 μm/s, 3000 μm/s, 4000 μm/s and 5000 μm/s. For the evaluation of the controller performance, experiments have been performed in forward and backward directions.

For PSS actuators, using an instantaneous velocity control leads to a relatively long response

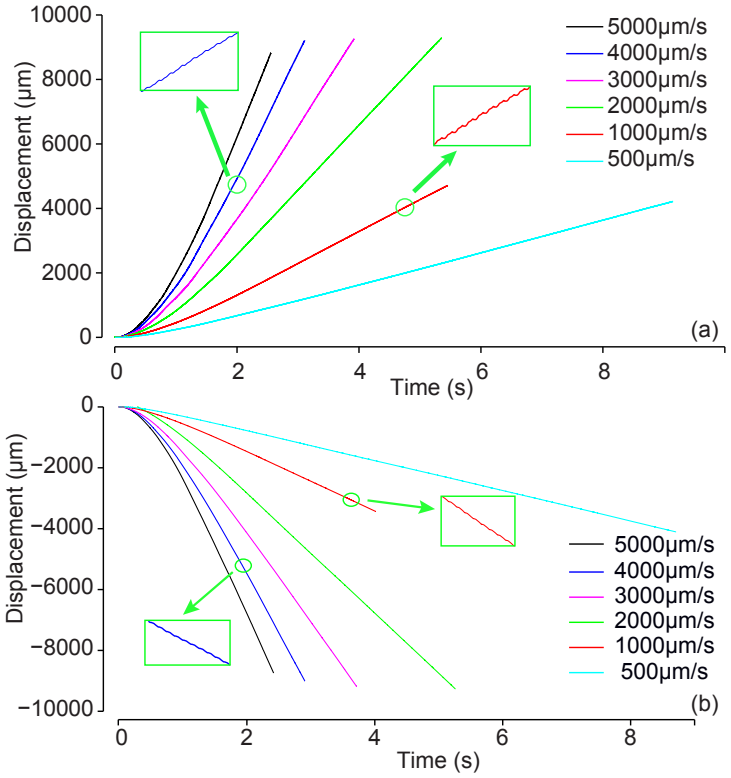

Figure 2.16: Experimental results of the displacement of the slider with the closed loop instantaneous velocity control. (a) Displacement in forward direction. (b) Displacement in backward direction. The PSS actuator is operating in the vacuum environment.

time which is more than 1 s in the range of the input reference [500 μm/s - 5000 μm/s]. This is an important issue for PSS actuators, which have a limited working range. For instance, the displacement range of the studied actuator is 12 mm. Using a reference velocity of 5000 μm/s, the actuator reaches the desired velocity in closed loop after having traveled the half of the total displacement range. Moreover, there are significant vibrations in the instantaneous velocity feedback signal as shown in Fig. 2.17. This is mainly due to the repetition of several sequences

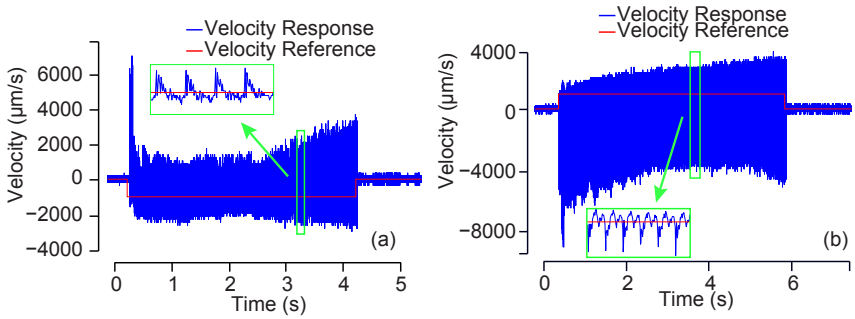

Figure 2.17: Experimental instantaneous velocity of the slider with the closed loop feedback for a reference of 1000 μm/s. (a) Velocity in forward direction. (b) Velocity in backward direction. The PSS actuator is operating in the vacuum environment.

of slip motions.

The instantaneous velocity control is an interesting solution for PSS actuators but it requires a severe compromise between stability and response time.

2.5.4 Average velocity control

The velocity of the slider can also be calculated by the ratio between the displacement and the time, i.e. the slope of the displacement with respect to the time. The velocity control describes the instant velocity state, and the slope control reflects the average velocity state. If a velocity control is applied, the average velocity must also converge to the velocity reference.

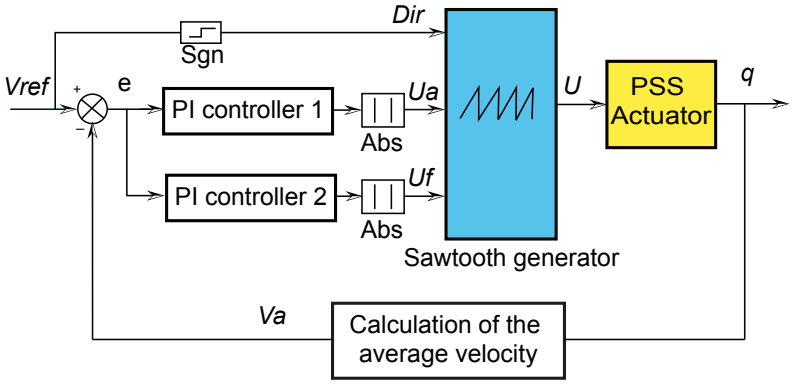

Figure 2.18: Control diagram of the closed loop average velocity control. V_{ref} and V_a are respectively the desired velocity reference and the actual average velocity calculated from the slider's starting position.

The average velocity is calculated by

$$V_a = \frac{q}{t - t_0} \tag{2.19}$$

Where V_a is the average velocity, q represents the displacement of the slider, t stands for the actual time and t_0 is the time when the slider starts moving (initial position).

The control diagram is shown in Fig. 2.18. It has the same working principle as that of the previous controller (Fig. 2.15) except that the output feedback is now the average velocity.

The ratio between the total displacement of the slider and the unwanted vibration generated at the slip phase is high. Therefore, the effect of the slip vibrations on the velocity control performance is very limited. With the average velocity control, it is then possible to find a good tradeoff between the stability and the response time. The gains of the controller can be increased to decrease the closed loop response time while keeping a safe stability margin.

For the implementation of the controller, the selected gains are $K_{pa} = 1\ Vs/\mu$m, $K_{ia} = 0.8\ Vs/\mu$m, $K_{pf} = 1.2\ Vs/\mu$m and $K_{if} = 2.5\ Vs/\mu$m.

The controller has been implemented in the controller board. Experimental results of the displacement of the slider with the closed loop average velocity control and the instantaneous

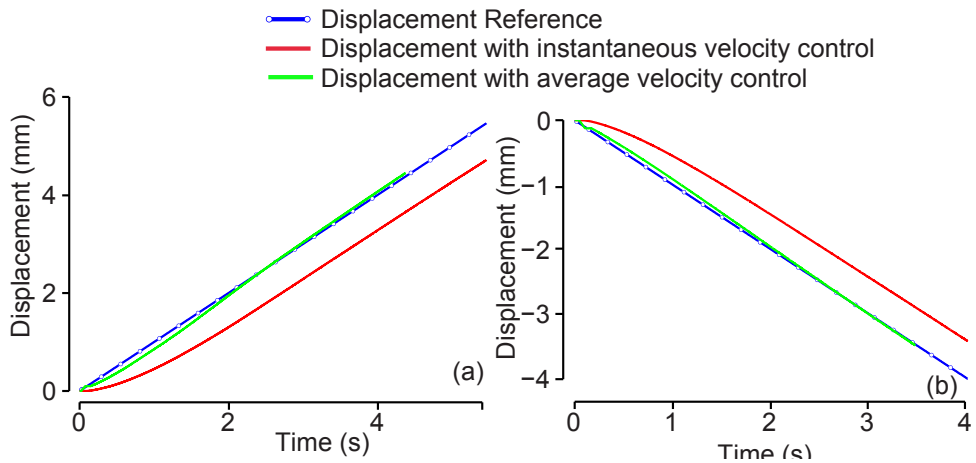

Figure 2.19: Experimental results of the displacement of the slider with the closed loop average velocity control and instantaneous velocity control for a velocity reference of 1000 μm/s. (a) Displacement in forward direction. (b) Displacement in backward direction. The PSS actuator is operating in the vacuum environment.

velocity control for a velocity reference of 1000 μm/s are shown in Fig. 2.19. This result demonstrates the ability to converge faster to a target position with a controlled average velocity. Thus, the slider's displacement curve is able to track and converge to the integral curve of the constant velocity reference.

Closed loop position tracking of a triangle wave when using the average velocity control and the instantaneous velocity control are shown in Fig. 2.20 (a) and Fig. 2.20 (b) respectively. The input reference is a square velocity signal of 0.2 Hz with -500 μm/s and +500 μm/s minimum and maximum values respectively. For tracking performance, the advantage of using the average velocity feedback to control the velocity of PSS actuators is demonstrated. The results have been compared with simulation data using the model presented in Section 2.2. For the simulation, the controller gains have been selected equal to those used in the experiments. A good agreement is observed between simulation and experimental data. This result shows also the potential of the non linear model for velocity control and observation.

2.6 Summary

This chapter has dealt with fundamental issues of modeling and low level motion control of the 3-DOFs (X-Y-Z) ISIR-robotex nano-robotic system. A new nonlinear dynamic model has been proposed for a class of nanorobotic systems using inertial piezoelectric actuators (PIAs). It describes the mathematical relation between the input voltage applied to a piezoelectric element and the displacement of the associated slider. The model is based on a coupled piezo/friction hysteresis model and an augmented multistate elasto-plastic friction model for which the breakaway displacement depends on the frequency and the amplitude of the input sawtooth voltage. This dependency is highlighted experimentally and represents the main novelty in friction modeling compared to the state of the art. This consideration has allowed a precise simulation of the motion of each individual PIA in a very wide operating range, i.e from the millimeter down to

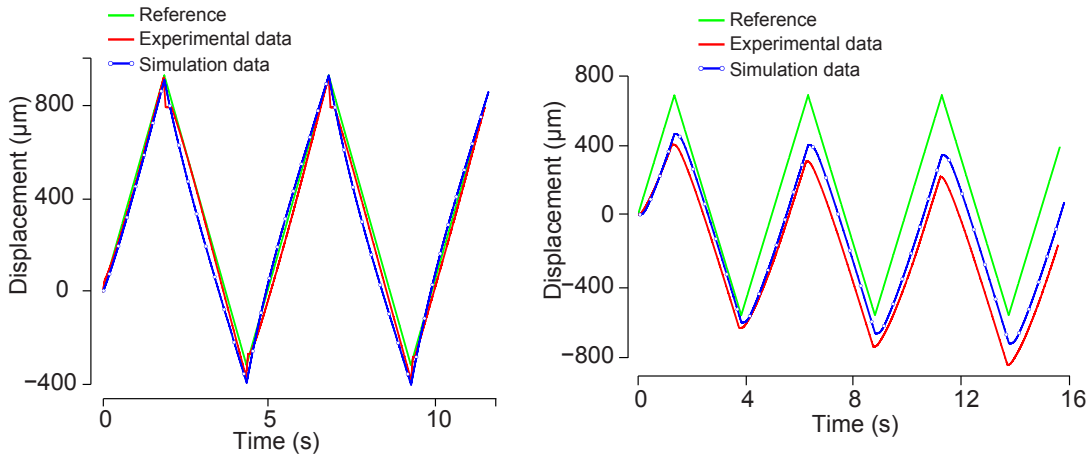

Figure 2.20: Simulation and experimental tracking results with the closed loop average velocity control (a) and instantaneous velocity control (b). The reference velocity is ± 500 μm/s. The PSS actuator is operating in the vacuum environment.

the nanometer; which is referred as a multi-scale displacement modeling. The maximum error of the closed loop simulation data and experimental data is 9.05 %. The model has been validated for closed loop control design considering two elementary tasks inside the SEM, namely 3D motion generation of the AFM probe and multi-scale AFM tip landing on sample surface. The model has shown its efficiency for observer and control designs as well as simulation and code generation for nano-robotics through a streamlined CAD/CAM engine programming. Finally, velocity characterization and velocity control of PIAs has been studied. A detailed map of the velocity versus the input amplitude and frequency voltage has been drawn based on experiments in forward and backward motion directions. This map is of importance to define the reachable velocities that can be set as input reference in closed loop velocity control. Velocity control strategies have then studied based on an instantaneous velocity feedback and an average velocity feedback. The low level controllers studied in this chapter will be used in the next chapters as the basis to deal will multi-scale path following issues of AFM probes with SEM vision feedback. The nonlinear model is the key for observer design.

Chapter 3

Atomic force microscope tip localization and path following through electron microscopy vision

The previous chapter has put the low level control foundations that will be used here. This chapter addresses the issue of high level multi-scale path following control of an AFM cantilever operating inside electron microscopes. The aim is to control the trajectory of the cantilever driven by a PIA using both electron microscope images and velocity measurements from optical encoders. The path following control is divided into two layers. The high level layer considers a Frenet frame kinematic model to compute velocity references along two orthogonal axes. The low level layer is based on an average closed loop velocity control of the nano-robotic system along the two orthogonal axes. For AFM tracking using SEM vision, one has to consider specific issues related to the compromise between the scan speed and the image quality of SEM. This restriction seriously limits the performance of conventional vision tracking algorithms such that those based on Template Matching when used with electron images. At high scan speed, the image quality is very noisy making very difficult to differentiate the AFM tip from the background, hence limiting the tracking capabilities. In this work, we explore for the first time the potential value of deep learning in the context of nano-robotic vision tracking inside SEM. The aim is to localize in real time the AFM cantilever from SEM images for any scan speed configuration and despite of low images quality. For that purpose, a data set of AFM tip images is build up from SEM images for the learning algorithm. Network performances are estimated under different SEM scan speeds. Thanks to the learning algorithm, experimental results show robust AFM tip tracking capabilities inside the SEM under various scan speed conditions. Experiments have been done considering different path shapes and the mean tracking error has been found less than 2 μm in the worst case.

3.1 Multi-scale Path Following of the AFM tip inside the SEM

3.1.1 Path Following versus trajectory tracking

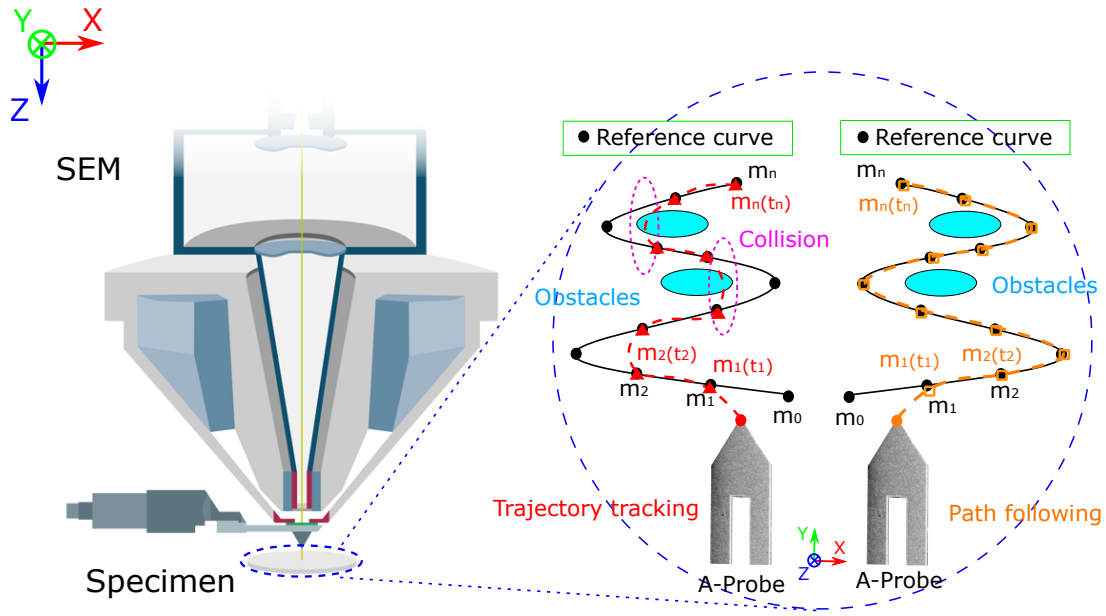

Figure 3.1: Comparison between trajectory tracking controller and path following controller. Trajectory controller may bypass and short-cut the reference curve by accelerations considering of time schedule, leading to the loss of geometric precision. Path following controller, regardless of time characters, is able to keep the desired tangential velocity and converge to the curve as accurate as possible.

To control the robot motion over a pre-specified geometric curve in a Euclidean space, there are usually two control methods: trajectory tracking and path following. The difference between the two controllers lies on the dependency on time. The trajectory-tracking controller relies on the time factor, where the reference path is defined with a time specification. On the other hand, the path following controller is time-invariant, where the reference path is defined without temporal constrains.

The temporal dependency of the path is therefore one of the main factors that differentiate the performances of the two controllers. As shown in Fig. 3.1, in the presence of perturbations and/or high curvatures along the reference path, the trajectory tracking controller will accelerate the robot and short-cut the reference curve to respect the time constraints during the tracking. This may lead to unexpected collisions between the robot and the obstacles close to the reference path. While in the same situations, as the path following controller has no time restrictions, only the geometric convergence of the actual robot path to the reference path is considered, thus avoiding the previously mentioned issues. Hence, in the case of perturbations or lag conditions, the path following controller achieves better performances than the trajectory-tracking controller in terms of geometric precision and convergence to the reference path.

In this thesis, the AFM tip path following control is not implemented for scanning or topography purposes but for manipulation of small scale objects inside the SEM. Therefore, no severe

time constraints are needed. Bypass or short cut behaviors in the trajectory tracking will bring the AFM tip close or in contact with obstacles, which is not desirable. What matters is that the AFM cantilever follows the exact specified reference curve, avoiding obstacles. In addition, with path following control, the longitudinal velocity may be modified according to the curve shape, length and curvature and the limited acquisition speed of SEM vision will requires a limitation in the AFM cantilever velocity within a feasible range. Finally, modifying the velocity profile will improve the transference efficiency of the AFM cantilever between different Regions Of Interest (ROI) for the vision tracking. Therefore, according to the above-mentioned reasons, the path following is a better choice than the trajectory tracking in the case of our study.

3.1.2 State of the art

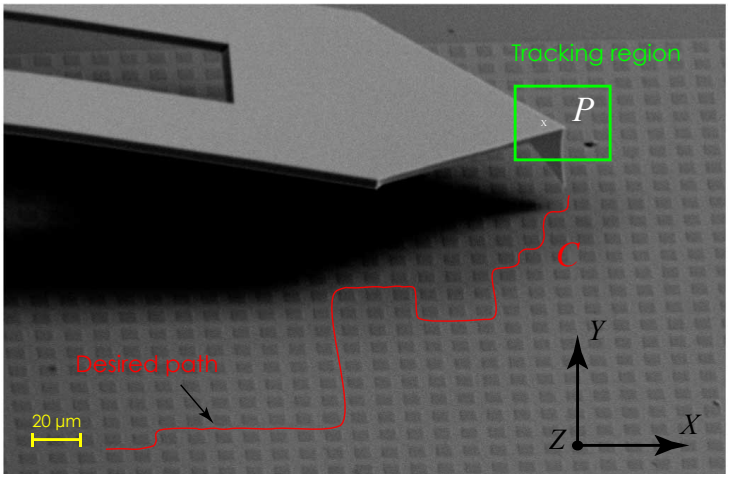

Figure 3.2: AFM cantilever observed with the SEM. The aim is to track the point P on the cantilever so that it follows the path C.

The objective of path following is that a point P on the robot follows a given in plane curve C without time constraints (Fig. 3.2). The distance between the point P and the closest point M on the curve C is minimized, i.e. stabilized at zero, while the robot is moving with a velocity v_0 [19] [20]. Velocity control is therefore one of the pivotal issues here. Path following has been deeply studied and applied in various fields of robotics. In recent published works, one can cite applications in mobile vehicles [121] [42] [72], aerial vehicles [97], underwater vehicles [155] [145] [103], surgical robotics [125] [31] and micro- robotics [99]. The studied systems can be classified into holonomic [31] [158] and non-holonomic [121] [122].

Despite the widespread use of inertial actuated nano-robotic systems in laboratories [30] [3], there is up to now no work in the literature nor demonstration of path following control for robotic systems actuated by piezoelectric and inertial principles and more specifically by stick-slip actuators. There is therefore no demonstration of multi-scale path following control for AFM cantilevers with SEM vision.

The essence of path following is to control the robot velocities so that it converges into the reference path. Specific driving methods of inertial actuators are needed to obtain a smooth motion trajectory. This is of importance to reduce undesired vibrations caused by the stick and slip transitions and the presliding dynamics [36]. Hunstig et al. [35] proposed some driving

methods considering three main criteria, namely the steady state velocity, the smoothness of motion, and the start-up time. Liang et al. [73] have made a characterization of the velocity with respect to the amplitude and the frequency of the input sawtooth volage to evaluate the reachable velocities that can be used a an input reference in a closed loop control. Velocity control based on an instantaneous velocity feedback and on an average velocity feedback have then been studied. The latter one have shown better results in terms of motion vibration damping. The average velocity control described in [73] will be used here as a part of the path following control.

3.1.3 General problem description

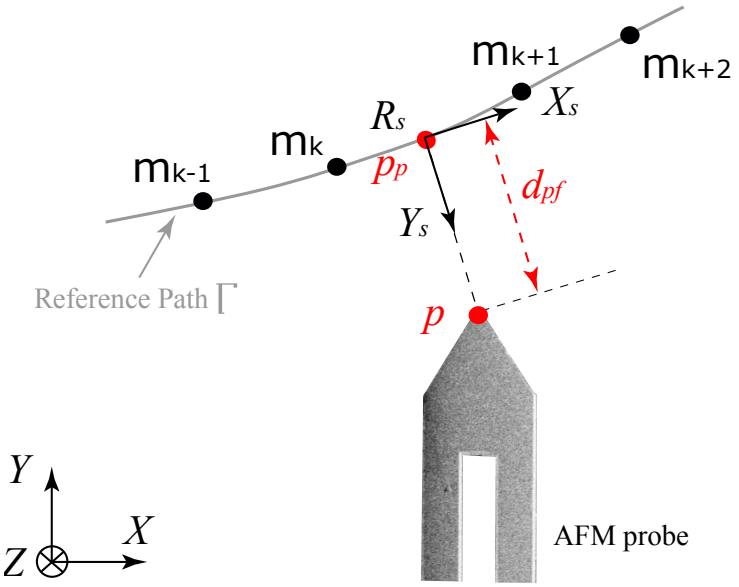

Figure 3.3: Define projection distance d_{pf}, by projecting end-effector P onto the reference curve Γ, resulting projection point P_p.

The first step toward path following is to define the geometric reference curve. It can be defined by a path planning algorithm using SEM vision. To be more user-friendly, the operator can also draw the desired path curve through mouse click on the screen of the SEM. The second step is to land the AFM probe on the starting point of the reference curve. Here the landing procedure described in the previous chapter can be used. At each sampling time, the path following algorithm minimizes the projection distance d_{pf} and simultaneously maintains the desired tangential velocity along the curve. The distance d_{pf} is the projection distance between the point P on the AFM probe and the point P_p on the reference path Γ (Fig. 3.3).

3.1.4 Kinematic Model

The path following control strategy is designed considering the specific case of the 2-DOF holonomic inertial actuated nano-robotic system (i.e. X and Y axes of the Cartesian nano-robot of [21]). Let us consider the local frame R_p, the *Frenet* frame R_s and the world frame R_0 [94] as in Fig. 3.4. The controller specifies the local velocities of the AFM tip $\mathbf{v_{adv}}$ and $\mathbf{v_{rec}}$, with respect to the *Frenet* frame R_s. These velocities are further projected onto X and Y axes as

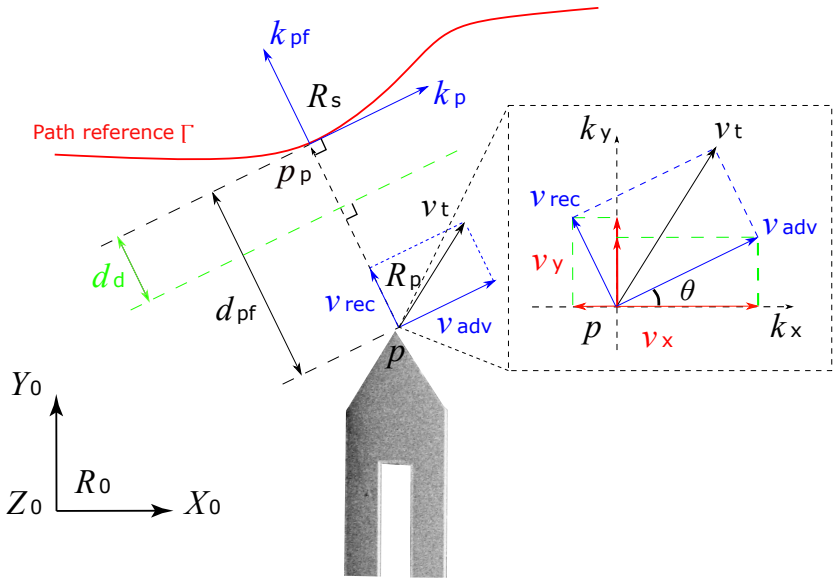

Figure 3.4: *Frenet* frame based kinematic model, calculating the tangential velocity $\mathbf{v_{adv}}$ and the normal velocity $\mathbf{v_{ret}}$ in the *Frenet* frame R_s and projected into $\mathbf{v_x}$ and $\mathbf{v_y}$ in the world frame R_0.

$\mathbf{v_x}$ and $\mathbf{v_y}$ in the world frame R_0. With $\mathbf{v_x}$ and $\mathbf{v_y}$ as input, the closed loop velocity control previosulsy designed in [73] is applied for each axis of the nano-robotic system driving the AFM cantilever. The aim is that the AFM tip position converges to a defined curve Γ in world frame.

In this work, the AFM tip orientations in the frames R_p, R_s and R_0, are assumed to be fixe. The AFM tip position is characterized by a point $\mathbf{p}(x, y)^T$ in world frame R_0, which is obtained from SEM images. The point $\mathbf{p_p}$ is the perpendicular projection of $\mathbf{p}(x, y)^T$ in the reference curve Γ. The AFM tip translation velocity $\mathbf{v_t}$ within the frame R_s, is divided onto the tangential velocity $\mathbf{v_{adv}}$ along the path, and the normal velocity $\mathbf{v_{rec}}$ perpendicular with the path. In Fig. 3.4, $\mathbf{k_p}$ and $\mathbf{k_{pf}}$ are tangential and normal unit vectors respectively of Γ at $\mathbf{p_p}$. Moreover, $\mathbf{k_x}$ and $\mathbf{k_y}$ are the unit vectors of x and y axes in the frame R_0 respectively. The path following error is the distance $||\mathbf{d_{pf}}|| = \mathbf{p_p} - \mathbf{p}$. In equation (3.1), the AFM tip velocity $\mathbf{v_t}$ is an independent variable.

3.1.5 Path Following Control Strategy

The control process consists of a high level control and a low level control (Fig. 3.5). The high level control computes and assigns the tangential velocity $\mathbf{v_{adv}}$ and normal velocity $\mathbf{v_{rec}}$ to steer the AFM tip to converge to the path reference Γ. In the low level control, the projection of $\mathbf{v_{adv}}$ and $\mathbf{v_{rec}}$ on X and Y axes as $\mathbf{v_x}$ and $\mathbf{v_y}$ are used as input references for the closed loop inertial actuators velocity control.

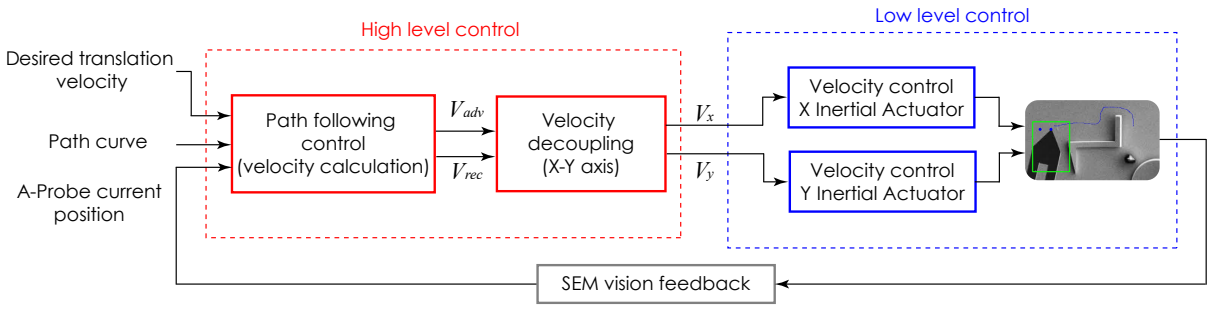

Figure 3.5: Two-layer path following control scheme on inertial nano-robotic system: the high level control, considering the translation velocity v_t, reference path and end-effector position, computes the tangential velocity v_{adv} and perpendicular velocity v_{ret} converging to reference path; low level control decouples v_{adv} and v_{ret} into v_x and v_y as input, apply velocity control on inertial actuators by double-PI controllers; SEM tracks and feedback robot position across imaging

3.1.5.1 Velocity assignment in Frenet Frame

The velocities $\mathbf{v_{adv}}$ and $\mathbf{v_{rec}}$ are calculated from the specified desired translation velocity $\mathbf{v_t}$ of the AFM tip in the world frame R_0, where:

$$\begin{cases} ||\mathbf{v_t}|| = v_{\text{constant}}, \\ \mathbf{v_t} = \underbrace{\alpha \mathbf{k_p}}_{\mathbf{v_{adv}}} + \underbrace{\beta ||\mathbf{d_{pf}}|| \mathbf{k_{pf}}}_{\mathbf{v_{rec}}}, \end{cases} \tag{3.1}$$

α is the amplitude of the tangential velocity $\mathbf{v_{adv}}$ and $\beta||\mathbf{d_{pf}}||$ is the amplitude of the normal velocity $\mathbf{v_{rec}}$ toward the path reference. The AFM tip velocity $\mathbf{v_t}$ is specified as constant $v_{constant}$ to ensure a smooth and stable tracking. α and β are determined by the following rules:

$$if \begin{cases} ||\mathbf{d_{pf}}|| < d_d, \begin{cases} \beta = constant \\ \alpha = \sqrt{||\mathbf{v_t}||^2 - ||\mathbf{v_{ret}}||^2} \end{cases} \\ ||\mathbf{d_{pf}}|| > d_d, \begin{cases} \beta = constant \\ \alpha = 0 \end{cases} \end{cases} \tag{3.2}$$

where d_d is a threshold distance between the AFM tip position and the path reference.

3.1.5.2 Velocity assignment in the world frame

The projected velocities $\mathbf{v_x}$ and $\mathbf{v_y}$ in the world frame are obtained from $\mathbf{v_{adv}}$ and $\mathbf{v_{rec}}$ as follows:

$$\begin{cases} \mathbf{v_x} = \mathbf{v_{adv}} \cdot \mathbf{k_x} + \mathbf{v_{rec}} \cdot \mathbf{k_y}, \\ \mathbf{v_y} = \mathbf{v_{adv}} \cdot \mathbf{k_y} + \mathbf{v_{rec}} \cdot \mathbf{k_x}, \end{cases} \tag{3.3}$$

$\mathbf{k_x}$ and $\mathbf{k_y}$ are the unit vectors of X and Y axes in R_0. The velocities $\mathbf{v_x}$ and $\mathbf{v_y}$ will be used as velocity control input references to achieve the final path following task.

3.1.6 Template Matching Real-Time Visual Tracking

Template Matching is a conventional technique to find areas inside an image that are similar to a template (patch). When applied to a moving object in a sequence of images, it allows tracking its motion. The algorithm input includes two primary components:

- **Source image (I):** the image inside which the template is searched.
- **Template image (T):** the patch image that will be compared with the source image.

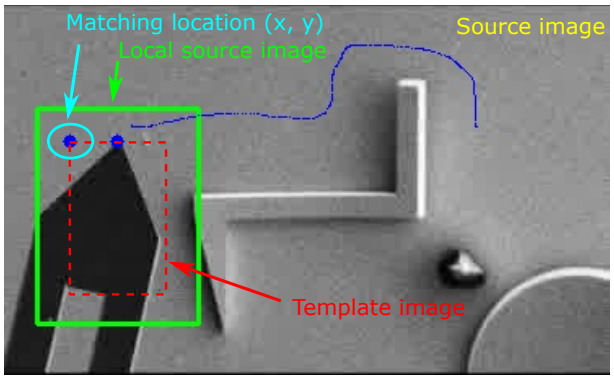

Figure 3.6: Template Matching illustration. Matching the template image within the source image, generates more wrong leap localization estimation. Matching the template image within the local source image, moving and updating with the ifentified coordinate, generates stable localization estimation.

The goal is to find the most probable position of the template in the source image (Fig. 3.6). To this end, the template is placed at any possible position in the image and a similarity measurement between the template and the source image is computed. More specifically, let us consider T(x,y) the template and I(x,y) the source image. A score image R(x,y) is estimated as follows:

$$R(x,y) = \frac{\sum_{x',y'}(T(x',y') \cdot I(x+x',y+y'))}{\sqrt{\sum_{x',y'} T(x',y')^2 \cdot \sum_{x',y'} I(x+x',y+y')^2}} \tag{3.4}$$

The higher the score in R(x,y) is, the more likely the object is present at this position. Due to noise in SEM images, some bad detections, far from the previous detection (time t-1) can be found. To improve the robustness and accelerate the computation time, a local source image, which is 20 pixels bigger than the template image and localized at the previous detection is considered. This consideration significantly improves the stability of the tracking result with template matching. Fig. 3.6 illustrates this process. The template is represented in red and is searched in the local source image represented in green.

3.1.7 Experimental Validation

The path following controller of Fig. 3.5 is implemented in real time on the nano-robotic system holding the AFM cantilever. The template matching algorithm is used to track the position of the AFM tip. All the experiments are done inside the SEM. Three main performances are evaluated, namely the path following precision, repeatability and robustness w.r.t to the AFM tracking velocity. Different types of reference paths are tested, i.e. line shape reference curve, circle shape reference curve and sine shape reference curve. For a tracking velocity of 3 μm/s, in the steady state, the mean of the error is no more than 2 pixels which corresponds to 2 μm for the 3 reference paths (Fig. 3.7).

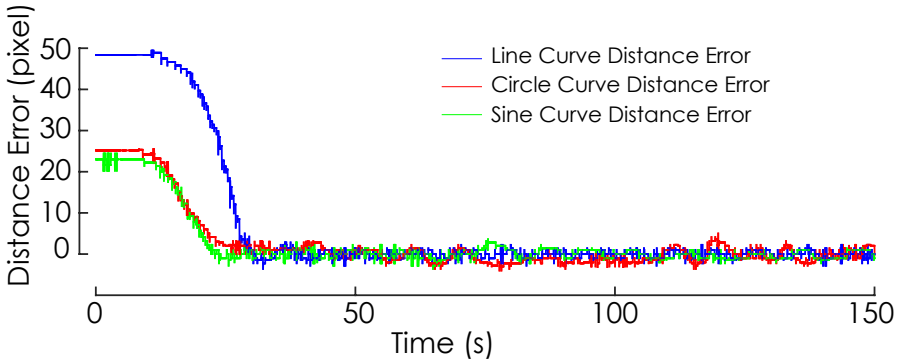

Figure 3.7: Path following control deviation d at translate velocity of 3 μm/s, line curve control deviation, circle curve control deviation, sine curve control deviation.

To analyze the repeatability of the path following, for each path reference curve, the AFM tip path following is repeated 10 times with a longitudinal velocity of 3 μm/s as shown in Fig. 3.8. The RMS error is found equal to 1.8420, 1.5316 and 1.3673 pixels for the line, the circle and the sine reference paths respectively. These results demonstrate the high repeatability of the path following control process.

In the third experiment, the effect of the tracking velocity on the path following performances is evaluated. Taking into account the closed loop sampling frequency of the controller and the vision tracking capability, the tracking reference velocities used for the robustness analysis of the path following are 2 μm/s, 3 μm/s and 4 μm/s. Form the results of Fig. 3.9, it can be seen that a path following under velocities of 2 μm/s and 3 μm/s is much smooth than with 4 μm/s. The effects of these velocities on the performances of the controller are shown in in TABLE 3.1. A path following control at 2 μm/s takes much more time to follow the given path. Control under 3 μm/s achieves the best performance with the smallest RMS errors and STD errors, compared with the two other velocities.

In the forth experiment, the controller is applied when the path is drawn on the computer screen by the user using a mouse click at 3 μm/s. The tracking result is shown in Fig. 3.10. The AFM probe can follow a manually pre-defined path, which is of importance towards a user-friendly use of dual AFM/ SEM.

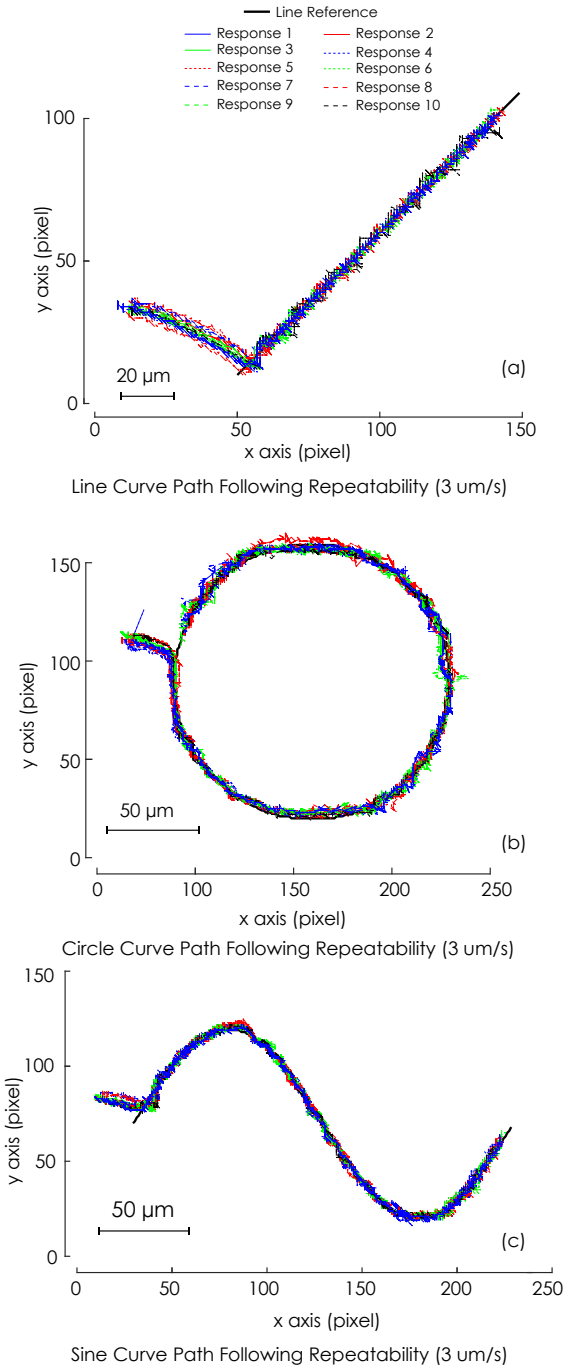

Figure 3.8: Repeatability test, applying on line (a), circle (b) and sine reference (c) curves, at translate velocity of 3 μm/s

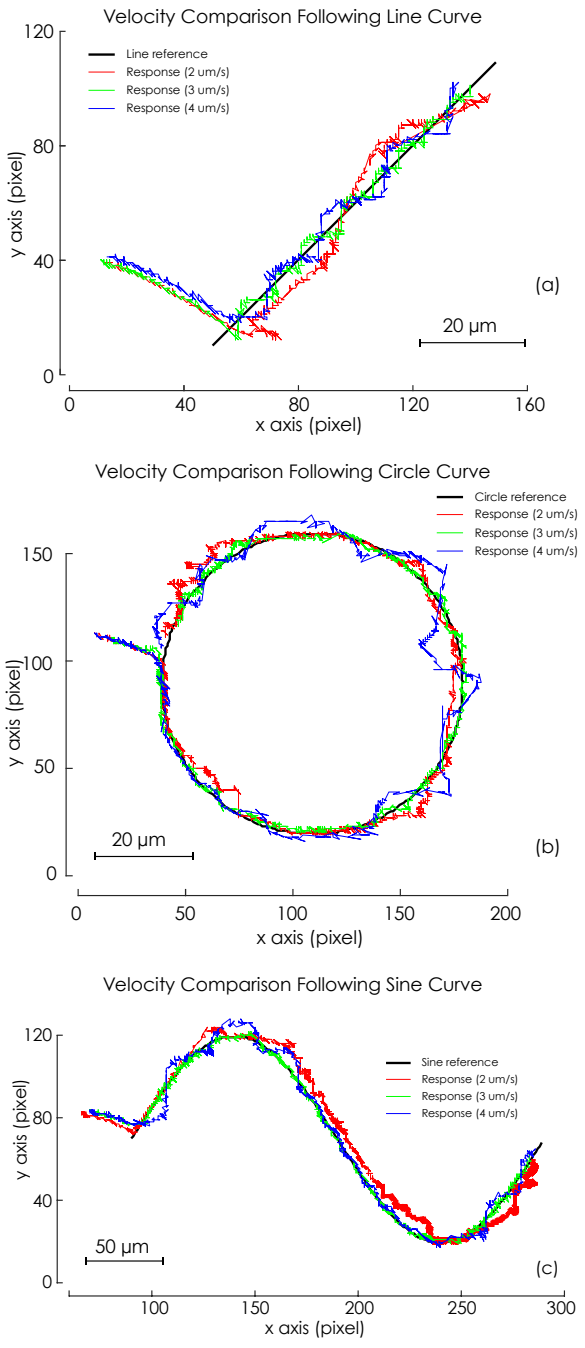

Figure 3.9: Velocities (2 μm/s, 3 μm/s, 4 μm/s) affections comparison under path following control on line (a), circle (b) and sine (c) reference curves.

	Line		Circle		Sine	
Velocity	RMS	STD	RMS	STD	RMS	STD
2 μm/s	6.627	6.587	3.696	3.628	4.428	3.277
3 μm/s	5.068	4.995	1.647	1.647	1.000	0.985
4 μm/s	5.199	5.087	7.331	7.232	2.684	2.641

Table 3.1: Summary of path following performance comparison (in pixels) under 2 μm/s, 3 μm/s, 4 μm/s with given line, circle and sine reference curves.

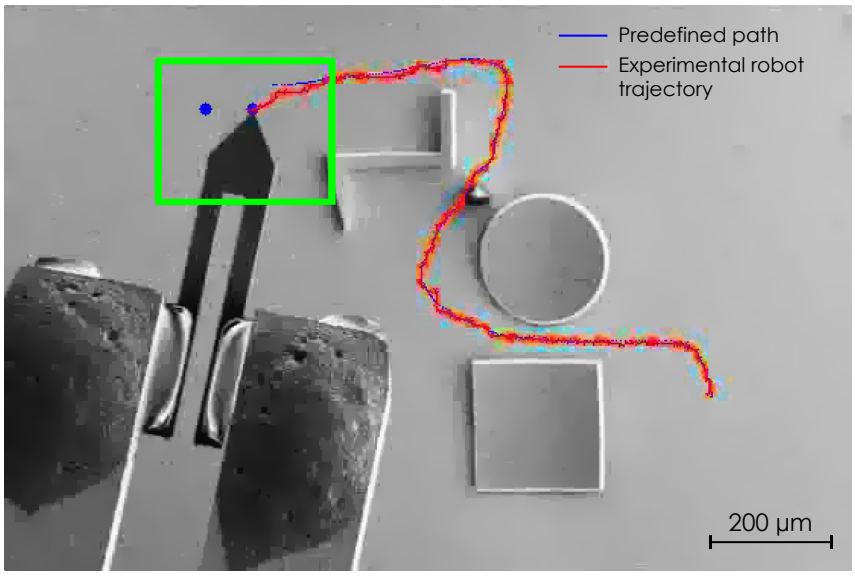

Figure 3.10: Path following control of shape-adaptability test result at 3 μm/s, inside SEM.

3.2 Deep learning for AFM tracking and path following with SEM vision

In Section 3.1, the conventional Template Matching algorithm has been used for visual tracking based on SEM vision. Path following has been successfully implemented when the background of the SEM images is not noisy and with no elements with complexe shapes. However, experiments have shown that the tracking is lost when these conditions are not satisfied which greatly limits the applicability of the path following in more usual situations of SEM uses.

3.2.1 SEM image processing

Several tracking algorithms are available using conventional image processing methods. Standard algorithms are divided into 3 main steps. The first one is the preprocessing that decreases the noise in images. It can be done using a Gaussian filtering, or a nonlinear anisotropic diffusion approach [104]. Secondly, the image is binarized in order to localize a Region of interest (RoI). More or less advanced methods can be used such as segment detection method (SDM) [133] or

binary large object (BLOB)-detection [163]. Some morphological operations [120] are often used to improve the detection. The third step is the RoI tracking that is often performed using simple heuristics. The lack of robustness of the RoI detection step has led to another kind of methods that skips this step. It is based on the previously used method based on template matching where a template is searched in the image using the sum-of-squared-differences (SSDs) between the image and the template or using a correlation. However, these algorithms are highly sensitive to variations of the contrast, the brightness or the signal to noise ratio [133]. Experiments carried out in the context of this thesis have shown that template matching performance decreases with decreasing the signal to noise ratio. Therefore, a more powerful image processing method is needed to track in a robust way an AFM cantilever inside a SEM.

3.2.2 Deep learning

Deep learning is a class of machine learning. It is increasingly applied in modern tricky computer vision issues. This is thanks to its outstanding capability to distinguish and extract target representations from massive and intricate data, showing significant superiority and potential to enhance robotic performances on various aspects, such as speech recognition and visual servoing. Deep convolutional neural networks (CNNs) are driving the advances in recognition for a multitude of computer vision challenges, illustrating highly superiority on both holistic and local feature extraction [81]. The application and combination of convolutional layers and pooling layers are the key factors that boost the outperformance of CNNs. Convolutional layers, enable the network to extract local features that are choosen and learned according to the application.

Deep Neural Networks (DNNs) have achieved remarkable success on both image classification [64] and object localization. Modern approaches perform at the same time multiple objet classifications and localizations. Among them, some methods [32] use an external RoI proposal generator and apply a classification algorithm with a box regression to recognize the object and refine its position. In R-CNN [32], each RoI is resized to a fixed size and pre-trained. CNN network is employed to extract a feature vector of size 4096. Multiple SVM are learned on these vectors to perform the multi-classes classification. Then, for each positive classification, a linear regression is done to refine the position of the object. This method is time consuming as the feature extraction, the classification and the regression and done for each RoI (2000 in the original article). An improvement is done in Fast R-CNN [48] as the CNN is applied only once on the whole image. The feature vectors are extracted after the CNN, at the localizations of the RoI. Recent approaches such as Faster R-CNN [113], SDD [80] or YOLO [112] change the two-step method and include the region proposal generator in the network in an end to end way. They use a multi-part loss that combines a classification loss and a regression loss. A good review of recent techniques can be found in [4]. In the previous approaches, the localization is made using bounding box and are useful to coarsely localize the object in the image. Other works consider the estimation of the pose of complex object. This problem has been widely addressed for human pose estimation [138], [96]. Two main approaches can be distinguished: those that predict heatmaps (map of presence probability) and those that directly predict the position (x, y) of each joint. While the first methods [96] are based on hourglass or stacked hourglass network, the second ones [138] use generic convolutional layers and regression. This kind of approach, also used in [19] is well adapted to our problem as we can directly regress the x and y positions of the AFM tip from SEM imaging, in a more precise way than using bounding box.

3.2.3 Motivation

The aim is to tackle the issue of tracking the position of the AFM tip inside the SEM in various scan speeds of the electron microscope. Let us recall that the SEM used in this work is the ZEISS EVO-LS 25. This microscope features 15 scan speed modes. The scan mode 1 is the fastest one but it provides very noisy images that do not allow to distinguish precisely the AFM tip from the background as shown in Fig. 3.11(a). The scan mode 15 is the slowest one, it requires much more time to get an image and leads to the best quality of image among other scan speed modes. It is possible for instance to see the image quality at scan speed mode 5 in Fig. 3.11(b). This mode requires 15 s to get an image.

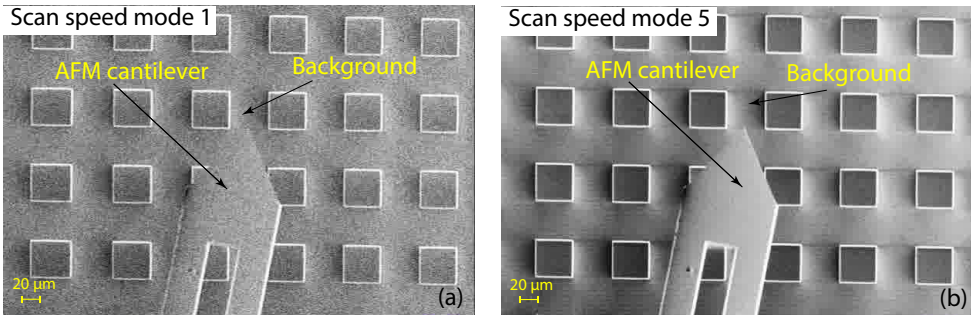

Figure 3.11: AFM tip observed with the SEM using a scan speed mode 1 (a) and 5 (b). The scan speed 1 is the fastest one, it allows obtaining an image every 1.3 s but the image quality is bad, it is hard to differentiate the AFM tip from the background. The scan speed mode 5 allows obtaining a better image quality, but it requires 15 s to acquire an image.

To this end, a learning algorithm that allows extracting precisely the coordinate of the AFM tip in various scan speeds and despite of the noisy images of the fast scan modes is studied. A ConvNets based network is built to regress the AFM tip localization within SEM imaging, which is further used as position feedback in path following control loop. This work shows the potential of Deep Learning and enriches the feasible solutions to deal with the tricky SEM imaging issues.

3.2.4 Deep learning model for AFM tip coordinate regression in SEM imaging

The aim is to develop an end-to-end, pixel-wise prediction of the AFM tip coordinates (x, y) from the images acquired by the SEM. The studied images are very specific grayscale images, with many geometric and repetitive patterns. It is difficult to take advantage of the large databases in the literature such as imagenet, Microsoft coco dataset [76] or other applications like human pose estimation [96]. Therefore, a specific model has been built to localize the AFM tip in images captured by SEM.

3.2.4.1 Problem definition and model architecture

Among the deep learning methods, those based on a first detection of bounding boxes cannot be used in our application, as the whole object is not fully visible with the magnification of the SEM images. So, we propose to directly regress the extremity (x, y) of the tip using standard

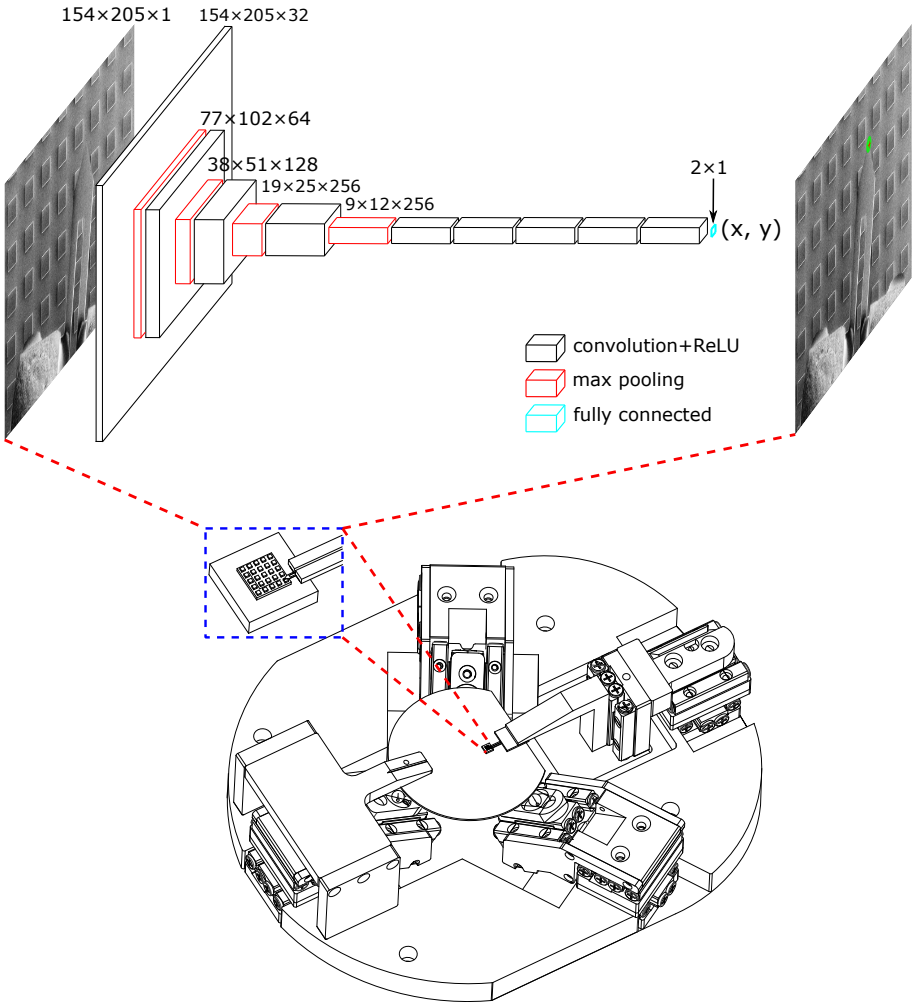

Figure 3.12: AFM tip localization with regression network. Classification layers as feature extractor first, followed with fully convolutional layers for fine-tuning and regresses numerical AFM tip coordinate by fully connected layer.

CNN [138]. As preprocessing, data normalization is implemented by subtracting the mean and dividing it by the standard deviation of the pixel values. The image is then passed through several layers. All convolutional layers have a size of 3 x 3 pixels, a stride fixed to 1 pixel and a padding to keep the original size of the image. The spatial max-pooling layers are done with 2 x 2 pixels window and a stride of 2. The last layers are fully connected layers with two units that predict the x and y positions of the AFM tip. The Rectified Linear Unit (ReLU) activation function is used for all the layers except the fully connected one that has a linear activation function. Moreover, a Local Response Normalization (LRN) is done before the ReLU layers.

3.2.4.2 Loss function

The last fully connected layer gives the prediction of the numerical tip coordinates $\mathbf{x_p} = (x_p, y_p)^T$. The loss is estimated as the Euclidean distance between the predicted coordinate $\mathbf{x_p} = (x_p, y_p)^T$ and the ground truth coordinates $\mathbf{x_g} = (x_g, y_g)^T$. This loss, named Mean Square Error (MSE),

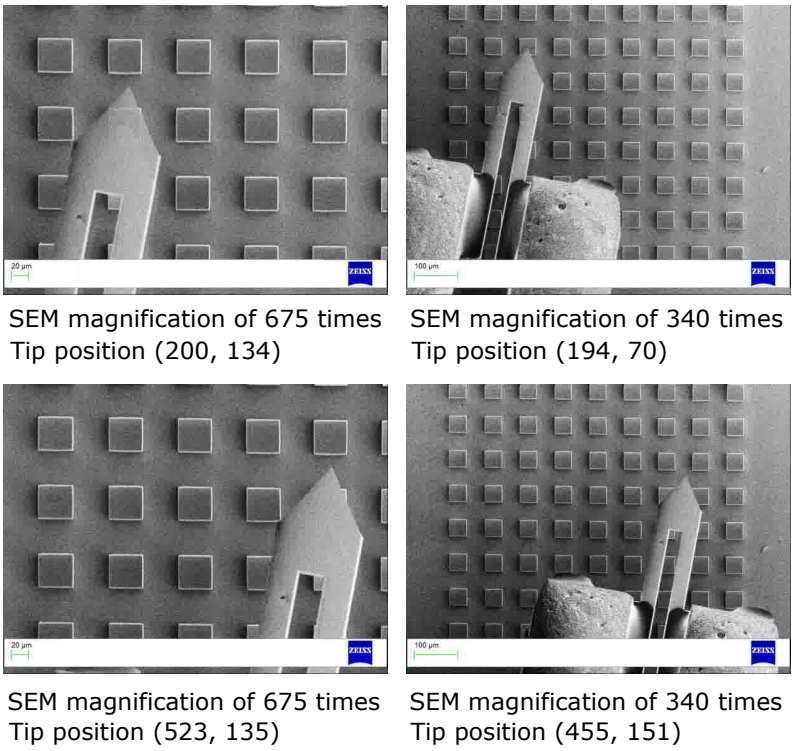

Figure 3.13: Examples of AFM tip images used for the learning process.

is defined by:

$$L = \frac{1}{N}\sum_{i=1}^{N} ||\mathbf{x_p} - \mathbf{x_g}||^2 \tag{3.5}$$

Where N is the number of images in the batch.

3.2.4.3 Construction of SEM imaging database

Some popular datasets of natural images, such as imagenet or Microsoft coco dataset [76] exist in the literature. However, no training data are available for AFM cantilevers with SEM images. Thus, a dedicated database is built for AFM tip localization. In order to consider the images under conventional SEM standard uses, images are captured with a wide range of SEM magnification, distributing at 340, 377, 423, 474, 526, 572, 622, 675 times. This leads to images with an important variation in the size of the AFM tip. Moreover, the position of the tip is changed during the acquisition to simulate all the possible configurations as illustrated on Fig. 3.13. The final database contains 1476 images of size 612 × 460 collected through UDP communication from SEM at scan speed mode 3.

3.2.5 Tip localization using the learning network

3.2.5.1 Experimental setup

For each image of the database, the extremity tip positon is manually annotated and the x and y coordinates that will be regressed are registered. Then, the whole database (1476 images) is split in a training part (80%) and a testing part (20%). Considering the training efficiency and the computation capability, the raw images are resized to 205 × 154 pixels. The network is trained using Keras in Jupyter Notebook. For each mini batchsize of 64, Adam optimizer is chosen with changing learning rate, initialized from 10^{-4}, dropping 0.6, every 50 epochs (500 epochs in total). The whole train takes 80 *mins* on a 4 *GB* NVIDIA Quadro K2200 and a single prediction takes 17 *ms*. Thus, 3.5 images per second can be processed.

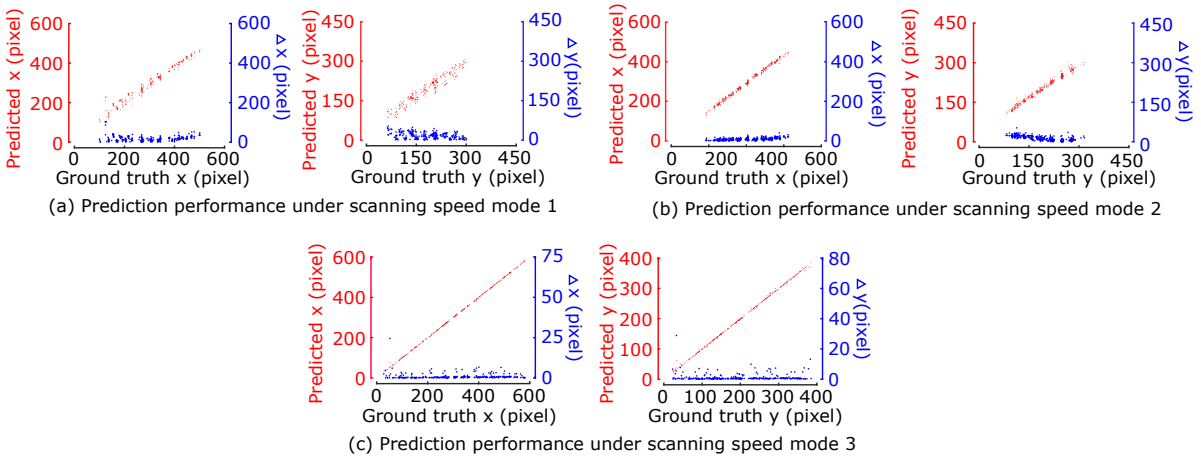

Figure 3.14: Proposed learning network prediction results of AFM tip coordinates, x and y respectively (red marked) and corresponding deviation analysis (blue marked). AFM tip coordinate (x, y) prediction under SEM scan speed mode 1 (a), 2 (b) and 3 (c).

3.2.5.2 Results

The Root Mean Square error on the 295 test images, which represents the mean Euclidian distance between the prediction and the ground truth, is 3.83 pixels. Prediction and ground truth of AFM tip coordinates x and y, are compared and analyzed as shown in Fig. 3.14(c). Good results are obtained, except for the extreme localizations on both axes, as shown with the deviation analysis (blue marked). This illustrates that the proposed learning network performs better in the central image area compared with border, due to less quantity of boarder-tip-distributed training samples. In order to test the generalization and the adaptability, SEM images at scan speed mode 1 (268 images) and 2 (343 images) are presented as input to the proposed learning network, without re-learning. These images have a low signal to noise ratio, e.g. Fig. 3.11(a). Prediction results, shown in Fig. 3.15 and further separately presented on x and y axes in Fig. 3.14, are still close to the real position. This enables the nano-robotic system to manipulate under different real-time demanding situations. Specifically, under different SEM scan speed modes, the prediction performances are analyzed and summarized in TABLE 3.2. Prediction under SEM scan speed mode 3, performs the most precisely, with the Euclidian

	X error			Y error			Distance error		
Scaning	Mean	RMS	STD	Mean	RMS	STD	Mean	RMS	STD
Mode 1	17.86	23.14	14.73	17.84	21.13	11.34	27.97	31.33	14.15
Mode 2	9.10	11.20	6.54	13.70	16.10	8.47	17.50	19.61	8.86
Mode 3	0.93	2.30	2.10	1.02	2.40	2.17	1.53	3.32	2.95

Table 3.2: Learning network performance, prediction errors analysis (in pixels) of AFM tip coordinate (x, y) and Euclidian distance (distance between predicted localization and ground truth), under SEM scan speed mode 1, mode 2, mode 3.

distance error (distance between predicted AFM tip localization and ground truth) no more than 4 pixels, and the standard deviation of this distance less than 3 pixels. When the scan speed mode decreases, the errors increases.

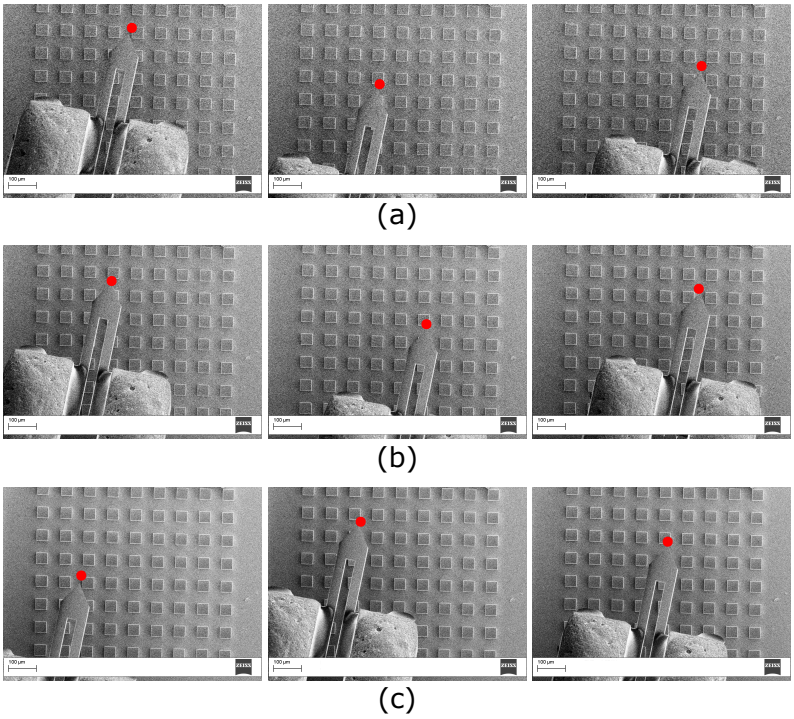

Figure 3.15: AFM tip coordinate prediction results, by the proposed learning network from SEM image. Coordinate predictions under SEM scan speed mode 1 (a), 2 (b) and 3 (c).

3.2.6 Path following with the learning network regression

Straight line shape and sine shape path references are used. The tracking process is implemented under different SEM scan speeds, mode 1, mode 2 and mode 3, with increasing image quality, but slowing down the feedback. The Template Matching tracking method is applied to make comparison on track performances. As shown in Fig. 3.16, with the localisation prediction of the network, the AFM tip is able to track the path references in real-time based on SEM vision under different scan speeds. However, due to the image quality and the background around the AFM

tip, Templated matching loses the track at the very beginning of the path following process. Fig. 3.17 illustrates the tracking errors.

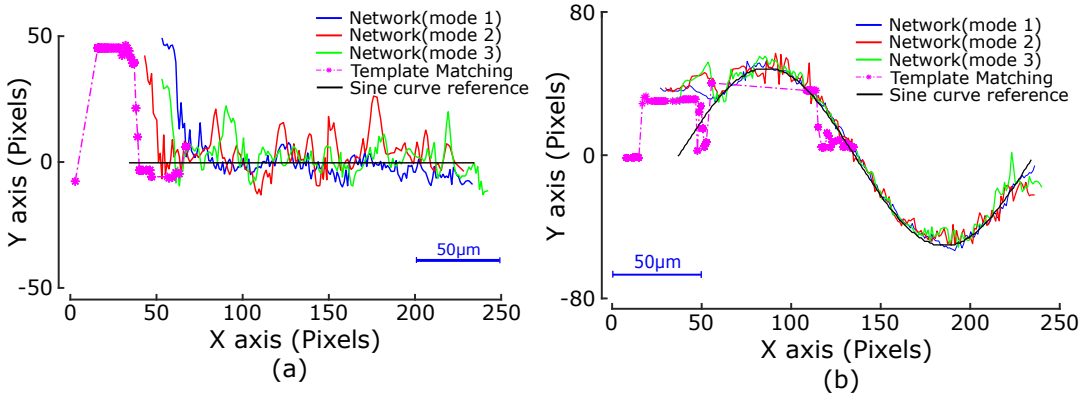

Figure 3.16: Path following control performances after LOWESS smoothing, at a translation velocity of 3 μm/s with a line path reference (a) and a sine path references (b).

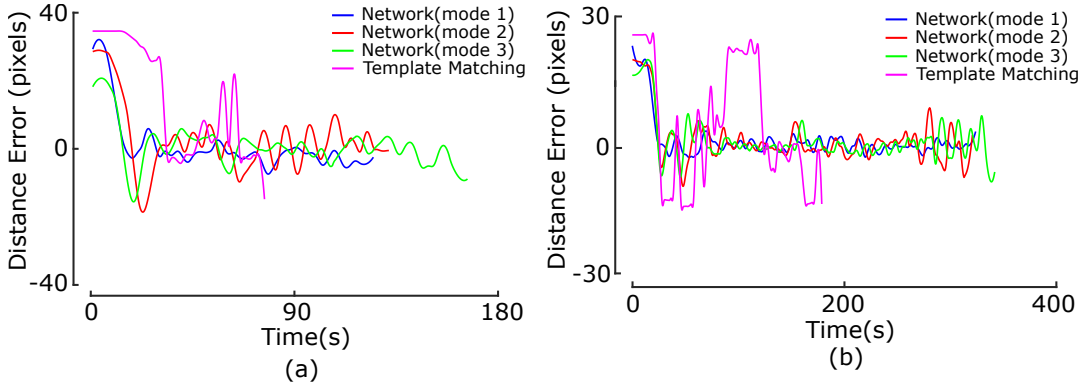

Figure 3.17: Path following tracking errors d_{pf}, at translate velocity of 3 μm/s with a line path reference (a) and a sine path references (b).

3.3 Conclusion

This chapter has dealt with atomic force microscope tip localization and path following through electron microscope vision. The two main issues have been related to the driving principle of the AFM probe which is based on inertial piezoelectric actuators and the second one has been related to the real time AFM tip localization using SEM images under various conditions, i.e. scan speed and background complexity. For the first issue, the key has been to master the velocity control of PIA actuators as it is the basis of the path following. The path following control has been divided into two layers. The high level layer considers a Frenet frame kinematic model to compute velocity references along two orthogonal axes. The low level layer is based on an average closed loop velocity as described in chapter 2. The accuracy, the repeatability and the robustness of the path following with respect to the path profile and the velocity have been evaluated experimentally. The mean tracking error has been found less than 2 μm in the worst case. For the second issue, it has been demonstrated that conventional visual tracking

algorithm such as those based on template matching fails to track AFM-Probes from SEM vision under scan speeds 1, 2 and 3 and in some specific background conditions. Hence, a learning algorithm based on Neural Networks (ConvNet) has been built for accurate localization of AFM tips inside SEM for various operating conditions in which template matching fails to detect the tip. A database has been constructed from SEM images for the learning process. The efficiency of the algorithm when used for path following control of the AFM probes inside the SEM has been demonstrated experimentally. For the best knowledge of the authors, this work represents the first demonstration of the potential of deep learning for AFM localization inside an electron microscope.

Chapter 4

Model Predictive Control (MPC)-based Path Following and Obstacle Avoidance

This chapter presents a model predictive control (MPC)-based path following and obstacle avoidance at pre-defined velocity profile under the supervision of Scanning Electron Microscopy (SEM) for the AFM based nano-robotic system. This is the first time that MPC is implemented in micro/nano-robotic systems for autonomous control. The novelty of this work includes two aspects. First, a velocity-direction-amplitude-frequency map with input limitations is identified and introduced as a part of the kinematic model for MPC. Secondly, the algorithm is designed so that it allows controlling the AFM probe to follow a reference path with a specified longitudinal velocity and to avoid obstacles simultaneously, taking into account input safety constrains. As in the previous chapter, the AFM probe is localized across the visual tracking from SEM. A multi-phase optimization is formulated by Quadratic Programming to simultaneously optimize the sawtooth control signal directions, amplitudes and frequencies on both X and Y axes. A Frenet frame-based kinematic model combined with the identified PIA velocity map is designed and linearized. A cost function is defined to navigate the AFM probe with a specified velocity. Simulations and experiments are carried out and verify that, with the combination of Frenet kinematic model and the identified velocity map, the proposed algorithm is able to tune the inputs with safe constrains to drive the AFM probe across the reference path and to get around the obstacles simultaneously under the given velocity reference.

4.1 State of the art

Obstacle avoidance is a pivotal issue for autonomous robotics such as ground vehicles (AGVs) [77] [33], aerial vehicles [95] [151] and marine vehicles [144] [55]. According to literatures, there are mainly four categories of obstacle avoidance algorithms [77]: graph search-based methods [68], virtual potential and navigation function-based methods [87] [111], meta-heuristic-based methods [58], and mathematical optimization-based methods [165] [106].

Mathematical optimization-based methods are very popular in the field [77]. Model predictive control (MPC) is one of the most applied mathematical optimization approache. It performs an optimal computation online taking into account the robot states and the obstacle distribution information updated by sensors. An optimal control problem (OCP) is solved repeatedly over a receding finite horizon. Typically, optimal control problem (OCP) can be divided into nonlinear programming (NLP) and linear-quadratic programming (QP) [54]. A model predictive control requires an accurate kinematic or dynamic model of the system to predict its behavior in the future states.

Model predictive control scheme can be divided into several layers. In [54], the authors point out the concept of integrating collision avoidance functionality into the reference tracking, by dividing collision-free trajectory generation task into a high-level layer and a low-level control layer for stabilizing the vehicle, where MPC can be implemented for both layers, so as mentioned in [115]. A path planning and tracking framework is demonstrated in [60]. Potential field is constructed to generate a collision-free trajectory in high control layer. Path tracking control then follows the planned trajectory with Multi-constrained Model Predictive Control (MMPC), by regulating the steering angle to evade the dynamic obstacles. In [16], the authors propose a trajectory tracking strategy for unmanned aerial vehicles (UAV), using linear model predictive controller (MPC) in combination with non-linear state feedback. Instead of impractically applying direct control on UAV for evasive maneuvers, MPC works as part of trajectory tracker, only generating reference for the underlying state feedback.

In this thesis, considering the special working principle of PIA actuator, the moving direction of the end-effector is first determined in the high control layer. Afterwards, the sawtooth signal amplitudes and frequencies are optimized referring to the pre-decided motion direction. Path following and obstacle avoidance highly dependent on the velocity control of the PIA actuator. Here we consider the low amplitude velocity map that has not been identified previously. Therefore, a low velocity characterization model (velocity map) is identified. It is further linearized and integrated into the model predictive control.

4.2 Velocity Characterization

Experiments in Chapter 2, Fig.2.13, have illustrated that the velocity of PIA actuator is dependent on the direction, the amplitude and the frequency of the driving sawtooth input voltage. Here, a velocity-direction-amplitude-frequency map of PIA actuator is characterized in a low velocity range, i.e. < 20 μm/s.

The experiments are repeated for sawtooth voltages with the following frequencies: $1Hz$, $3Hz$, $5Hz$, $7Hz$, $9Hz$, $11Hz$, $13Hz$, $15Hz$, $17Hz$, $19Hz$, $20Hz$. For each frequency, different amplitudes have been are applied, namely $20V$, $30V$, $35V$, $40V$, $60V$, $80V$, $90V$. For each operating point, the velocity is calculated based on the average velocity. Correspondingly, the low velocity map of X and Y axes are fitted by a polynomial interpolation. For instance, Fig. 4.1 shows the identified velocity-direction-amplitude-frequency map of Y axis. The max velocities are $17.23\mu m/s$ and $-22.96\mu m/s$ for forward and backward directions respectively.

In the sequel, the following notations will be used to define the velocities of X and Y axes:

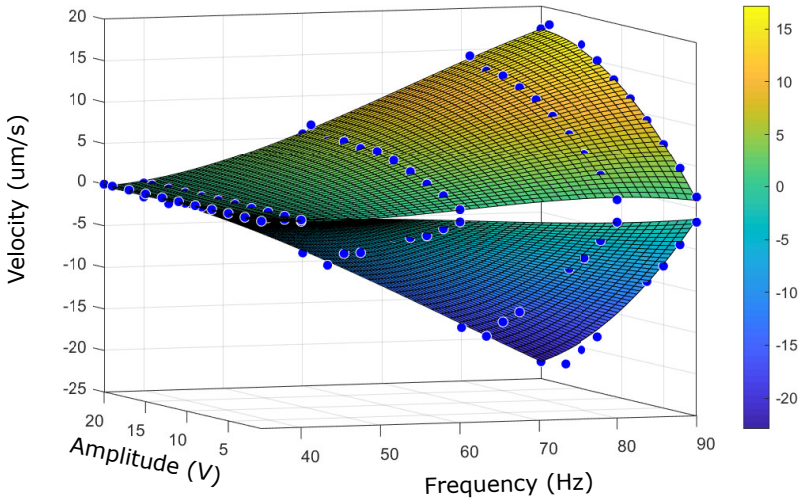

Figure 4.1: Identified velocity-direction-amplitude-frequency map of Y axis.

$$\begin{cases} v_x = f_x(dir_x, Amp_x, Fre_x) \Rightarrow \begin{cases} v_{x|forward} = f_{x|for}(Amp_x, Fre_x), \\ v_{x|backward} = f_{x|bac}(Amp_x, Fre_x) \end{cases} \\ v_y = f_y(dir_y, Amp_y, Fre_y) \Rightarrow \begin{cases} v_{y|forward} = f_{y|for}(Amp_y, Fre_y), \\ v_{y|backward} = f_{y|bac}(Amp_y, Fre_y) \end{cases} \end{cases} \tag{4.1}$$

where, dir_x, Amp_x, Fre_x, dir_y, Amp_y and Fre_y represent the direction, amplitude and frequency of X and Y axes. Associated with the input constrains, amplitude within 0-90V and frequency within 1-20Hz, the velocity mapping is exploited for the future states estimation and control optimization of MPC algorithm.

4.3 Kinematic model considering the velocity map

The ISIR-robotex platform is modeled as a holonomic system driven by PIA actuator, Fig. 4.2. Here, the kinematic frames are the same as those described in Chapter 3. The kinematic model of the ISIR-robotex platform is given by:

$$\begin{cases} \dot{P}_x(t) = v_x(t), \\ \dot{P}_y(t) = v_y(t), \end{cases} \tag{4.2}$$

where $P_x(t)$ and $P_y(t)$ stand for the AFM probe coordinates in the world frame, $v_x(t)$ and $v_y(t)$ represent the AFM probe velocities along X and Y axes. The equation 4.2 can be written in discrete format as follows:

$$\begin{cases} P_{x|k+1} = P_{x|k} + v_{x|k} T_{horizon}, \\ P_{y|k+1} = P_{y|k} + v_{y|k} T_{horizon}, \end{cases} \tag{4.3}$$

where $T_{horizon}$ is the MPC time interval,

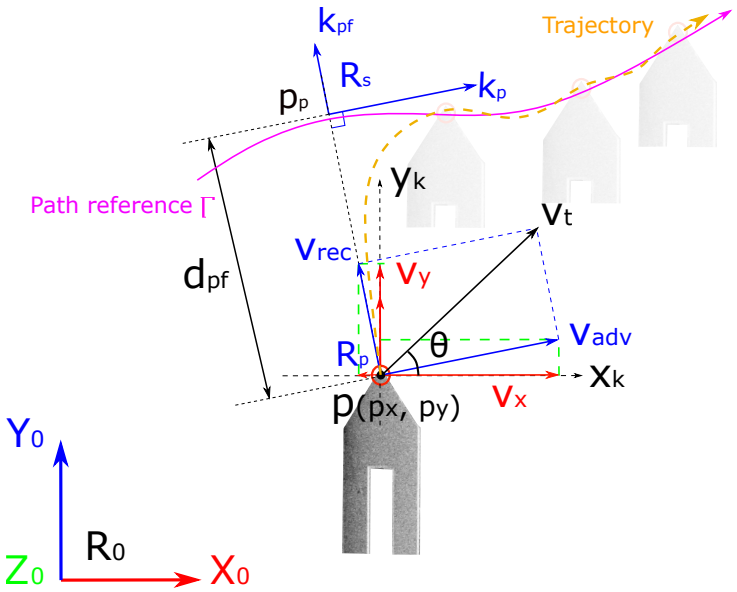

Figure 4.2: Kinemetic model with Frenet frame for path following

In order to use MPC for PIA actuators control, one can integrate the velocity map model of equation 4.1, into the kinematic model:

$$\begin{cases} \dot{P_{x|k}} = f_x(dir_{x|k}, Amp_{x|k}, Fre_{x|k}), \\ \dot{P_{y|k}} = f_y(dir_{y|k}, Amp_{y|k}, Fre_{y|k}), \end{cases} \tag{4.4}$$

For simplification, only the amplitude and the frequency are considered. They can be rewritten as $\dot{P_{h|k}} = f_h(Amp_{h|k}, Fre_{h|k})$ $(h = x \ or \ y)$.

This velocity relation is linearized in Taylor series and the future state of the velocity at $k+1$ can be iteratively determined as follows:

$$\begin{cases} v_{x|k+1} = v_{x|k} + \frac{\partial f_x}{\partial Amp_{x|k}} \Delta Amp_{x|k} + \frac{\partial f_x}{\partial Fre_{x|k}} \Delta Fre_{x|k}, \\ v_{y|k+1} = v_{y|k} + \frac{\partial f_y}{\partial Amp_{y|k}} \Delta Amp_{y|k} + \frac{\partial f_y}{\partial Fre_{y|k}} \Delta Fre_{y|k}, \end{cases} \tag{4.5}$$

Therefore, the amplitude increment $\Delta Amp_{h|k}$ and frequency increment $\Delta Fre_{h|k}$ of the saw-tooth voltages are the control variables of the MPC algorithm.

4.4 MPC algorithm

Typical MPC issue is presented in a linear format. After linearization, equation 4.3 and equation 4.5 can be rewritten as:

$$\begin{cases} X_{k+1} = AX_k + B_kU_k, \\ Y_k = CX_k, \end{cases} \tag{4.6}$$

where X_k and X_{k+1} represent the system current state and the future state, U_k is the control input, Y_k is the system output. X_k, Y_k and U_k are given as:

$$\begin{cases} X_k = [P_{x|k},\ P_{y|k},\ v_{x|k},\ v_{y|k},\ Amp_{x|k},\ Fre_{x|k}, Amp_{y|k},\ Fre_{y|k}]^T \\ Y_k = [P_{x|k},\ P_{y|k},\ v_{x|k},\ v_{y|k}]^T, \\ U_k = [\Delta Amp_{x|k},\ \Delta Fre_{x|k},\ \Delta Amp_{y|k},\ \Delta Fre_{y|k}]^T \end{cases} \tag{4.7}$$

where $P_{x|k}$ and $P_{y|k}$ are the coordinates of the point **P** in x and y axes respectively in the world frame. $v_{x|k}$ and $v_{y|k}$ are the velocities of the point **P** in x and y directions respectively in the world frame. $Amp_{x|k}$ and $Fre_{x|k}$ are the amplitude and the frequency of the sawtooth voltage applied to the PIA of the x axis at time k. $Amp_{y|k}$ and $Fre_{y|k}$ are the amplitude and the frequency of the sawtooth voltage applied to the PIA of the y axis at time k. $\Delta Amp_{x|k}$, $\Delta Fre_{x|k}$, $\Delta Amp_{y|k}$, $\Delta Fre_{y|k}$ are increment values of the corresponding variables between times k and k+1.

In equation 4.6:

$$A = \begin{bmatrix} 1\ 0 & T_{horizon}\ 0\ 0\ 0\ 0 \\ 0\ 1 & 0\ T_{horizon}\ 0\ 0\ 0 \\ 0_{6\times2} & I_{6\times6} \end{bmatrix},\ B_k = \begin{bmatrix} 0_{2\times4} \\ \frac{\partial f_x}{\partial Amp_{x|k}} \ \frac{\partial f_x}{\partial Fre_{x|k}}\ 0\ 0 \\ 0\ 0\ \frac{\partial f_y}{\partial Amp_{y|k}} \ \frac{\partial f_y}{\partial Fre_{y|k}} \\ I_{4\times4} \end{bmatrix},\ and\ C = \begin{bmatrix} I_{4\times4}\ 0_{4\times4} \end{bmatrix} \tag{4.8}$$

where, $0_{m\times n}$ and $I_{m\times n}$ are $m \times n$ zero matrix and identity matrix.

At each sampling time k, the MPC takes into account the process model of equation 4.6 and a sequence of optimized control inputs to predict the future behavior of the controlled system over a prediction horizon N using equation equation 4.9. Only the first element of U_k is taken into account. This process keeps repeating when the next sampling time arrives with the updated states measurements.

$$\bar{Y_k} = \bar{A_k}\bar{X_k} + \bar{B_k}\bar{U_k} \tag{4.9}$$

with

$$\bar{A_k} = \begin{bmatrix} CA \\ CA^2 \\ \vdots \\ CA^N \end{bmatrix}$$

$$\bar{B_k} = \begin{bmatrix} CB_k & 0 & ... & 0 \\ CAB_k & CB_{k+1} & ... & 0 \\ \vdots & \vdots & \ddots & \vdots \\ CA^{N-1}B_k & CA^{N-2}B_{k+1} & ... & CB_{k+N-1} \end{bmatrix}$$

$$\bar{Y_k} = \begin{bmatrix} Y_{k+1} \\ Y_{k+2} \\ ... \\ Y_{k+N-1} \\ Y_{k+N} \end{bmatrix}, \bar{X_k} = \begin{bmatrix} X_k \\ X_{k+1} \\ ... \\ X_{k+N-2} \\ X_{k+N-1} \end{bmatrix}, \bar{U_k} = \begin{bmatrix} U_k \\ U_{k+1} \\ ... \\ U_{k+N-2} \\ U_{k+N-1} \end{bmatrix} \tag{4.10}$$

where $\bar{Y_k}$ and $\bar{X_k}$ are the predicted system outputs and states in N horizons. The desired output state in N horizons is:

$$\bar{Y}_{desire|k} = \begin{bmatrix} Y_{desire|k+1} \\ Y_{desire|k+2} \\ ... \\ Y_{desire|k+N-1} \\ Y_{desire|k+N} \end{bmatrix}, \; Y_{desire|k+i} = \begin{bmatrix} P_{p_{x|k}} \\ P_{p_{y|k}} \\ v_{desire|k} \end{bmatrix} \tag{4.11}$$

where $i = (1...N)$. $P_{p_{x|k}}$ and $P_{p_{y|k}}$ are the coordinate of the projected point $\mathbf{P_p}$ at sampling k as shown in Fig.4.2. $v_{desire|k}$ is manually specified by the operator. This control process tunes the AFM Probe to track its projection $\mathbf{P_p}$ on curve Γ, with a specified velocity $v_{desire|k}$.

The objective of MPC is to optimize $\bar{U_k}$ to minimize a quadratic cost function of the form:

$$\bar{U_k^*} = arg \min_{\bar{U_k}} \sum_{i=1}^{N} \frac{1}{2} \underbrace{\|Y_{desire|k+i} - Y_{output|k+i}\|^2}_{Error_i} \tag{4.12}$$

where, $Y_{output|k+i} = [P_{x|k+i}, \; P_{y|k+i}, \; v_{P|k+i}]^T$ contains the system control states, including the AFM Probe position $(P_{x|k+i}, \; P_{y|k+i})$ and its advancing velocity $v_{P|k+i}$. Here, $v_{P|k+i} = ||(v_{x|k+i}, \; v_{y|k+i})^T||$.

$$Error_i = \underbrace{[\omega_1(P_{p_{x|k}} - P_{x|k+i})^2 + \omega_2(P_{p_{y|k}} - P_{y|k+i})^2]}_{distace\ error\ between\ AFMProbe\ and\ its\ projection P_p} + \underbrace{\omega_3(v_{desire|k} - v_{P|k+i})^2}_{velocity\ error} \tag{4.13}$$

where, ω_1, ω_2 and ω_3 are the weights of of each error item. The performance preference, e.g more accurate path following or more accurate velocity tracking, can be achieved by adding weighting matrix in the cost function:

$$\bar{weight}_k = \begin{bmatrix} weight_{k+1} & 0 & 0 & 0 & ... & ... & 0 & 0 \\ 0 & weight_{k+2} & 0 & 0 & ... & ... & 0 & 0 \\ ... & ... & ... & ... & ... & ... & ... & ... \\ ... & ... & ... & ... & ... & ... & ... & ... \\ 0 & 0 & ... & ... & 0 & 0 & weight_{k+N-1} & 0 \\ 0 & 0 & ... & ... & 0 & 0 & 0 & weight_{k+N} \end{bmatrix} \tag{4.14}$$

where

$$weight_{k+i} = \begin{bmatrix} \omega_1 & 0 & 0 \\ 0 & \omega_2 & 0 \\ 0 & 0 & \omega_2 \end{bmatrix} \quad i = (1...N) \tag{4.15}$$

Here, $\omega_1 = \omega_2 = 0.5$ and $\omega_3 = 1$.

Quadratic Programming (QP) is used to calculate the optimal $\bar{U}_k^*$.

4.5 Quadratic Programming

Quadratic programming (QP) solves quadratic objective functions with linear constraints. Here qpOASES is chosen as the QP solver. qpOASES is an open-source *C++* implementation of the recently proposed online active set strategy, which was inspired by important observations from the field of parametric quadratic programming (QP). It has several theoretical features that make it particularly suited for model predictive control (MPC) applications. Further numerical modifications have made qpOASES a reliable QP solver, even when tackling semi-definite, ill-posed or degenerated QP problems. Moreover, several interfaces to third-party software like Matlab, Simulink or dSPACE are provided to make qpOASES easy-to-use.

qpOASES finds a minimum for a QP problem formulated in the following stard form:

$$min\ \frac{1}{2}x'Hx + x'g \tag{4.16}$$

such that

$$\begin{cases} lb \leqslant x \leqslant ub, \\ lbA \leqslant A \cdot x \leqslant ubA, \end{cases} \tag{4.17}$$

where nV and nC take the number of variables and the number of constraints of the quadratic program sequence to be solved, $H \in R^{nV \times nV}$ denotes a (typically positive semi-definite) symmetric Hessian matrix and all other quantities match common notation, the gradient vector $g \in R^{nV}$, the constraint matrix $A \in R^{nC \times nV}$, the lower and upper bound vectors $lb, ub \in R^{nV}$, and the lower and upper constraints' bound vectors $lbA, ubA \in R^{nC}$. Equality constraints are imposed be setting the corresponding entries of lower and upper (constraints') bounds vectors to the same value. qpOASES also does a good job in detecting infeasible or unbounded QP problem formulations.

4.6 Constrains

One distinguished advantage of model predictive control is the consideration of the plant model restrictions and physical constrains between the plant and the environment. This enables MPC to be adaptable and preferred to various practical applications.

4.6.1 Constrains for input

The control input $\bar{U}_k^*$ from model predictive controller represents the increments of amplitude and frequency, which needs to be limited in order to achieve a smooth control on PIA actuator. As a result, the lower and upper constrain vectors of $\bar{U}_k^*$ during model predictive control are defined as:

$$lb_k = \begin{bmatrix} lbs_{k+1} \\ lbs_{k+2} \\ \cdots \\ \cdots \\ lbs_{k+N-1} \\ lbs_{k+N} \end{bmatrix} \; where, \; lbs_{k+i} = \begin{bmatrix} lb_{\Delta Amp_x|k+i} \\ lb_{\Delta Fre_x|k+i} \\ lb_{\Delta Amp_y|k+i} \\ lb_{\Delta Fre_y|k+i} \end{bmatrix}, \; i \in (1...N) \tag{4.18}$$

Here, $lb_{\Delta Amp_x|k+i} = -1V$, $lb_{\Delta Fre_x|k+i} = -5Hz$ are the lower amplitude and frequency increment bounds on X axis, $lb_{\Delta Amp_y|k+i} = -1V$, $lb_{\Delta Fre_y|k+i} = -5Hz$ are the lower amplitude and frequency increment bounds on Y axis.

$$ub_k = \begin{bmatrix} ubs_{k+1} \\ ubs_{k+2} \\ ... \\ ... \\ ubs_{k+N-1} \\ ubs_{k+N} \end{bmatrix} \; where, \; ubs_{k+i} = \begin{bmatrix} ub_{\Delta Amp_x|k+i} \\ ub_{\Delta Fre_x|k+i} \\ ub_{\Delta Amp_y|k+i} \\ ub_{\Delta Fre_y|k+i} \end{bmatrix}, \; i \in (1...N) \tag{4.19}$$

Here, $ub_{\Delta Amp_x|k+i} = 1V$, $ub_{\Delta Fre_x|k+i} = 5Hz$ are the upper amplitude and frequency increment bounds on X axis, $ub_{\Delta Amp_y|k+i} = 1V$, $ub_{\Delta Fre_y|k+i} = 5Hz$ are the upper amplitude and frequency increment bounds on Y axis.

4.6.2 Constraints for state

The identified velocity-amplitude-frequency map of PIA actuator (Fig. 4.1) provides the information of feasible control input range. In addition, obstacle avoidance requests that the distance between the AFM probe and the obstacle is higher than a safe value r_{safe}, Fig. 4.3. As a result, the lower and upper bound vectors of the states in N horizons are defined as:

$$\bar{lbAd}_k = \begin{bmatrix} lbAds_{k+1} \\ lbAds_{k+2} \\ ... \\ ... \\ lbAds_{k+N-1} \\ lbAds_{k+N} \end{bmatrix} \; where, \; lbAds_{k+i} = \begin{bmatrix} lbAd_{d|k+i} \\ lbAd_{Amp_x|k+i} \\ lbAd_{Fre_x|k+i} \\ lbAd_{Amp_y|k+i} \\ lbAd_{Fre_y|k+i} \end{bmatrix}, \; i \in (1...N) \tag{4.20}$$

Here, $lbAd_{d|k+i} = r_{safe}$ (Fig. 4.3) takes the minimum distance between the AFM probe and the obstacle, e.g. the obstacle radius. $lbAd_{Amp_x|k+i} = 34V$ and $lbAd_{Fre_x|k+i} = 5Hz$ are the lower sawtooth signal amplitude and frequency bound on X axis, $lbAd_{Amp_y|k+i} = 30V$ and $lbAd_{Fre_y|k+i} = 5Hz$ are the lower sawtooth signal amplitude and frequency bound on Y axis.

$$\bar{ubAd}_k = \begin{bmatrix} ubAds_{k+1} \\ ubAds_{k+2} \\ ... \\ ... \\ ubAds_{k+N-1} \\ ubAds_{k+N} \end{bmatrix} \; where, \; ubAds_{k+i} = \begin{bmatrix} ubAd_{d|k+i} \\ ubAd_{Amp_x|k+i} \\ ubAd_{Fre_x|k+i} \\ ubAd_{Amp_y|k+i} \\ ubAd_{Fre_y|k+i} \end{bmatrix}, \; i \in (1...N) \tag{4.21}$$

$ubAd_{d|k+i} = 100 \times d_{safe}$ means that there is no upper bound of distance between the AFM probe and the obstacle. $ubAd_{Amp_x|k+i} = 80V$ and $ubAd_{Fre_x|k+i} = 20Hz$ are the upper sawtooth

signal amplitude and frequency bound on X axis, $ubAd_{Amp_y|k+i} = 80V$ and $ubAd_{Fre_y|k+i} = 20Hz$ are the upper sawtooth signal amplitude and frequency bound on Y axis.

Therefore, the above five states need to be obtained to satisfy the constrains of equation 4.20-4.21.

$$lbAds_{k+i} < \begin{bmatrix} d_{k+i} \\ Amp_{x|k+i} \\ Fre_{x|k+i} \\ Amp_{y|k+i} \\ Fre_{y|k+i} \end{bmatrix} < ubAds_{k+i}, \quad i \in (1...N) \tag{4.22}$$

Where, d_{k+i} stands for the distance between the AFM probe and the obstacle. $Amp_{x|k+i}$ and $Fre_{x|k+i}$ represent the sawtooth signal amplitude and frequency applied on X axis. $Amp_{y|k+i}$ and $Fre_{y|k+i}$ represent the sawtooth signal amplitude and frequency applied on Y axis. $Amp_{x|k+i}$, $Fre_{x|k+i}$, $Amp_{y|k+i}$ and $Fre_{y|k+i}$ are updated by iteration.

$$\begin{cases} Amp_{x|k+i+1} = Amp_{x|k+i} + U_{k+i}(1), \\ Fre_{x|k+i+1} = Fre_{x|k+i} + U_{k+i}(2), \\ Amp_{y|k+i+1} = Amp_{y|k+i} + U_{k+i}(3), \\ Fre_{y|k+i+1} = Fre_{y|k+i} + U_{k+i}(4), \end{cases} \tag{4.23}$$

The obstacle avoidance behavior thanks to the constrain on the distance between the AFP tip and the obstacle, d_{k+i}, which keeps being larger than the safe distance r_{safe}. d_{k+i} is calculated as:

$$d_{k+i} = ||\overrightarrow{P_{k+i}\ c_{k+i}}|| = a_{k+i} \cdot (P_{k+i} - c_{k+i}), \quad i \in (1...N) \tag{4.24}$$

where, $P_{k+i} = (P_{x|k+i}, P_{y|k+i})$ is the AFM probe coordinate, $c_{k+i} = (c_{x|k+i}, c_{y|k+i})$ is the obstacle coordinate, $a_{k+i} = (id_{x|k+i}, id_{y|k+i})$ is the unit vector of $\overrightarrow{P_{k+i}\ c_{k+i}}$, given as:

$$(id_{x|k+i}, id_{y|k+i}) = \frac{1}{\sqrt{(P_{x|k+i} - c_{x|k+i})^2 + (P_{y|k+i} - c_{y|k+i})^2}} (P_{x|k+i} - c_{x|k+i},\ P_{y|k+i} - c_{y|k+i}) \tag{4.25}$$

Thus, in order to satisfy the distance and control variables constrains in equation 4.22, a new set of state vector of the system need to be considered.

$$\bar{Ys}_{d|k} = \underbrace{\begin{bmatrix} Cs_{d|k}A_k \\ Cs_{d|k}A_k^2 \\ ... \\ ... \\ Cs_{d|k}A_k^{N-1} \\ Cs_{d|k}A_k^N \end{bmatrix}}_{\bar{As}_{d|k}} \bar{X}_k + \underbrace{\begin{bmatrix} Cs_{d|k}B_k & 0 & ... & 0 & 0 \\ Cs_{d|k}A_kB_k & 0 & ... & 0 & 0 \\ ... & ... & ... & ... & ... \\ ... & ... & ... & ... & ... \\ Cs_{d|k}A_k^{N-2}B_k & Cs_{d|k}A_k^{N-3}B_k & ... & Cs_{d|k}B_k & 0 \\ Cs_{d|k}A_k^{N-1}B_k & Cs_{d|k}A_k^{N-2}B_k & ... & Cs_{d|k}A_kB_k & Cs_{d|k}B_k \end{bmatrix}}_{\bar{Bs}_{d|k}} \bar{U}_k \tag{4.26}$$

where

$$\bar{Ys}_{d|k} = \begin{bmatrix} Ys_{d|k+1} \\ Ys_{d|k+2} \\ ... \\ ... \\ Ys_{d|k+N-1} \\ Ys_{d|k+N} \end{bmatrix} \quad and \quad \bar{U}_k = \begin{bmatrix} u_k \\ u_{k+1} \\ ... \\ ... \\ u_{k+N-2} \\ u_{k+N-1} \end{bmatrix} \tag{4.27}$$

and

$$\underbrace{\begin{bmatrix} P_{x|k+i} \\ P_{y|k+i} \\ Amp_{x|k+i} \\ Fre_{x|k+i} \\ Amp_{y|k+i} \\ Fre_{y|k+i} \end{bmatrix}}_{Ys_{d|k+i}} = \underbrace{\begin{bmatrix} 1&0&0&0&0&0&0&0 \\ 0&1&0&0&0&0&0&0 \\ 0&0&0&0&1&0&0&0 \\ 0&0&0&0&0&1&0&0 \\ 0&0&0&0&0&0&1&0 \\ 0&0&0&0&0&0&0&1 \end{bmatrix}}_{Cs_{d|k+i}} \underbrace{\begin{bmatrix} P_{x|k+i} \\ P_{y|k+i} \\ v_{x|k+i} \\ v_{y|k+i} \\ Amp_{x|k+i} \\ Fre_{x|k+i} \\ Amp_{y|k+i} \\ Fre_{y|k+i} \end{bmatrix}}_{X_{k+i}}, \quad i \in (1...N) \tag{4.28}$$

where $\bar{Ys}_{d|k}$ is the concerned states under constrains in N horizons. Convert $P_{x|k+i}, P_{y|k+i}$ in $Ys_{d|k+i}$ onto distance estimation d_{k+i} by equation 4.24 and equation 4.25. Therefore,

$$\underbrace{\begin{bmatrix} Yc_{d|k+1} \\ Yc_{d|k+2} \\ ... \\ ... \\ Yc_{d|k+N-1} \\ Yc_{d|k+N} \end{bmatrix}}_{\bar{Yc_{d|k}}} = \underbrace{\begin{bmatrix} Cc_{d|k+1} & 0 & 0 & ... & 0 & 0 \\ 0 & Cc_{d|k+2} & 0 & ... & 0 & 0 \\ ... & ... & ... & ... & ... & ... \\ ... & ... & ... & ... & ... & ... \\ 0 & 0 & ... & ... & Cc_{d|k+N-1} & 0 \\ 0 & 0 & ... & ... & 0 & Cc_{d|k+N} \end{bmatrix}}_{\bar{Cc_{d|k}}} \left(\underbrace{\begin{bmatrix} Ys_{d|k+1} \\ Ys_{d|k+2} \\ ... \\ ... \\ Ys_{d|k+N-1} \\ Ys_{d|k+N} \end{bmatrix}}_{\bar{Ys_{d|k}}} - \underbrace{\begin{bmatrix} c_{k+1} \\ c_{k+2} \\ ... \\ ... \\ c_{k+N-1} \\ c_{k+N} \end{bmatrix}}_{\bar{c_k}} \right) \tag{4.29}$$

where

$$\underbrace{\begin{bmatrix} d_{k+i} \\ Amp_{x|k+i} \\ Fre_{x|k+i} \\ Amp_{y|k+i} \\ Fre_{y|k+i} \end{bmatrix}}_{Yc_{d|k+i}} = \underbrace{\begin{bmatrix} id_{x|k+i} & id_{y|k+i} & 0 & 0 & 0 & 0 \\ 0 & 0 & 1 & 0 & 0 & 0 \\ 0 & 0 & 0 & 1 & 0 & 0 \\ 0 & 0 & 0 & 0 & 1 & 0 \\ 0 & 0 & 0 & 0 & 0 & 1 \end{bmatrix}}_{Cc_{d|k+i}} \left(\underbrace{\begin{bmatrix} P_{x|k+i} \\ P_{y|k+i} \\ Amp_{x|k+i} \\ Fre_{x|k+i} \\ Amp_{y|k+i} \\ Fre_{y|k+i} \end{bmatrix}}_{Ys_{d|k+i}} - \underbrace{\begin{bmatrix} c_{x|k+i} \\ c_{y|k+i} \\ 0 \\ 0 \\ 0 \\ 0 \end{bmatrix}}_{c_{k+i}} \right), \quad i \in (1...N) \tag{4.30}$$

Eventually, $\bar{Yc_{d|k}}$ should satisfy the constrain bounds of equation 4.20 and equation 4.21:

$$\begin{cases} lb\bar{A}d_k \leqslant \bar{Yc_{d|k}} \leqslant ub\bar{A}d_k \\ \bar{Yc_{d|k}} = \bar{Cc_{d|k}} \cdot (\bar{As_{d|k}} \cdot \bar{X_k} + \bar{Bs_{d|k}} \cdot \bar{U_k} - \bar{c_k}) \end{cases} \tag{4.31}$$

which is further induced in the standard QP format as equation 4.17.

$$\begin{cases} A = \bar{Cc_{d|k}} \cdot \bar{Bs_{d|k}} \\ lbA = lb\bar{A}d_k + \bar{Cc_{d|k}} \cdot \bar{c_k} - \bar{As_{d|k}} \cdot \bar{X_k} \\ ubA = ub\bar{A}d_k + \bar{Cc_{d|k}} \cdot \bar{c_k} - \bar{As_{d|k}} \cdot \bar{X_k} \end{cases} \tag{4.32}$$

With the constrains of equation 4.18, equation 4.19 and equation 4.32, the nano-robotic system is able to drive the AFM probe with a smooth trajectory and simultaneously avoid unexpected collisions with the obstacles.

4.7 Obstacle avoidance control scheme

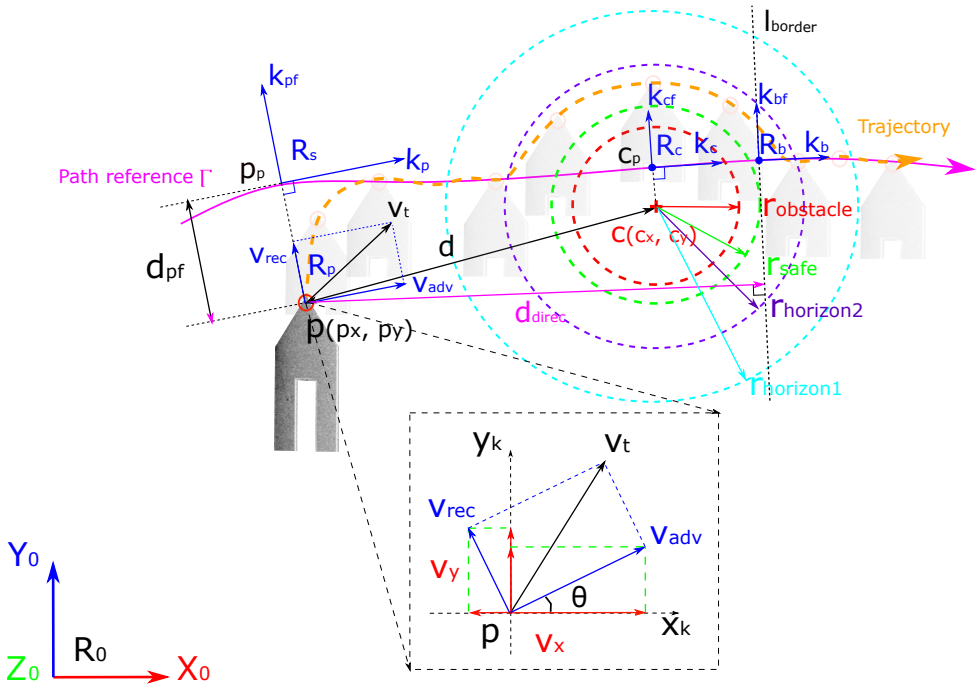

Figure 4.3: Kinematic model for model predictive control obstacle avoidance

Fig. 4.3 illustrates the Kinematic model during obstacle avoidance. $P(P_x, P_y)$ stands for the AFM probe coordinates from SEM vision. P_p is the closest point, projected from AFM probe $P(P_x, P_y)$ onto the reference curve Γ. R_s is the Frenet frame at P_p, with k_{pf} and k_p are the perpendicular and tangential unit vectors on curve Γ. $c(c_x, c_y)$ is the obstacle coordinate. c_p is the closest point, by projecting $c(c_x, c_y)$ onto Γ. R_c is the Frenet frame at c_p, with k_{cf} and k_c are the perpendicular and tangential unit vectors of the curve Γ. Line l_{border} is the tangent to the obstacle parallel with k_{cf}. It is treated as the terminating border of the obstacle, after which the bypassing behavior is completed. The intersection between l_{border} and Γ is at b_p, where frame R_b locates, parallel with frame R_c. Here, a virtual obstacle is defined with a radius of $r_{obstacle} = 18\ pixel$ and a safe zone radius of $r_{safe} = 20\ pixel$.

The obstacle avoidance control procedure is divided into three steps:

(1) When the AFM probe is far from the obstacle, only path following by MPC is implemented.

(2) When the AFM probe moves closer and enters the 'dangerous zone' around the obstacle, path following and obstacle avoidance controls are both applied thanks to MPC. The robot bypasses the obstacle and simultaneously keeps itself as close as possible to the specified path.

(3) After the AFM probe bypass the obstacle (passing by l_{border}), it will switch back to unique path following by MPC again.

4.7.1 Control scheme

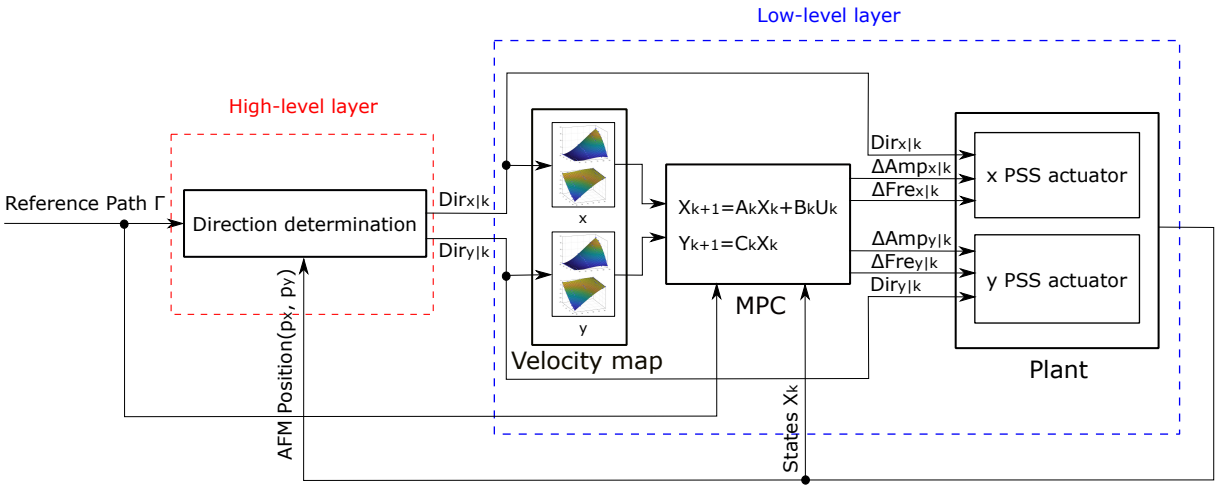

Figure 4.4: Model predictive control (MPC)-based obstacle avoidance scheme. High-level layer determines the direction dependent velocity maps, according to AFM probe velocity projection on X and Y axes. Low-level layer referring to the specified velocity maps, optimizes the control input applying on the plant.

In this work, a model predictive control method is proposed considering the special direction dependent characteristic of PIA actuator. The obstacle avoidance control scheme is divided into two layers as shown in Fig. 4.4. The high-level layer projects the desired AFM probe velocity onto X and Y axes velocities. The directions decide the corresponding velocities maps to be used in equation 4.8. The low-level layer, according to the selected velocity maps, executes MPC to optimize $Amp_{x|k}$, $Fre_{x|k}$, $Amp_{y|k}$ and $Fre_{y|k}$.

Based on Fig. 4.3, the sawtooth signal directions definition in high-level layer, is summarized as follows:

$$\begin{cases} if\ d_{direc} \cdot k_b > 0, \begin{cases} if\ d_{k+i} > r_{horizon1}, \begin{cases} Direc_x = sign(k_{pf} \cdot i_x + k_p \cdot i_x) \\ Direc_y = sign(k_{pf} \cdot i_y + k_p \cdot i_y)) \end{cases} \\ if\ r_{horizon1} > d_{k+i}, \begin{cases} Direc_x = sign(k_{cf} \cdot i_x + k_c \cdot i_x) \\ Direc_y = sign(k_{cf} \cdot i_y + k_c \cdot i_y) \end{cases} \end{cases} \\ if\ d_{direc} \cdot k_b < 0, \begin{cases} Direc_x = sign(k_{pf} \cdot i_x + k_p \cdot i_x) \\ Direc_y = sign(k_{pf} \cdot i_y + k_p \cdot i_y) \end{cases} \end{cases} \tag{4.33}$$

where, $Direc_x$ and $Direc_y$ are the sawtooth signal directions on X and Y axes. d_{direc} is the vector from $P(P_x, P_y)$ to l_{border}. Moreover, $r_{horizon1}$ is the 'dangerous zone' radius, centered on the obstacle c. The process is explained as:

(1) When the AFM probe is before bypassing the obstacle ($d_{direc} \cdot k_b > 0$), and out of the

'dangerous zone' ($d_{k+i} > r_{horizon1}$, where $r_{horizon1} = 4 \times r_{obstacle}$), $Direc_x$ and $Direc_y$ depend on the relative locations between the AFM probe position $P(P_x, P_y)$ and the closest point P_p.

(2) When the AFM probe enters the 'dangerous zone' ($d_{k+i} < r_{horizon1}$) and before bypasses the obstacle ($d_{direc} \cdot k_b > 0$), $Direc_x$ and $Direc_y$ are only defined by corresponding locations of the obstacle location $c(c_x, c_y)$ and the curve Γ.

(3) After the AFM probe bypasses the obstacle ($d_{direc} \cdot k_b < 0$), it converts back to path following mode and $Direc_x$ and $Direc_y$ are determined the same as step (1).

4.7.2 Time horizon adaptation during obstacle avoidance

To achieve both path following and obstacle avoidance, a location-varying time horizon interval is applied. This is because during obstacle avoidance, a longer time horizon interval is needed to pre-view a further interaction between the AFM probe and the obstacle. The time horizon is defined as:

$$\begin{cases} if\ d_{direc} \cdot k_b > 0, \begin{cases} if\ d_{k+i} > r_{horizon1},\ T_{horizon} = T_{horizon}^{min} \\ if\ r_{horizon1} > d_{k+i} > r_{horizon2},\ T_{horizon} = \frac{(T_{horizon}^{max} - T_{horizon}^{min})}{r_{horizon1} - r_{horizon2}}(d - r_{horizon2}) \\ if\ d_{k+i} < r_{horizon2},\ T_{horizon} = T_{horizon}^{max} \end{cases} \\ if\ d_{direc} \cdot k_b < 0,\ T_{horizon} = T_{horizon}^{min} \end{cases} \tag{4.34}$$

(1) When the AFM probe is before bypassing the obstacle ($d_{direc} \cdot k_b > 0$) and out of the 'dangerous zone' ($d_{k+i} > r_{horizon1}$, where $r_{horizon1} = 4 \times r_{obstacle}$), a short $T_{horizon} = T_{horizon}^{min} = 2s$ is implemented. This is because a long $T_{horizon}$ will generate an excessive far position prediction, leading to no solution by qpOASES solver.

(2) When the AFM probe enters the 'dangerous zone' ($d_{k+i} < r_{horizon1}$) and before bypasses the obstacle ($d_{direc} \cdot k_b > 0$), it continuously lengthens the horizon time, in order to 'see' the future collision possibility, and have enough response time to take an avoiding act in advance. The horizon time, starts from $T_{horizon} = T_{horizon}^{min}$ increases inverse-proportionally with the distance between the AFM probe and the obstacle, d_{k+i}, until a threshold value of $T_{horizon} = T_{horizon}^{max} = 8s$ after $d < r_{horizon2}$.

(3) After the AFM probe bypass the obstacle ($d_{direc} \cdot k_b < 0$), it converts back to path following mode and the short $T_{horizon} = T_{horizon}^{min}$ is applied again to track the following path.

4.8 Experiment

The experimental setup is the same as the one used for path following. The experiments are implemented focusing on two performances. The first part concerns the path following with the specified longitudinal velocity. The second part tests the new control method's capability for

obstacle avoidance. During the experiments, the AFM probe position feedback is provided by Template Matching from SEM vision. QPOASES is used as the quadratic programming solver for the model predictive control optimization. It can be directly integrated in Simulink and dSPACE for a real-time control. The control parameters are summarized in TABLE 4.1.

During the experiments, the velocity feedback of X and Y axes are given as an average velocity format:

$$\begin{cases} v_{x|kT_s} = \frac{P_{x|kT_s} - P_{x|(kT_s - nT_s)}}{\Delta t}, \\ v_{y|kT_s} = \frac{P_{y|kT_s} - P_{y|(kT_s - nT_s)}}{\Delta t}, \end{cases} \tag{4.35}$$

where,

$P_{x|kT_s}$ and $P_{y|kT_s}$ are the coordinated of the AFM probe at time kT_s.

$\Delta t = nT_s$ is the time duration of the average velocity calculation, which is assigned as 5 s.

$F_s = 1/T_s = 50Hz$ is the sampling frequency of the system.

Variable	Value	Refering
F_s (Sampling frequency)	50 Hz	
v_{desire}	$3\mu m/s$	equation 4.11
ω_1	0.5	equation 4.15
ω_2	0.5	equation 4.15
ω_3	1	equation 4.15
$T_{horizon}^{min}$	2 s	equation 4.34
$T_{horizon}^{max}$	8 s	equation 4.34
$obstacle_{radius}$	18 $pixels$	Fig. 4.3
$safe_{radius}$	20 $pixels$	Fig. 4.3
$r_{horizon1}$	$4 \times obstacle_{radius}$	equation 4.33
$r_{horizon2}$	$2 \times obstacle_{radius}$	equation 4.33
$lbAd_d$	20 $pixel$	equation 4.20
$ubAd_{Amp_x}$	80 V	equation 4.21
$lbAd_{Amp_x}$	34 V	equation 4.20
$ubAd_{Fre_x}$	20 Hz	equation 4.21
$lbAd_{Fre_x}$	5 Hz	equation 4.20
$ubAd_{Amp_y}$	80 V	equation 4.21
$lbAd_{Amp_y}$	30 V	equation 4.20
$ubAd_{Fre_y}$	20 Hz	equation 4.21
$lbAd_{Fre_y}$	5 Hz	equation 4.20
$ub_{\Delta Amp_x}$	1 V	equation 4.19
$lb_{\Delta Amp_x}$	-1 V	equation 4.18
$ub_{\Delta Fre_x}$	5 Hz	equation 4.19
$lb_{\Delta Fre_x}$	-5 Hz	equation 4.18
$ub_{\Delta Amp_y}$	1 V	equation 4.19
$lb_{\Delta Amp_y}$	-1 V	equation 4.18
$ub_{\Delta Fre_y}$	5 Hz	equation 4.19
$lb_{\Delta Fre_y}$	-5 Hz	equation 4.18

Table 4.1: Parameter list of model predictive control for path following and obstacle avoidance

4.8.1 Path following by model predictive control

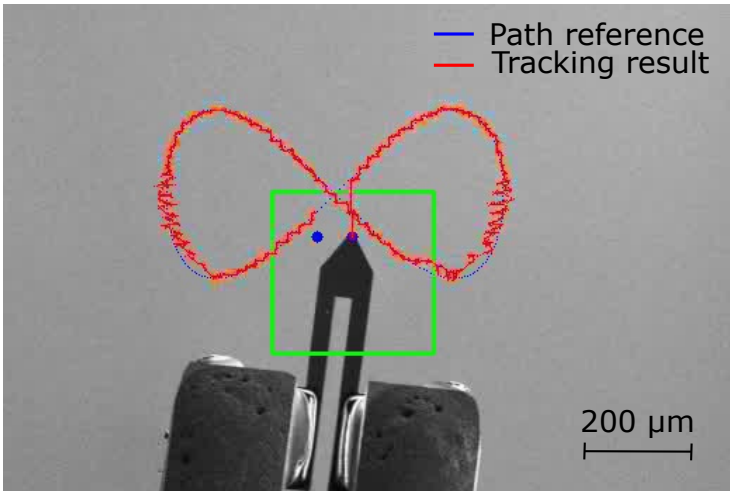

Figure 4.5: Eight-shape reference path following with specified tangential velocity, through the proposed model predictive control. The blue curve represents the reference path, and the red curve is the tracking result.

An eight-shape curve is designated as the reference path, which is characterized with varying curvatures and different motion directions in order to comprehensively and representatively test the tracking performance of the proposed algorithm. The aim of this experiment is to control the AFM probe to track the defined path with a specified tangential velocity.

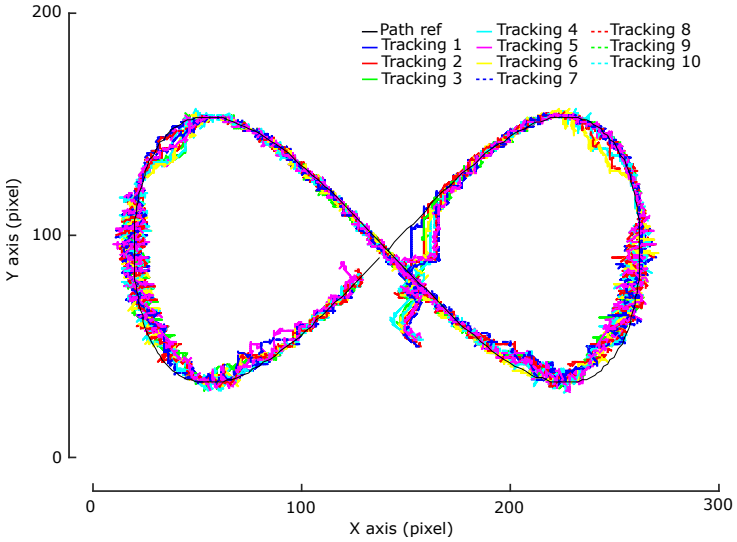

Figure 4.6: Tracking repeatability verification. From the same initial location, tune the AFM probe to follow the eight-shape reference path with specified tangential velocity for 10 trials.

The tracking result under the proposed model predictive control is presented in Fig. 4.5. It can be found that the proposed algorithm is able to tune the AFM probe to track the defined reference path with various curvatures in various directions. Tracking repeatability is carried out

and proved by applying path following control on the AFM probe from the same initial location for 10 trials, as shown in Fig. 4.6. The AFM probe performs better when tracking the partial path with less curvature, and shortcuts more when it meets sharp turns. In addition, it vibrates more when moving on Y axis direction compared with X axis direction.

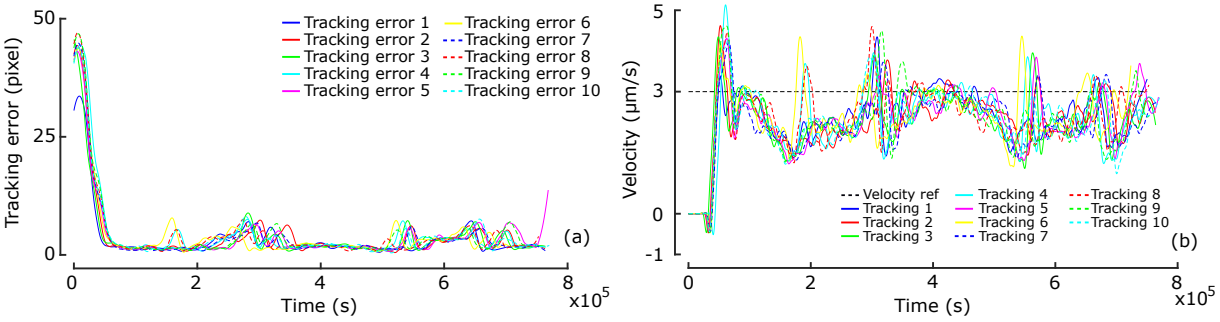

Figure 4.7: MPC obstacle avoidance experiment result. (a) The position tracking error. (b) The velocity tracking result. All the experiments are implemented for 10 trials.

Fig. 4.7 presents the position tracking error result (Fig. 4.7 (a)) and the velocity tracking result (Fig. 4.7 (b)), respectively. The position tracking error curve of Fig. 4.7 (a) illustrates the consistent convergences of the AFM probe to the eight-shape curve. There are fluctuations of the position tracking error curve because of the vibrations during the motion on Y axis direction and sharp turns. On the other hand, the velocity control result of Fig. 4.7 (b) shows that the actual AFM probe velocity fluctuates around the desired velocity, i.e. 3 $\mu m/s$. It decreases at the sharp turns.

Furthermore, based on the 10 trials data, the position tracking performance are evaluated by the mean tracking error, the Root Mean Square Error (RMSE) and the Standard deviation (STD).

The mean tracking error $\bar{x}$ is calculated as:

$$\bar{x} = \frac{1}{N}\sum_{i=1}^{N} x_i, \quad i \in (1...N) \tag{4.36}$$

where x_i represents the tracking error sample, N is the number of error samples.

The Root-Mean-Square Error (RMSE) is calculated as:

$$RMSE = \sqrt{\frac{1}{N}\sum_{i=1}^{N} {x_i}^2}, \quad i \in (1...N) \tag{4.37}$$

The Standard deviation (STD) is calculated as:

$$STD = \sqrt{\frac{1}{N}\sum_{i=1}^{N} (x_i - \bar{x})^2}, \quad i \in (1...N) \tag{4.38}$$

The analysis results are summarized in TABLE 4.2.

	Mean	RMSE	STD
Value	2.5193 *Pixel*	3.2452 *Pixel*	2.0447 *Pixel*

Table 4.2: MPC eight-shape path following tracking performance

The mean tracking error is 2.5 pixels, within an image sized of 610 × 460 pixels, which is considered acceptable. The RSME shows a slight bigger difference between the desired and the actual tracking trajectory, with 3.2 pixels. The STD of 2.0 pixels demonstrates the achievement of a stable tracking process.

These results illustrate that the proposed model predictive control is able to achieve an accurate and stable path following of the AFM probe, with a specified velocity profile, under the consideration of the special case of PIA actuator working principle.

4.8.2 Obstacle avoidance by model predictive control

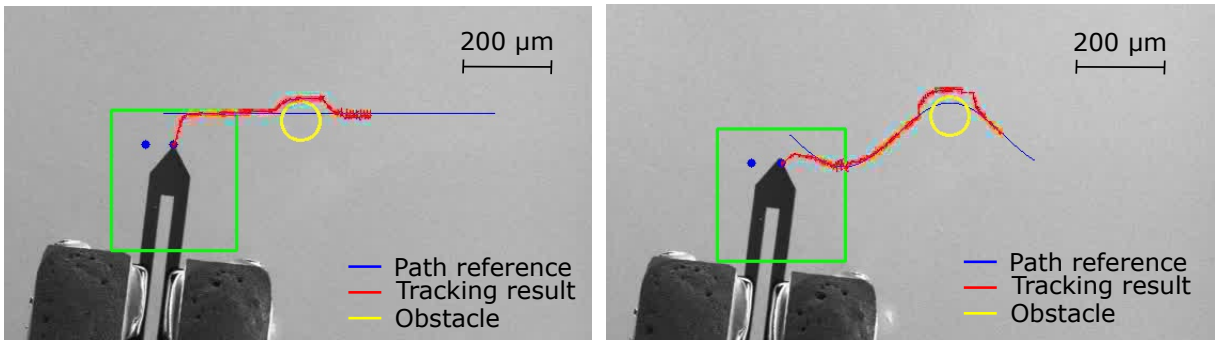

(a) (b)

Figure 4.8: Obstacle avoidance experiment results under the proposed model predictive control. The obstacle is featured with a radius of 18 pixels and a safe radius of 20 pixels.(a) Tracking result by given a straight line shape reference path. (b) Tracking result by given a sinusoidal shape reference path.

Furthermore, experiments of obstacle avoidance are executed under the proposed model predictive control method. A reference path is given, with a virtual obstacle obstructing the planned path. The aim is to control the AFM probe to follow the reference path and to simultaneously bypass the unexpected obstacle. The tracking result is shown in Fig. 4.8. A straight line shape reference path and a sinusoidal shape reference path are shown in Fig. 4.8 (a) and Fig. 4.8 (b). The results show that, with the proposed control algorithm, the AFM probe succeeds to first converge and follow the pre-defined path and then bypass the obstacle at the same time.

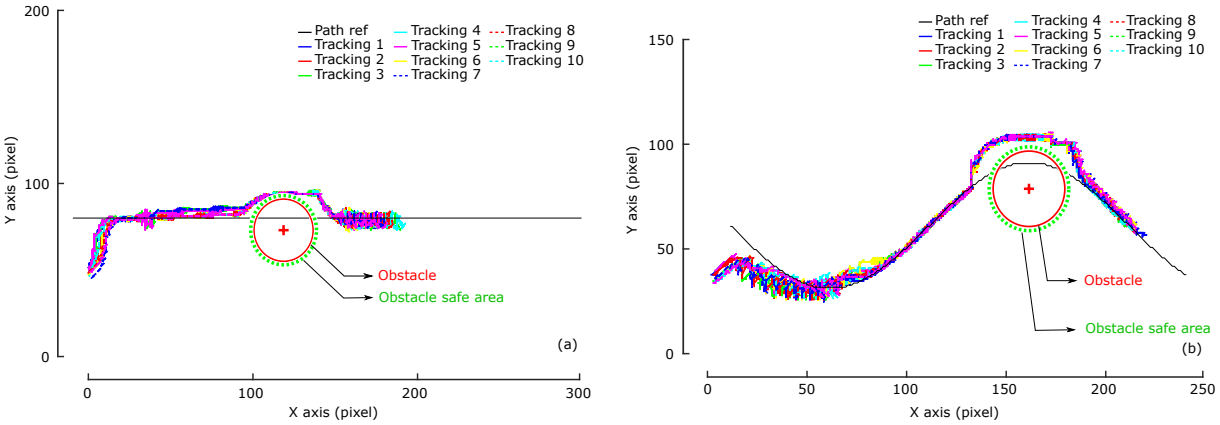

Figure 4.9: Obstacle avoidance repeatability experiment results. (a) 10 trails of obstacle avoidance control given with line reference path. (b) 10 trails of obstacle avoidance control given with sinusoidal reference path.

To prove the repeatability, 10 trails of both line shape and sinusoidal shape reference paths following are maneuvered separately as shown in Fig. 4.9. The obstacle is featured with a radius of 18 pixels and a circle with a radius of 20 pixels is regarded as safe area. Fig. 4.9 demonstrates that the obstacle avoidance behavior under the proposed model predictive control is experimentally repeatable. The AFM probe follows the pre-defined path first, then bypass the obstacle and keeps being as close as possible to the specified path, to achieve the shortest trajectory.

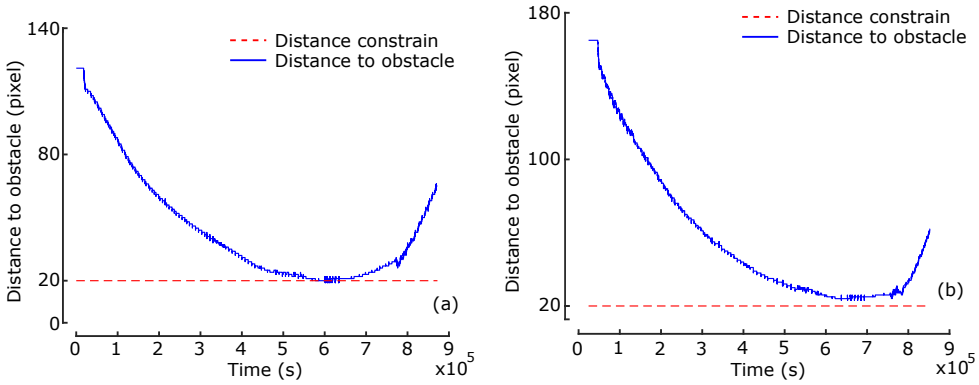

Figure 4.10: Distance distribution between the AFM probe and the obstacle, during the obstacle avoidance process. (a) Distance evolvement given with line reference curve. (b) Distance evolvement given with sinusoidal reference curve.

Fig. 4.10 shows the distance evolution between the AFM probe and the obstacle with respect to the obstacle avoidance procedure under the constrains of the proposed model predictive control. It forces the distance between the AFM probe and the obstacle to be bigger than the safe radius of 20 pixels. The results present that, given with both line and sinusoidal reference path, the proposed algorithm successfully controls the AFM probe to bypass the obstacle and maintains the AFM probe outside a safe radius of 20 pixels, away from the obstacle.

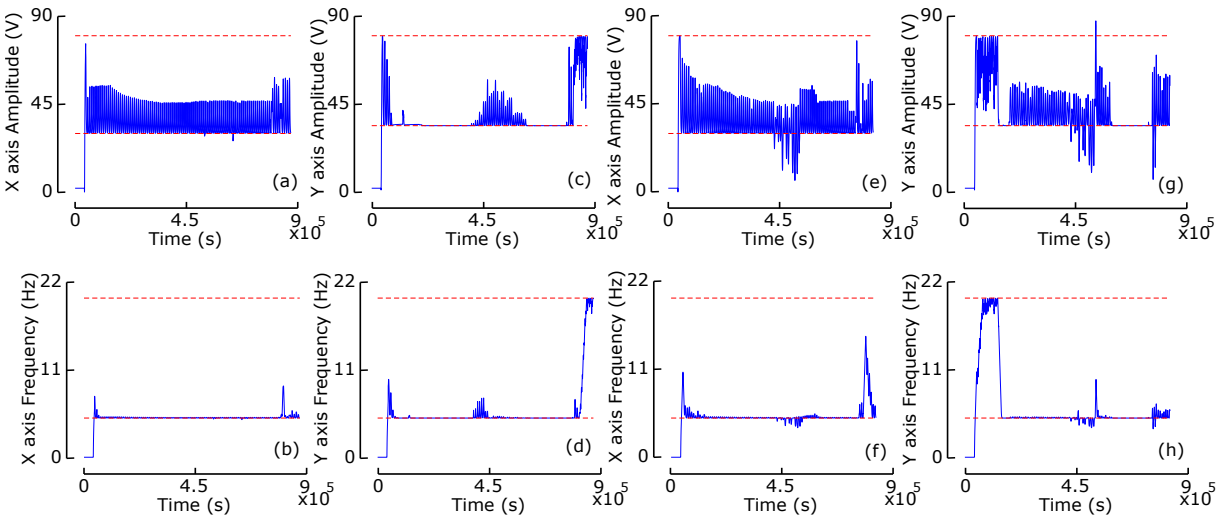

Figure 4.11: PIA actuator sawtooth signal inputs distribution during obstacle avoidance. (1) Obstacle avoidance given with line reference, (a)-(d), are $Amp_{x|k}$ within $34V \sim 80V$, $Fre_{x|k}$ within $5Hz \sim 20Hz$, $Amp_{y|k}$ within $30V \sim 80V$ and $Fre_{y|k}$ within $5Hz \sim 20Hz$. (2) Obstacle avoidance given with sinusoidal reference, (e)-(h) are $Amp_{x|k}$ within $34V \sim 80V$, $Fre_{x|k}$ within $5Hz \sim 20Hz$, $Amp_{y|k}$ within $30V \sim 80V$ and $Fre_{y|k}$ within $5Hz \sim 20Hz$.

Fig. 4.11 presents the PIA actuator sawtooth signal inputs. The amplitudes and the frequencies of X and Y axes ($Amp_{x|k}$, $Fre_{x|k}$, $Amp_{y|k}$ and $Fre_{y|k}$ in equation 4.7) are constrained by the proposed model predictive control method, as summarized in TABLE 4.1. All the concerning parameters are mainly within the constrain ranges, which guarantees the working range of the velocity from characterization map of Section 4.2.

To sum up, the experimental results show that, under the proposed model predictive control, which considers the working principle and velocity characterization of the PIA actuator, the AFM probe succeeds to follow the reference path with a pre-defined velocity, and simultaneously is capable of avoiding the obstacle obstructing the path.

4.9 Summary

This chapter for the first time achieves path following and obstacle avoidance simultaneously by model predictive control on an AFM driven by Piezoelectric Stick-Slip inertial actuator (PIA actuator). The work is implemented under the visual tracking from SEM. Low velocity performance of PIA actuator is characterized by model identifications of velocity-direction-amplitude-frequency map (velocity map) of PIA actuator. The velocity map combined with the AFM based nano-robotic system kinematic model, is linearized to represent the plant. A model predictive control process is built according to the linearized plant model to optimize control inputs during obstacle avoidance. A two-layer obstacle avoidance control scheme is proposed considering the direction dependent feature of PIA actuator. The high-level layer determines the motion directions of X and Y axes, which is used to select the corresponding velocity map for MPC control. The low-level layer, in accordance with the selected velocity map and the nano-robotic kinematics, optimize the increment of the sawtooth input voltage amplitude and frequency to achieve

the obstacle avoidance task. Experiments are performed for both path following and obstacle avoidance control. The repeatability and the control effectiveness are verified experimentally with the AFM based nano-robotic system.

Conclusion and perspectives

Nano-robotic combined with scanning electron microscopy has become an excellent tool to deal with challenging and tricky micro/nano-technologies for both industry and academic research. Its extensive applications in various domains, including material characterization, nano-assembly and medical investigation, show the great commercial potentials, which requests to highly automated, standard and batching production capabilities. However, the start of the art shows that nano-robotic systems are most of the time operated based on either tele-operation with skilled-users or automated with task-oriented constraints. This greatly reduces the usability of such a technology for people outside the robotics filed. On the other hand, the advanced motion control and learning based techniques in macro scale robotics are still hard to directly apply in the small scales because of the special working principle of nano-robots, the complex physics and the limited sensing modules in the small world. As such, the objective of this thesis is the development of a generic, intelligent and user friendly interface that can manage elementary robotic tasks needed inside a SEM by simply defining graphical instructions on the SEM screen. To deal with the very high magnification capability of SEM and to be able to reach any region of interest on sample observed by a SEM, the robot end effectors must have the capability to navigate with a displacement range to resolution ratio of several million times. As such, all the motion control considered in this thesis must deal with *multi-scale trajectories*, i.e. trajectories in the nano-meter range up to the milliliter range. In this case, the piezoelectric inertial actuator (PIA) such as the Piezoelectric Stick Slip (PSS) actuator is the most promising type of actuator for such robots.

The main experimental platform considered in this thesis is the ISIR-robotex nano-robotic platform. The latter is mainly composed of a poly-articulated nano-robotic system actuated by PSS actuators and holding a self sensing AFM probe as end effector. This robot operates inside a SEM. The thesis tackles two control level issues. The high level control layer and the low level control layer. The high level control layer is in charge of decision making, such as motion planning, trajectory tracking and task distribution. It optimizes the decisions and assigns reference commands to the low level control layer according to multi-channel sensing fusion information. The low level control layer is focused on fundamental dynamics control such as position control, velocity control and force control.

For the low level control, this thesis deals with position and velocity control of PSS actuators. Even though there are a series of nano-robotic systems having been developed as commercial products or prototypes in the labs, the integrated controllers greatly limits the potential of use of such nano-robotic system. This is due to the lack of knowledge about the dynamics of the actuator. Therefore, this thesis first establishes a comprehensive and systematic modeling of a class of PSS actuator including the dynamic and the hysteresis modeling of the piezoelectric element actuator and the modeling of the friction. A multi-states pattern is proposed and applied in the dynamic modelings of the friction presliding phenomenon, resulting in a consistent simulations with the corresponding experimental data, in both time and frequency domains. Furthermore, the friction properties are identified and discovered to be dependent on the specific direction, amplitude and frequency of the sawtooth driving signal. Consequently, a fully-constructed modeling of the piezoelectric stick-slip actuator is presented. This model illustrates high matching with the experimental data for multi-scale displacement. This model can be used for observation purposes and for a fast pre-development of control strategies, upstream of a real time implementation.

For the velocity control of PSS actuators, the velocity characterization is first identified, with

respect to the amplitude and frequency of the sawtooth driving signal, in both the forward and backward directions under air and vacuum environments. The achievable velocity ranges of the PSS actuators have then been identified to be used as input references for the closed loop control. A double-proportional-integral control structure is proposed, in order to tune the amplitude and frequency of the sawtooth driving signal respectively. The instant and the average velocity feedback structures are compared in the control loop. The average velocity feedback with less pulse caused by the slip-phase achieves more stable performance. The success of velocity control enables the ISIR-robotex platform to achieve a smooth and stable motion when trajectory tracking is needed.

The well developed low level controls in this thesis settles the solid foundation to support the high level control to take a further step towards new approaches for automated nano-robotics based on inertial actuators inside electron microscopes.

For the high level control of the ISIR-robotex platform, path following control is first developed thanks to the accomplishment of velocity control. The inspiration comes from the path following control strategy of holonomic robotics in macro scale. Under the geometric based Frenet kinematic frame, an intuitive and effective path following algorithm is carried out to calculate the longitudinal and the perpendicular velocities which drive the robot to move along and converge to the reference path. These velocities are further projected onto X and Y axes and are tracked by the low level velocity controllers. Template matching algorithm is applied for the localization of the AFM probe and to provide the sensing feedback from the SEM image. The developed path following technique enriches the motion capability of the inertial based nano-robotic systems, that can be utilized for complicated trajectory tracking for manipulation and assembly missions. Other than this, it is a generic control method and can be adapted in sundry applications.

For AFM tracking using SEM vision, one has to consider specific issues related to the compromise between the scan speed and the image quality of SEM. This restriction seriously limits the performance of conventional vision tracking algorithms such that those based on Template Matching when used with electron images. At high scan speed, the image quality is very noisy making very difficult to differentiate the AFM tip from the background, hence limiting the tracking capabilities. In this thesis, we have explored for the first time the potential value of deep learning in the context of nano-robotic vision tracking inside SEM. A deep learning based Convolutional Neural Networks is proposed to provide a real-time AFM probe localization as position feedback in the control loop. A databased of scanning electron microscopy imaging is built, which consists of the marked coordinate of the AFM probe with different magnifications and evenly distributed locations. Compared with traditional vision tracking methods, the proposed learning network is able to extract the essential feature of the AFM probe and provide a robust prediction agaist the imaging background complexity and noise caused by the increasing SEM scanning speeds. The proposed learning network for the first time verify the possibility of importing machine learning into nano-robotic domain.

After the achievement of path following, another high level control is developed, obstacle avoidance. Model predictive control is implemented to drive the AFM probe to track the predefined path and keep the minimum distance between the AFM probe and the obstacle. The velocity-direction-amplitude-frequency map is identified, linearized and integrated as part of the model predictive control structure. A piezoelectric stick-slip actuator customized model predictive control algorithm is proposed for the path following control. A varying time horizon interval

strategy is imposed to guarantee the best performances in tracking the path and bypassing the obstacle. Constrains are added to drive the ISIR-robotex platform with safe input values. This thesis is a pioneer in model predictive control on robots based on piezoelectric inertial driving principle, which has not been reported in the literature. The proposed algorithm is able to facilitate the ISIR-robotex platform to track reference paths with position and velocity controls simultaneously. The obstacle avoidance control increase the intelligence of the nano-robotic system, which is more flexible and adaptable to deal with accidents during a manipulation task and continue to accomplish the given task. This can be an interesting solution for collaborative nano-manipulation issues.

In order to achieve these automation control process efficiently, an intuitive and user-friendly interface between the operators and the ISIR-robotex platform is constructed. The reference path is easily specified just by a simple mouse click on the screen. Sensors, controllers and executors are linked by the built interface through real-time udp communication. This intuitive interface enables the challenging nano-manipulation issue to become a child-play. With such a simple operating rules, even people who have no pre-knowledge about nano-manipulation, is able to give a reasonable command without any hesitation.

To summary, this thesis develops a task-generic, automated nano-manipulation system under the vision feedback of scanning electron microscopy. The work involves a comprehensive improvement on the modeling, sensing, control and intelligence of nano-robotic. Velocity control, path following control and obstacle avoidance control are for the first time achieved in nano-robotic domain. Deep learning based Convolutional Neural Networks improves the visual tracking performance from scanning electron microscopy imaging, which has not been reported in the literature. The proposed algorithms and methods in this thesis are universal and can be adapted in wide ranges of tasks. The developed techniques enrich the motion capability and sensing methods of nano-robotic, accelerating the process towards a fully-automation for robotic manipulation purposes at small scales.

For the future work, with the developed work in this thesis, there are three aspects which can be investigated in the future. The first aspect is to develop a compact nano-manipulation AFM probe with force feedback, such as a nano-griper. Efficient pick-and-place strategy should be developed with the consideration of the adhesion force at the small scale. This will guarantee the efficiency and the stability during handling tasks. The second perspective is to develop multi-AFM probes cooperative manipulation for complicated tasks. Challenging algorithm of motion planning is requested to dispatch collision-free trajectories for AFM probes. Multiple AFM probes tracking is another tricky issue needed to be solved. Meanwhile, virtual reality (VR) can be carried out for the robotic configuration simulation to guide the complex assembly when measurements from external sensors are not accessible. Eventually, the overall enhancement on sensing information fusion, pick-and-place and motion plan, will enormously boost the commercialization process of micro/nano-robotic for industrial applications.

Appendices

Appendix A

Geometric Curve Characterization

The geometric curve can be defined in an explicit form, an implicit form or in a parametric form [135]. In the explicit form, the output variable is completely defined by other independent variables. For instance, in the equation $y = mx + b$, the output variable y is defined by the independent variable x to describe a straight line in $\mathbb{R}^2$. In the implicit form, all the variables are grouped on one side of the equation. For instance, the equation of a circle $f(x, y) = x^2 + y^2 = r2$ in $\mathbb{R}^2$, and the equation of a sphere $f(x, y, z) = x^2 + y^2 + z^2 = r^2$ in $\mathbb{R}^3$. A parameterized curve is able to describe the geometry of a curve in a more general way. Each point coordinate of the curve is defined as functions of one parameter. For instance, a 3D Cartesian parametrized curve is defined as:

$$S_p(c_p) = \begin{bmatrix} S_{px}(c_p) \\ S_{py}(c_p) \\ S_{pz}(c_p) \end{bmatrix} \tag{A.1}$$

where S_{px}, S_{py}, S_{pz} are the functions of the parameter c_p.

Generally, a parameterized curve is defined as $(S_p : I_p \rightarrow \mathbb{R}^n)$, which maps an interval $I_p = (a, b)$ to $\mathbb{R}^n$ space [34] [135]. As a result, a point whose differential $\frac{S_p}{c_p} = \hat{S}_p(c_p) \neq 0$ is called a regular point. Point whose differential $\hat{S}_p(c_p) = 0$ for $c_p \in I_p$ is called a singular point. A smooth regular parametrized curve should be differentiable and without singular points.

Arc length: the curve $S_p(s_p)$ is parameterized with respect to its arc length s_p. The arc s_p is defined as the segment length between two curve points (c_{p1} and c_{p2}) along the curve. If the curve is differentiable, its arc length starts from the starting point is defined as:

$$s_p(c_p) = \int_{c_{p0}}^{c_{pn}} ||\hat{\mathrm{S}}_{\mathrm{p}}(\mathrm{c_p})||\, \mathrm{d}c_p = \int_{c_{p0}}^{c_{pn}} \sqrt{\hat{\mathrm{S}}_{\mathrm{px}}(\mathrm{c_p})^2 + \hat{\mathrm{S}}_{\mathrm{py}}(\mathrm{c_p})^2 + \hat{\mathrm{S}}_{\mathrm{pz}}(\mathrm{c_p})^2}\, \mathrm{d}c_p \tag{A.2}$$

where $||\hat{S}_p(c_p)|| = \sqrt{\hat{S}_{px}(c_p)^2 + \hat{S}_{py}(c_p)^2 + \hat{S}_{pz}(c_p)^2}$ is the Euclidean norm of the vector $\hat{S}_p(c_p)$.

Tangent vector: as s_p is the arc length, the derivative of s_p is the tangent vector of the curve at point c_p. The unit vector is given as:

$$k_p(s_p) = \frac{\mathrm{d}S_p(s_p)}{\mathrm{d}s_p} = S'_p(s_p) \tag{A.3}$$

The derivative of $C_p(s_p) = ||k'_p(s_p)||$ is the curve curvature. which is given as:

$$C_p(s_p) = \sqrt{S''_p(s_p) \cdot S''_p(s_p)} \tag{A.4}$$

Normal vector: as $k_p(s_p)$ is the unit vector, $k_p(s_p) \cdot k_p(s_p) = 1$. The derivative of this equation results in $k_p(s_p) \cdot k'_p(s_p) = 0$. Here, $k'_p(s_p)$ represents a vector perpendicular to $k_p(s_p)$. Assuming that $k'_p(s_p)$, the curvature, is not zero, the unit vector of $k'_p(s_p)$ is defined as the principle normal vector n_p:

$$n_p(s_p) = \frac{k'_p(s_p)}{||k'_p(s_p)||} = \frac{k'_p(s_p)}{C_p(s_p)} \tag{A.5}$$

Bi-normal vector: k_p and n_p span the plane of curvature. Furthermore, in order to build a Frenet frame, a bi-normal vector b_p is defined as:

$$b_p = k_p \times n_p \tag{A.6}$$

As a result, the orthogonal base of a Frenet frame is formed by the parameters k_p, n_p, b_p. There is a natural relationship between these vectors that is encoded by the curvature and the torsion of the parametric curve. The curvature is measuring how much the curve is bending as it is traced out, while the torsion is measuring the twisting of the curve. The origin point of the frame is the projected point of the AFM probe tip onto the geometric curve S_p.

Curve torsion: the torsion τ_p measures the speed of rotation of the binormal vector at the given point [107]. By computing the derivative of the Bi-normal vector b_p, with respect to the arc length s_p, the following equation is obtained:

$$b'_p = \underbrace{\underbrace{k'_p}_{=C_p n_p} \times n_p}_{=0} + k_p \times n'_p \tag{A.7}$$

Here, b'_p is perpendicular to k_p. In addition, b'_p is also perpendicular to b_p due to $||b_p|| = 1$. Thus, b'_p is parallel to n_p, which as defined $b'_p = -\tau_p n_p$. Thereby the curve torsion is:

$$\tau_p = -n_p \cdot b'_p = n'_p \cdot b_p \tag{A.8}$$

n'_p can be expressed as:

$$n'_p = -C_p k_p + \tau_p b_p \tag{A.9}$$

Frenet formula: it is described by:

$$\begin{bmatrix} k'_p \\ n'_p \\ b'_p \end{bmatrix} = \begin{bmatrix} 0 & C_p & 0 \\ -C_p & 0 & \tau_p \\ 0 & -\tau_p & 0 \end{bmatrix} \begin{bmatrix} k_p \\ n_p \\ b_p \end{bmatrix} \tag{A.10}$$

Bibliography

[1] J-O. Abrahamians, B. Sauvet, J. Polesel-Maris, R. Braive, and S. Régnier. A nanorobotic system for in situ stiffness measurements on membranes. *IEEE Transactions on Robotics*, 30:119–124, 2013.

[2] Jean-Ochin Abrahamians, Bruno Sauvet, Jérôme Polesel-Maris, Rémy Braive, and Stéphane Régnier. A nanorobotic system for in situ stiffness measurements on membranes. *IEEE Transactions on Robotics*, 30(1):119–124, 2013.

[3] Jean-Ochin Abrahamians, Bruno Sauvet, Jérôme Polesel-Maris, Rémy Braive, and Stéphane Régnier. A nanorobotic system for in situ stiffness measurements on membranes. *IEEE Transactions on Robotics*, 30(1):119–124, 2014.

[4] Shivang Agarwal, Jean Ogier Du Terrail, and Frédéric Jurie. Recent advances in object detection in the age of deep convolutional neural networks. *arXiv preprint arXiv:1809.03193*, 2018.

[5] Mohd Ridzuan Ahmad, Masahiro Nakajima, Masaru Kojima, Seiji Kojima, Michio Homma, and Toshio Fukuda. Instantaneous and quantitative single cells viability determination using dual nanoprobe inside esem. *IEEE Transactions on Nanotechnology*, 11(2):298–306, 2012.

[6] Mohd Ridzuan Ahmad, Masahiro Nakajima, Masaru Kojima, Seiji Kojima, Michio Homma, and Toshio Fukuda. Nanofork for single cells adhesion measurement via esem-nanomanipulator system. *IEEE transactions on nanobioscience*, 11(1):70–78, 2012.

[7] Mohd Ridzuan Ahmad, Masahiro Nakajima, Seiji Kojima, Michio Homma, and Toshio Fukuda. The effects of cell sizes, environmental conditions, and growth phases on the strength of individual w303 yeast cells inside esem. *IEEE transactions on nanobioscience*, 7(3):185–193, 2008.

[8] Mohd Ridzuan Ahmad, Masahiro Nakajima, Seiji Kojima, Michio Homma, and Toshio Fukuda. In situ single cell mechanics characterization of yeast cells using nanoneedles inside environmental sem. *IEEE Transactions on Nanotechnology*, 7(5):607–616, 2008.

[9] Mohd Ridzuan Ahmad, Masahiro Nakajima, Seiji Kojima, Michio Homma, and Toshio Fukuda. Nanoindentation methods to measure viscoelastic properties of single cells using sharp, flat, and buckling tips inside esem. *IEEE transactions on nanobioscience*, 9(1):12–23, 2010.

[10] Mohd Ridzuan Ahmad, Masahiro Nakajima, Seiji Kojima, Michio Homma, and Toshio Fukuda. Buckling nanoneedle for characterizing single cells mechanics inside environmental sem. *IEEE Transactions on Nanotechnology*, 10(2):226–236, 2011.

[11] Seiji Akita and Yoshikazu Nakayama. Manipulation of nanomaterial by carbon nanotube nanotweezers in scanning probe microscope. *Japanese journal of applied physics*, 41(6S):4242, 2002.

[12] Mohammad Al Janaideh, Micky Rakotondrabe, and Omar Aljanaideh. Further results on hysteresis compensation of smart micropositioning systems with the inverse prandtl–ishlinskii compensator. *IEEE Transactions on Control Systems Technology*, 24(2):428–439, 2016.

[13] Mehdi Ammi and Antoine Ferreira. Robotic assisted micromanipulation system using virtual fixtures and metaphors. In *Proceedings 2007 IEEE International Conference on Robotics and Automation*, pages 454–460. IEEE, 2007.

[14] Kanna Aoki, Hideki T Miyazaki, Hideki Hirayama, Kyoji Inoshita, Toshihiko Baba, Kazuaki Sakoda, Norio Shinya, and Yoshinobu Aoyagi. Microassembly of semiconductor three-dimensional photonic crystals. *Nature materials*, 2(2):117–121, 2003.

[15] Quentin T Aten, Brian D Jensen, Sandra H Burnett, and Larry L Howell. A self-reconfiguring metamorphic nanoinjector for injection into mouse zygotes. *Review of Scientific Instruments*, 85(5):055005, 2014.

[16] Tomas Baca, Daniel Hert, Giuseppe Loianno, Martin Saska, and Vijay Kumar. Model predictive trajectory tracking and collision avoidance for reliable outdoor deployment of unmanned aerial vehicles. In *2018 IEEE/RSJ International Conference on Intelligent Robots and Systems (IROS)*, pages 6753–6760. IEEE, 2018.

[17] Dominik J Bell, Lixin Dong, Bradley J Nelson, Matthias Golling, Li Zhang, and Detlev Grützmacher. Fabrication and characterization of three-dimensional ingaas/gaas nanosprings. *Nano Letters*, 6(4):725–729, 2006.

[18] Christian Belly and Willy Charon. Benefits of amplification in an inertial stepping motor. *Mechatronics*, 22(2):177–183, 2012.

[19] Matthew B Blaschko and Christoph H Lampert. Learning to localize objects with structured output regression. In *European conference on computer vision*, pages 2–15. Springer, 2008.

[20] Aude Bolopion, Hui Xie, Dogan Sinan Haliyo, and Stéphane Régnier. Haptic teleoperation for 3-d microassembly of spherical objects. *IEEE/ASME Transactions on Mechatronics*, 17(1):116–127, 2010.

[21] M. Boudaoud, T. Lu, S. Liang, R. Oubellil, and S. Régnier. A voltage/frequency modeling for a multi-dofs serial nanorobotic system based on piezoelectric inertial actuators. *IEEE/ASME Transactions on Mechatronics*, 23(6):2814–2824, 2018.

[22] Mokrane Boudaoud, Shuai Liang, Tianming Lu, Raouia Oubellil, and Stéphane Régnier. Voltage/frequency rate dependent modeling for nano-robotic systems based on piezoelectric stick-slip actuators. In *Intelligent Robots and Systems (IROS), 2016 IEEE/RSJ International Conference on*, pages 5297–5303. IEEE, 2016.

[23] Mokrane Boudaoud, Tianming Lu, Shuai Liang, Raouia Oubellil, and Stephane Régnier. Voltage/frequency rate dependent modeling for nano-robotic systems based on piezoelectric stick-slip actuators. In *IEEE/RSJ International Conference on Intelligent Robots and Systems*, 2016.

[24] J-M Breguet and Reymond Clavel. Stick and slip actuators: design, control, performances and applications. In *Micromechatronics and Human Science, 1998. MHS'98. Proceedings of the 1998 International Symposium on*, pages 89–95. IEEE, 1998.

[25] Jean-Marc Breguet, Walter Driesen, Fabian Kaegi, and Thomas Cimprich. Applications of piezo-actuated micro-robots in micro-biology and material science. In *International Conference on Mechatronics and Automation*, 2007.

[26] Kenneth Carlson, Karin N Andersen, Volkmar Eichhorn, Dirch Hjorth Petersen, IYY Bu, KBK Teo, WI Milne, S Fatikow, et al. A carbon nanofibre scanning probe assembled using an electrothermal microgripper. *Nanotechnology*, 18(34):345501, 2007.

[27] Technologies Cedrat. http://www.cedrat-technologies.com/, 2015.

[28] Brandon K Chen, David Anchel, Zheng Gong, Rachel Cotton, Ren Li, Yu Sun, and David P Bazett-Jones. Nano-dissection and sequencing of dna at single sub-nuclear structures. *small*, 10(16):3267–3274, 2014.

[29] Jun Chen, Ji Gel, Brandon K Chen, Zheng Gong, Chao Zhou, Chaoyang Shi, Changhai Ru, Huayan Pu, Yan Peng, Shaorong Xie, and Yu Sun. Automated sem-guided afm scan with dynamically varied scan speed. In *2018 International Conference on Manipulation, Automation and Robotics at Small Scales (MARSS)*, pages 1–6. IEEE, 2018.

[30] H Corte-León, P Krzysteczko, F Marchi, J-F Motte, Alessandra Manzin, HW Schumacher, V Antonov, and O Kazakova. Detection of a magnetic bead by hybrid nanodevices using scanning gate microscopy. *AIP Advances*, 6(5):056502, 2016.

[31] Bassem Dahroug, Brahim Tamadazte, and Andreff. Visual servoing controller for time-invariant 3d path following with remote centre of motion constraint. In *Robotics and Automation (ICRA), 2017 IEEE International Conference on*, pages 3612–3618. IEEE, 2017.

[32] Jifeng Dai, Yi Li, Kaiming He, and Jian Sun. R-fcn: Object detection via region-based fully convolutional networks. In *Advances in neural information processing systems*, pages 379–387, 2016.

[33] Guillaume Demesure, Michael Defoort, Abdelghani Bekrar, Damien Trentesaux, and Mohamed Djemai. Decentralized motion planning and scheduling of agvs in an fms. *IEEE Transactions on Industrial Informatics*, 14(4):1744–1752, 2017.

[34] Manfredo P Do Carmo. *Differential Geometry of Curves and Surfaces: Revised and Updated Second Edition*. Courier Dover Publications, 2016.

[35] Lixin Dong, Bradley J Nelson, Toshio Fukuda, and Fumihito Arai. Towards nanotube linear servomotors. *IEEE Transactions on Automation Science and Engineering*, 3(3):228–235, 2006.

[36] Pierre Dupont, Vincent Hayward, Brian Armstrong, and Friedhelm Altpeter. Single state elastoplastic friction models. *Automatic Control, IEEE Transactions on*, 47(5):787–792, 2002.

[37] Volkmar Eichhorn, Kenneth Carlson, Karin N Andersen, Sergej Fatikow, and Peter Boggild. Nanorobotic manipulation setup for pick-and-place handling and nondestructive characterization of carbon nanotubes. In *Intelligent Robots and Systems, 2007. IROS 2007. IEEE/RSJ International Conference on*, pages 291–296. IEEE, 2007.

[38] Volkmar Eichhorn, Sergej Fatikow, Tim Wortmann, Christian Stolle, Christoph Edeler, Daniel Jasper, Ozlem Sardan, Peter Boggild, Guillaume Boetsch, Christophe Canales, et al. Nanolab: A nanorobotic system for automated pick-and-place handling and characterization of cnts. In *2009 IEEE International Conference on Robotics and Automation*, pages 1826–1831. IEEE, 2009.

[39] Sergej Fatikow, Volkmar Eichhorn, Thomas Wich, Torsten Sievers, Olaf HanBler, and Karin Nordstrom Andersen. Depth-detection methods for cnt manipulation and characterization in a scanning electron microscope. In *Mechatronics and Automation, 2007. ICMA 2007. International Conference on*, pages 45–50. IEEE, 2007.

[40] Andrew J Fleming. A review of nanometer resolution position sensors: Operation and performance. *Sensors and Actuators A: Physical*, 190:106–126, 2013.

[41] Andrew J Fleming, Sumeet S Aphale, and SO Reza Moheimani. A new method for robust damping and tracking control of scanning probe microscope positioning stages. *IEEE Transactions on Nanotechnology*, 9(4):438–448, 2010.

[42] Thor I Fossen, Kristin Ytterstad Pettersen, and Roberto Galeazzi. Line-of-sight path following for dubins paths with adaptive sideslip compensation of drift forces. *IEEE Trans. Contr. Sys. Techn.*, 23(2):820–827, 2015.

[43] Toshio Fukuda, Fumihito Arai, and Lixin Dong. Assembly of nanodevices with carbon nanotubes through nanorobotic manipulations. *Proceedings of the IEEE*, 91(11):1803–1818, 2003.

[44] Toshio Fukuda, Masahiro Nakajima, Mohd Ridzuan Ahmad, Yajing Shen, and Masaru Kojima. Micro-and nanomechatronics. *IEEE Industrial Electronics Magazine*, 4(4):13–22, 2010.

[45] Toshio Fukuda, Masahiro Nakajima, Pou Liu, and Mohd Ridzuan Ahmad. Bringing the nanolaboratory inside electron microscopes. *IEEE Nanotechnology Magazine*, 2(2), 2008.

[46] Rong-Fong Fung, Chang-Fu Han, and Jer-Rong Chang. Dynamic modeling of a high-precision self-moving stage with various frictional models. *Applied Mathematical Modelling*, 32(9):1769–1780, 2008.

[47] Michaël Gauthier, Sébastien Alvo, Jérôme Dejeu, Brahim Tamadazte, Patrick Rougeot, and Stéphane Régnier. Analysis and specificities of adhesive forces between microscale and nanoscale. *IEEE Transactions on Automation Science and Engineering*, 10(3):562–570, 2013.

[48] Ross Girshick. Fast r-cnn. In *Proceedings of the IEEE international conference on computer vision*, pages 1440–1448, 2015.

[49] Zheng Gong, Brandon K Chen, Jun Liu, and Yu Sun. Robotic probing of nanostructures inside scanning electron microscopy. *IEEE Transactions on Robotics*, 30(3):758–765, 2014.

[50] Zheng Gong, Brandon K Chen, Jun Liu, Chao Zhou, Dave Anchel, Xiao Li, Ji Ge, David P Bazett-Jones, and Yu Sun. Fluorescence and sem correlative microscopy for nanomanipulation of subcellular structures. *Light: Science & Applications*, 3(11):e224, 2014.

[51] Guo-Ying Gu, Li-Min Zhu, and Chun-Yi Su. Modeling and compensation of asymmetric hysteresis nonlinearity for piezoceramic actuators with a modified prandtl–ishlinskii model. *IEEE Transactions on Industrial Electronics*, 61(3):1583–1595, 2014.

[52] Guo-Ying Gu, Li-Min Zhu, Chun-Yi Su, Han Ding, and Sergej Fatikow. Modeling and control of piezo-actuated nanopositioning stages: A survey. *IEEE Transactions on Automation Science and Engineering*, 13(1):313–332, 2016.

[53] Yana Guo, Qing Shi, Zhan Yang, Huaping Wang, Ning Yu, Lining Sun, Qiang Huang, and Toshio Fukuda. Automated pick-up of carbon nanotubes inside a scanning electron microscope. In *2016 IEEE/RSJ International Conference on Intelligent Robots and Systems (IROS)*, pages 5318–5323. IEEE, 2016.

[54] Benjamin Gutjahr, Lutz Gröll, and Moritz Werling. Lateral vehicle trajectory optimization using constrained linear time-varying mpc. *IEEE Transactions on Intelligent Transportation Systems*, 18(6):1586–1595, 2016.

[55] Andreas J Häusler, Alessandro Saccon, António Pedro Aguiar, John Hauser, and António M Pascoal. Energy-optimal motion planning for multiple robotic vehicles with collision avoidance. *IEEE Transactions on Control Systems Technology*, 24(3):867–883, 2015.

[56] R Heiderhoff, I Joachimsthaler, and LJ Balk. A universal scanning-probe-microscope based hybrid system. *VDI BERICHTE*, 1803:311–312, 2003.

[57] Matthias Hunstig, Tobias Hemsel, and Walter Sextro. Stick–slip and slip–slip operation of piezoelectric inertia drives. part i: Ideal excitation. *Sensors and Actuators A: Physical*, 200:90–100, 2013.

[58] Ahmed Hussein, Heba Mostafa, Mohamed Badrel-din, Osama Sultan, and Alaa Khamis. Metaheuristic optimization approach to mobile robot path planning. In *2012 international conference on engineering and technology (ICET)*, pages 1–6. IEEE, 2012.

[59] Daniel Jasper, Christian Dahmen, Florian Krohs, Volkmar Eichhorn, Michael Weigel-Jech, et al. Robot-based automation on the nanoscale. In *Encyclopedia of Nanotechnology*, pages 2246–2264. Springer, 2012.

[60] Jie Ji, Amir Khajepour, Wael William Melek, and Yanjun Huang. Path planning and tracking for vehicle collision avoidance based on model predictive control with multiconstraints. *IEEE Transactions on Vehicular Technology*, 66(2):952–964, 2016.

[61] Takefumi Kanda, Akira Makino, Tomohisa Ono, Koichi Suzumori, Takeshi Morita, and Minoru Kuribayashi Kurosawa. A micro ultrasonic motor using a micro-machined cylindrical bulk pzt transducer. *Sensors and Actuators A: physical*, 127(1):131–138, 2006.

[62] Takefumi Kanda, Akira Makino, Tomohisa Ono, Koichi Suzumori, Takeshi Morita, and Minoru Kuribayashi Kurosawa. A micro ultrasonic motor using a micro-machined cylindrical bulk pzt transducer. *Sensors and Actuators A: physical*, 127(1):131–138, 2006.

[63] Bradley E Kratochvil, Lixin Dong, and Bradley J Nelson. Real-time rigid-body visual tracking in a scanning electron microscope. *The International Journal of Robotics Research*, 28(4):498–511, 2009.

[64] Alex Krizhevsky, Ilya Sutskever, and Geoffrey E Hinton. Imagenet classification with deep convolutional neural networks. In *Advances in neural information processing systems*, pages 1097–1105, 2012.

[65] Klaus Kuhnen and Hartmut Janocha. Inverse feedforward controller for complex hysteretic nonlinearities in smart-material systems. *Control and Intelligent Systems*, 29(3):74–83, 2001.

[66] RT Rajendra Kumar, SU Hassan, O Sardan Sukas, Volkmar Eichhorn, F Krohs, S Fatikow, and P Boggild. Nanobits: customizable scanning probe tips. *Nanotechnology*, 20(39):395703, 2009.

[67] Fakhreddine Landolsi, Fathi H Ghorbel, Jun Lou, Hao Lu, and Yuekai Sun. Nanoscale friction dynamic modeling. *Journal of dynamic systems, measurement, and control*, 131(6):061102, 2009.

[68] Steven M LaValle. *Planning algorithms*. Cambridge university press, 2006.

[69] Jianping Li, Hongwei Zhao, Han Qu, Tao Cui, Lu Fu, Hu Huang, Luquan Ren, and Zunqiang Fan. A piezoelectric-driven rotary actuator by means of inchworm motion. *Sensors and Actuators A: Physical*, 194:269–276, 2013.

[70] Linlin Li, Chun-Xia Li, Guoying Gu, and Li-Min Zhu. Positive acceleration, velocity and position feedback based damping control approach for piezo-actuated nanopositioning stages. *Mechatronics*, 47:97 – 104, 2017.

[71] Y. Li and Q. Xu. Adaptive sliding mode control with perturbation estimation and pid sliding surface for motion tracking of a piezo-driven micromanipulator. *IEEE Transactions on Control Systems Technology*, 18(4):798–810, 2010.

[72] Zhijun Li, Chenguang Yang, Chun-Yi Su, Jun Deng, and Weidong Zhang. Vision-based model predictive control for steering of a nonholonomic mobile robot. *IEEE Transactions on Control Systems Technology*, 24(2):553–564, 2016.

[73] Shuai Liang, Mokrane Boudaoud, Barthélémy Cagneau, and Stéphane Régnier. Velocity characterization and control strategies for nano-robotic systems based on piezoelectric stick-slip actuators. In *2017 IEEE International Conference on Robotics and Automation (ICRA)*, pages 6606–6611. IEEE, 2017.

[74] Hwee Choo Liaw, Bijan Shirinzadeh, and Julian Smith. Enhanced sliding mode motion tracking control of piezoelectric actuators. *Sensors and Actuators A: Physical*, 138(1):194–202, 2007.

[75] Seong Chu Lim, Keun Soo Kim, Seung Yol Jeong, Shinje Cho, Jae-Eun Yoo, Young Hee Lee, et al. Nanomanipulator-assisted fabrication and characterization of carbon nanotubes inside scanning electron microscope. *Micron*, 36(5):471–476, 2005.

[76] Tsung-Yi Lin, Michael Maire, Serge Belongie, James Hays, Pietro Perona, Deva Ramanan, Piotr Dollár, and C Lawrence Zitnick. Microsoft coco: Common objects in context. In *European conference on computer vision*, pages 740–755. Springer, 2014.

[77] Jiechao Liu, Paramsothy Jayakumar, Jeffrey L Stein, and Tulga Ersal. Combined speed and steering control in high-speed autonomous ground vehicles for obstacle avoidance using model predictive control. *IEEE Transactions on Vehicular Technology*, 66(10):8746–8763, 2017.

[78] Pou Liu, Fumihito Arai, and Toshio Fukuda. Cutting of carbon nanotubes assisted with oxygen gas inside a scanning electron microscope. *Applied physics letters*, 89(11):113104, 2006.

[79] Pou Liu, Kalle Kantola, Toshio Fukuda, and Fumihito Arai. Nanoassembly of nanostructures by cutting, bending and soldering of carbon nanotubes with electron beam. *Journal of nanoscience and nanotechnology*, 9(5):3040–3045, 2009.

[80] Wei Liu, Dragomir Anguelov, Dumitru Erhan, Christian Szegedy, Scott Reed, Cheng-Yang Fu, and Alexander C Berg. Ssd: Single shot multibox detector. In *European conference on computer vision*, pages 21–37. Springer, 2016.

[81] Jonathan Long, Evan Shelhamer, and Trevor Darrell. Fully convolutional networks for semantic segmentation. In *Proceedings of the IEEE conference on computer vision and pattern recognition*, pages 3431–3440, 2015.

[82] Haiwei Lu, Jianguo Zhu, Zhiwei Lin, and Youguang Guo. An inchworm mobile robot using electromagnetic linear actuator. *Mechatronics*, 19(7):1116–1125, 2009.

[83] Haiwei Lu, Jianguo Zhu, Zhiwei Lin, and Youguang Guo. An inchworm mobile robot using electromagnetic linear actuator. *Mechatronics*, 19(7):1116–1125, 2009.

[84] Tianming Lu, Mokrane Boudaoud, David Hériban, and Stéphane Régnier. Nonlinear modeling for a class of nano-robotic systems using piezoelectric stick-slip actuators. In *Intelligent Robots and Systems (IROS), 2015 IEEE/RSJ International Conference on*, pages 6020–6025. IEEE, 2015.

[85] Tianming Lu, Mokrane Boudaoud, David Hériban, and Stephane Régnier. Nonlinear modeling for a class of nano-robotic systems using piezoelectric stick-slip actuators. In *International Conference on Intelligent Robots and Systems (IROS)*, 2015.

[86] Alois Lugstein, Mathias Steinmair, A Steiger, Hans Kosina, and Emmerich Bertagnolli. Anomalous piezoresistance effect in ultrastrained silicon nanowires. *Nano letters*, 10(8):3204–3208, 2010.

[87] Nick Malone, Hao-Tien Chiang, Kendra Lesser, Meeko Oishi, and Lydia Tapia. Hybrid dynamic moving obstacle avoidance using a stochastic reachable set-based potential field. *IEEE Transactions on Robotics*, 33(5):1124–1138, 2017.

[88] Naresh Marturi, Sounkalo Dembélé, and Nadine Piat. Depth and shape estimation from focus in scanning electron microscope for micromanipulation. In *Control, Automation, Robotics and Embedded Systems (CARE), 2013 International Conference on*, pages 1–6. IEEE, 2013.

[89] Naresh Marturi, Brahim Tamadazte, Sounkalo Dembélé, and Nadine Piat. Visual servoing-based depth-estimation technique for manipulation inside sem. *IEEE Transactions on Instrumentation and Measurement*, 65(8):1847–1855, 2016.

[90] Uwe Mick, Volkmar Eichhorn, Tim Wortmann, Claas Diederichs, and Sergej Fatikow. Combined nanorobotic afm/sem system as novel toolbox for automated hybrid analysis and manipulation of nanoscale objects. In *Robotics and Automation (ICRA), 2010 IEEE International Conference on*, pages 4088–4093. IEEE, 2010.

[91] Manuel R Mikczinski, Gabriella Josefsson, Gary Chinga-Carrasco, E Kristofer Gamstedt, and Sergej Fatikow. Nanorobotic testing to assess the stiffness properties of nanopaper. *IEEE Transactions on robotics*, 30(1):115–119, 2014.

[92] SO Reza Moheimani. A survey of recent innovations in vibration damping and control using shunted piezoelectric transducers. *IEEE transactions on control systems technology*, 11(4):482–494, 2003.

[93] Chanwoo Moon, Sungho Lee, and JK Chung. A new fast inchworm type actuator with the robust i/q heterodyne interferometer feedback. *Mechatronics*, 16(2):105–110, 2006.

[94] Pascal Morin and Claude Samson. Motion control of wheeled mobile robots. In *Springer Handbook of Robotics*, pages 799–826. Springer, 2008.

[95] Tobias Nägeli, Javier Alonso-Mora, Alexander Domahidi, Daniela Rus, and Otmar Hilliges. Real-time motion planning for aerial videography with dynamic obstacle avoidance and viewpoint optimization. *IEEE Robotics and Automation Letters*, 2(3):1696–1703, 2017.

[96] Alejandro Newell, Kaiyu Yang, and Jia Deng. Stacked hourglass networks for human pose estimation. In *European Conference on Computer Vision*, pages 483–499. Springer, 2016.

[97] Tiago Oliveira, A Pedro Aguiar, and Pedro Encarnacao. Moving path following for unmanned aerial vehicles with applications to single and multiple target tracking problems. *IEEE Transactions on Robotics*, 32(5):1062–1078, 2016.

[98] R. Oubellil, A. Voda, M. Boudaoud, and S. Régnier. Mixed stepping/scanning mode control of stick-slip sem-integrated nano-robotic systems. *Sensors and Actuators A: Physical*, 285:258 – 268, 2019.

[99] Ali Oulmas, Nicolas Andreff, and Stéphane Régnier. Closed-loop 3d path following of scaled-up helical microswimmers. In *Robotics and Automation (ICRA), 2016 IEEE International Conference on*, pages 1725–1730. IEEE, 2016.

[100] PR Ouyang, RC Tjiptoprodjo, WJ Zhang, and GS Yang. Micro-motion devices technology: The state of arts review. *The International Journal of Advanced Manufacturing Technology*, 38(5-6):463–478, 2008.

[101] L-M Peng, Q Chen, XL Liang, S Gao, JY Wang, S Kleindiek, and SW Tai. Performing probe experiments in the sem. *Micron*, 35(6):495–502, 2004.

[102] Yong Peng, Tony Cullis, and Beverley Inkson. Bottom-up nanoconstruction by the welding of individual metallic nanoobjects using nanoscale solder. *Nano letters*, 9(1):91–96, 2008.

[103] Zhouhua Peng and Jun Wang. Output-feedback path-following control of autonomous underwater vehicles based on an extended state observer and projection neural networks. *IEEE Transactions on Systems, Man, and Cybernetics: Systems*, 48(4):535–544, 2018.

[104] Pietro Perona and Jitendra Malik. Scale-space and edge detection using anisotropic diffusion. *IEEE Transactions on pattern analysis and machine intelligence*, 12(7):629–639, 1990.

[105] Ian R Petersen and Himanshu R Pota. Minimax LQG optimal control of a flexible beam. *Control Engineering Practice*, 11(11):1273–1287, 2003.

[106] Mogens Graf Plessen, Daniele Bernardini, Hasan Esen, and Alberto Bemporad. Spatial-based predictive control and geometric corridor planning for adaptive cruise control coupled with obstacle avoidance. *IEEE Transactions on Control Systems Technology*, 26(1):38–50, 2017.

[107] Andrew N Pressley. *Elementary differential geometry*. Springer Science & Business Media, 2010.

[108] Micky Rakotondrabe. Bouc–wen modeling and inverse multiplicative structure to compensate hysteresis nonlinearity in piezoelectric actuators. *IEEE Transactions on Automation Science and Engineering*, 8(2):428–431, 2011.

[109] Micky Rakotondrabe, Cédric Clévy, and Philippe Lutz. Complete open loop control of hysteretic, creeped, and oscillating piezoelectric cantilevers. *IEEE Transactions on Automation Science and Engineering*, 7(3):440–450, 2010.

[110] Micky Rakotondrabe, Yassine Haddab, and Philippe Lutz. Voltage/frequency proportional control of stick-slip micropositioning systems. *IEEE Transactions on Control Systems Technology*, 16(6):1316–1322, 2008.

[111] Yadollah Rasekhipour, Amir Khajepour, Shih-Ken Chen, and Bakhtiar Litkouhi. A potential field-based model predictive path-planning controller for autonomous road vehicles. *IEEE Transactions on Intelligent Transportation Systems*, 18(5):1255–1267, 2016.

[112] Joseph Redmon, Santosh Divvala, Ross Girshick, and Ali Farhadi. You only look once: Unified, real-time object detection. In *Proceedings of the IEEE conference on computer vision and pattern recognition*, pages 779–788, 2016.

[113] Shaoqing Ren, Kaiming He, Ross Girshick, and Jian Sun. Faster r-cnn: Towards real-time object detection with region proposal networks. In *Advances in neural information processing systems*, pages 91–99, 2015.

[114] Stefan Romeis, Jonas Paul, Patrick Herre, Mathias Hanisch, Robin N Klupp Taylor, Jochen Schmidt, and Wolfgang Peukert. In situ deformation and breakage of silica particles inside a sem. *Procedia Engineering*, 102:201–210, 2015.

[115] Ugo Rosolia, Ashwin Carvalho, and Francesco Borrelli. Autonomous racing using learning model predictive control. In *2017 American Control Conference (ACC)*, pages 5115–5120. IEEE, 2017.

[116] C. Ru, Y. Zhang, Y. Sun, Y. Zhong, X. Sun, D. Hoyle, and I. Cotton. Automated four-point probe measurement of nanowires inside a scanning electron microscope. *IEEE Transactions on Nanotechnology*, 10(4):674–681, July 2011.

[117] Changhai Ru and Steve To. Contact detection for nanomanipulation in a scanning electron microscope. *Ultramicroscopy*, 118:61–66, 2012.

[118] Changhai Ru, Yong Zhang, Haibo Huang, and Tao Chen. An improved visual tracking method in scanning electron microscope. *Microscopy and Microanalysis*, 18(3):612–620, 2012.

[119] Changhai Ru, Yong Zhang, Yu Sun, Yu Zhong, Xueliang Sun, David Hoyle, and Ian Cotton. Automated four-point probe measurement of nanowires inside a scanning electron microscope. *IEEE Transactions on Nanotechnology*, 10(4):674–681, 2010.

[120] Changhai Ru, Yong Zhang, Yu Sun, Yu Zhong, Xueliang Sun, David Hoyle, and Ian Cotton. Automated four-point probe measurement of nanowires inside a scanning electron microscope. *IEEE Transactions on Nanotechnology*, 10(4):674–681, 2011.

[121] Claude Samson. Path following and time-varying feedback stabilization of a wheeled mobile robot. In *Proceedings of the international conference on advanced robotics and computer vision*, volume 13, pages 1–1, 1992.

[122] Claude Samson. Control of chained systems application to path following and time-varying point-stabilization of mobile robots. *IEEE transactions on Automatic Control*, 40(1):64–77, 1995.

[123] Abu Sebastian and Srinivasa M Salapaka. Design methodologies for robust nano-positioning. *IEEE Transactions on Control Systems Technology*, 13(6):868–876, 2005.

[124] Babak Sedghi. Control design of hybrid systems via dehybridization. *EPFL*, 2003.

[125] Jean-Antoine Seon, Brahim Tamadazte, and Nicolas Andreff. Decoupling path following and velocity profile in vision-guided laser steering. *IEEE Transactions on Robotics*, 31(2):280–289, 2015.

[126] Yajing Shen, Mohd Ridzuan Ahmad, Masahiro Nakajima, Seiji Kojima, Michio Homma, and Toshio Fukuda. Evaluation of the single yeast cell's adhesion to ito substrates with various surface energies via esem nanorobotic manipulation system. *IEEE transactions on nanobioscience*, 10(4):217–224, 2011.

[127] Yajing Shen and Toshio Fukuda. State of the art: micro-nanorobotic manipulation in single cell analysis. *Robotics and Biomimetics*, 1(1):21, 2014.

[128] Yajing Shen, Masahiro Nakajima, Seiji Kojima, Michio Homma, and Toshio Fukuda. Study of the time effect on the strength of cell–cell adhesion force by a novel nano-picker. *Biochemical and biophysical research communications*, 409(2):160–165, 2011.

[129] Yajing Shen, Masahiro Nakajima, Seiji Kojima, Michio Homma, Masaru Kojima, and Toshio Fukuda. Single cell adhesion force measurement for cell viability identification using an afm cantilever-based micro putter. *Measurement science and technology*, 22(11):115802, 2011.

[130] Yajing Shen, Masahiro Nakajima, Zhan Yang, Seiji Kojima, Michio Homma, and Toshio Fukuda. Design and characterization of nanoknife with buffering beam for in situ single-cell cutting. *Nanotechnology*, 22(30):305701, 2011.

[131] Yajing Shen, Masahiro Nakajima, Zhenhai Zhang, and Toshio Fukuda. Dynamic force characterization microscopy based on integrated nanorobotic afm and sem system for detachment process study. *IEEE/ASME Transactions on Mechatronics*, 20(6):3009–3017, 2015.

[132] Chaoyang Shi, Devin K Luu, Qinmin Yang, Jun Liu, Jun Chen, Changhai Ru, Shaorong Xie, Jun Luo, Ji Ge, and Yu Sun. Recent advances in nanorobotic manipulation inside scanning electron microscopes. *Microsystems & Nanoengineering*, 2:16024, 2016.

[133] Qing Shi, Zhan Yang, Yana Guo, Huaping Wang, Lining Sun, Qiang Huang, and Toshio Fukuda. A vision-based automated manipulation system for the pick-up of carbon nanotubes. *IEEE/ASME Transactions on Mechatronics*, 2017.

[134] Martin Špiller and Zdeněk Hurák. Hybrid charge control for stick–slip piezoelectric actuators. *Mechatronics*, 21(1):100–108, 2011.

[135] Dirk Jan Struik. *Lectures on classical differential geometry*. Courier Corporation, 1961.

[136] Kaspar Suter, Terunobu Akiyama, Nicolaas F de Rooij, Andreas Baumgartner, Thomas Ihn, Klaus Ensslin, Urs Staufer, Paul M Koenraad, and Martijn Kemerink. Tuning fork afm with conductive cantilever. In *AIP Conference Proceedings*, volume 696, pages 227–233. AIP, 2003.

[137] SL Toh, PK Tan, YW Goh, E Hendarto, JL Cai, H Tan, QF Wang, Q Deng, J Lam, LC Hsia, et al. In-depth electrical analysis to reveal the failure mechanisms with nanoprobing. *IEEE Transactions on Device and Materials Reliability*, 8(2):387–393, 2008.

[138] Alexander Toshev and Christian Szegedy. Deeppose: Human pose estimation via deep neural networks. In *Proceedings of the IEEE conference on computer vision and pattern recognition*, pages 1653–1660, 2014.

[139] Meng-Shiun Tsai and Jin-Shin Chen. Robust tracking control of a piezoactuator using a new approximate hysteresis model. *Journal of dynamic systems, measurement, and control*, 125(1):96–102, 2003.

[140] Robert Tunnell and Sergej Fatikow. 3d position detection with an fib-sem dual beam system. In *Proceedings of the 10th WSEAS international conference on communications, electrical & computer engineering, and 9th WSEAS international conference on Applied electromagnetics, wireless and optical communications*, pages 128–133. World Scientific and Engineering Academy and Society (WSEAS), 2011.

[141] P Vasiljev, D Mazeika, and G Kulvietis. Modelling and analysis of omni-directional piezoelectric actuator. *Journal of Sound and Vibration*, 308(3):867–878, 2007.

[142] Geng Wang, Guoqiang Chen, and Fuzhong Bai. High-speed and precision control of a piezoelectric positioner with hysteresis, resonance and disturbance compensation. *Microsystem Technologies*, 22(10):2499–2509, 2016.

[143] Manfred Weck, Joachim Hümmler, and Bernd Petersen. Assembly of hybrid microsystems in a large-chamber scanning electron microscope by use of mechanical grippers. In *Micromachining and Microfabrication*, pages 223–229. International Society for Optics and Photonics, 1997.

[144] Martin Syre Wiig, Kristin Ytterstad Pettersen, and Thomas Røbekk Krogstad. Collision avoidance for underactuated marine vehicles using the constant avoidance angle algorithm. *IEEE Transactions on Control Systems Technology*, 2019.

[145] Xianbo Xiang, Caoyang Yu, and Qin Zhang. Robust fuzzy 3d path following for autonomous underwater vehicle subject to uncertainties. *Computers & Operations Research*, 84:165–177, 2017.

[146] Didi Xu, Arunkumar Subramanian, Lixin Dong, and Bradley J Nelson. Shaping nanoelectrodes for high-precision dielectrophoretic assembly of carbon nanotubes. *IEEE Transactions on Nanotechnology*, 8(4):449–456, 2009.

[147] Chia-Feng Yang, Shyr-Long Jeng, and Wei-Hua Chieng. Motion behavior of triangular waveform excitation input in an operating impact drive mechanism. *Sensors and Actuators A: Physical*, 166(1):66–77, 2011.

[148] Zhan Yang, Pengbo Wang, Yajing Shen, Tao Chen, Liguo Chen, Qiang Huang, Lining Sun, and Toshio Fukuda. Dual-mwcnt probe thermal sensor assembly and evaluation based on nanorobotic manipulation inside a field-emission-scanning electron microscope. *International Journal of Advanced Robotic Systems*, 12(3):21, 2015.

[149] Xutao Ye, Yong Zhang, Changhai Ru, Jun Luo, Shaorong Xie, and Yu Sun. Automated pick-place of silicon nanowires. *IEEE Transactions on Automation Science and Engineering*, 10(3):554–561, 2013.

[150] MinFeng Yu, Mark J Dyer, George D Skidmore, Henry W Rohrs, XueKun Lu, Kevin D Ausman, James R Von Ehr, and Rodney S Ruoff. Three-dimensional manipulation of carbon nanotubes under a scanning electron microscope. *Nanotechnology*, 10(3):244, 1999.

[151] Tianhao Zhang, Gregory Kahn, Sergey Levine, and Pieter Abbeel. Learning deep control policies for autonomous aerial vehicles with mpc-guided policy search. In *2016 IEEE international conference on robotics and automation (ICRA)*, pages 528–535. IEEE, 2016.

[152] Yan Liang Zhang, Jason Li, Steve To, Yong Zhang, Xutao Ye, and Yu Sun. Automated nanomanipulation for nano device construction. In *2012 IEEE International Conference on Robotics and Automation*, pages 1063–1068. IEEE, 2012.

[153] Yan Liang Zhang, Yong Zhang, Changhai Ru, Brandon K Chen, and Yu Sun. A load-lock-compatible nanomanipulation system for scanning electron microscope. *IEEE/ASME Transactions on Mechatronics*, 18(1):230–237, 2011.

[154] Yan Liang Zhang, Yong Zhang, Changhai Ru, Brandon K Chen, and Yu Sun. A load-lock-compatible nanomanipulation system for scanning electron microscope. *IEEE/ASME Transactions on Mechatronics*, 18(1):230–237, 2013.

[155] Zewei Zheng, Liang Sun, and Lihua Xie. Error-constrained los path following of a surface vessel with actuator saturation and faults. *IEEE Transactions on Systems, Man, and Cybernetics: Systems*, 2017.

[156] Chao Zhou, Zheng Gong, Brandon K Chen, Zhiqiang Cao, Junzhi Yu, Changhai Ru, Min Tan, Shaorong Xie, and Yu Sun. A closed-loop controlled nanomanipulation system for probing nanostructures inside scanning electron microscopes. *IEEE/ASME Transactions on Mechatronics*, 21(3):1233–1241, 2016.

[157] Xiaoqin Zhou, Jinqiang Zhao, Gangbing Song, and J Alexis De Abreu-Garcia. Preisach modeling of hysteresis and tracking control of a thunder actuator system. *Smart Structures and Materials 2003: Modeling, Signal Processing, and Control*, 5049:112–126, 2003.

[158] Bing Zhu and Wei Huo. 3-d path-following control for a model-scaled autonomous helicopter. *IEEE Transactions on Control Systems Technology*, 22(5):1927–1934, 2014.

[159] Yong Zhu, Qingquan Qin, Feng Xu, Fengru Fan, Yong Ding, Tim Zhang, Benjamin J Wiley, and Zhong Lin Wang. Size effects on elasticity, yielding, and fracture of silver nanowires: In situ experiments. *Physical review B*, 85(4):045443, 2012.

[160] Soren Zimmermann, Sergio Alfredo Garnica Barragan, and Sergej Fatikow. Nanorobotic processing of graphene: A platform tailored for rapid prototyping of graphene-based devices. *IEEE Nanotechnology Magazine*, 8(3):14–19, 2014.

[161] Sören Zimmermann, Volkmar Eichhorn, and Sergej Fatikow. Nanorobotic transfer and characterization of graphene flakes. In *Intelligent Robots and Systems (IROS), 2012 IEEE/RSJ International Conference on*, pages 640–645. IEEE, 2012.

[162] Sören Zimmermann, Tobias Tiemerding, and Sergej Fatikow. Automated robotic manipulation of individual colloidal particles using vision-based control. *IEEE/ASME Transactions on Mechatronics*, 20(5):2031–2038, 2014.

[163] Sören Zimmermann, Tobias Tiemerding, and Sergej Fatikow. Automated robotic manipulation of individual colloidal particles using vision-based control. *IEEE/ASME Transactions on Mechatronics*, 20(5):2031–2038, 2015.

[164] Sören Zimmermann, Tobias Tiemerding, Tie Li, Wenrong Wang, Yuelin Wang, and Sergej Fatikow. Automated mechanical characterization of 2-d materials using sem based visual servoing. *International Journal of Optomechatronics*, 7(4):283–295, 2013.

[165] Rui Zou, Vijay Kalivarapu, Eliot Winer, James Oliver, and Sourabh Bhattacharya. Particle swarm optimization-based source seeking. *IEEE Transactions on Automation Science and Engineering*, 12(3):865–875, 2015.